UNIVERSITY OF CALIFORNIA
RIVERSIDE

Secondary Aerosol Formation From Mobile Sources and a Biogenic Precursor

A Dissertation submitted in partial satisfaction
of the requirements for the degree of

Doctor of Philosophy

in

Chemical and Environmental Engineering

by

Sahar Ghadimi

March 2023

Dissertation Committee:
Dr. David R. Cocker III, Chairperson
Dr. Georgios Karavalakis
Dr. Don Collins

The Dissertation of Sahar Ghadimi is approved:

_____

_____

_____

Committee Chairperson

University of California, Riverside

Acknowledgment

Chapter 2 of this dissertation is reprinted in full from the following reference published by Elsevier, Journal of Science of The Total Environment:

- Ghadimi S, Zhu H, Durbin TD, Cocker DR, Karavalakis G. The impact of hydrogenated vegetable oil (HVO) on the formation of secondary organic aerosol (SOA) from in-use heavy-duty diesel vehicles. Sci Total Environ. 2022 May 20;822:153583. doi: 10.1016/j.scitotenv.2022.153583. Epub 2022 Jan 31. PMID: 35114249.

The co-authors Dr. David Cocker, Dr. Goerge Karvalakis listed in these publications directed and supervised the research which form the basis for this dissertation. I would first like to thank and recognize my advisor, Dr. David Cocker for his endless support and guidance throughout my Ph.D. program. You were always available to help and support me whenever I had questions and always made sure to push me to accomplish more, and to produce the highest quality work possible. I could not have found a better advisor, who could be more patient toward students. You have been a great advisor and resource to my success, and I am grateful for your generosity with your time.

I would also like to thank Dr. Georgios Karavalakis for all your support towards vehicle emissions and job searching. You were always available to help with revisions for writing and presentations and also helped me with all my questions and concerns.

I would like to acknowledge the funding from the South Coast Air Quality Management District (SCAQMD) under contract number 18090 for chapter 2 and chapter 3 work. Also, The National Center for Sustainable Transportation (NCST) Graduate Fellowship and Colin F. Hackett Endowed Engineering Research Award that was provided to me throughout my Ph.D. program. Also thank Professor Roya Bahreini of UCR and Dr. Donna Sueper of Aerodyne Research, Inc. for their valuable help to me with my HR- ToF-

AMS data treatments. In addition, I would also like to thank my final committee member Dr. Don Collins. Finally, I would also like to thank my family and friends for all their support throughout these years, especially my husband Pouya Haratipour for all his endless support and kindness, which has made my journey much more joyful.

ABSTRACT OF THE DISSERTATION

Secondary Aerosol Formation From Mobile Sources and a Biogenic Precursor

by

Sahar Ghadimi

Doctor of Philosophy, Graduate Program in Chemical and Environmental Engineering
University of California, Riverside, March 2023
Dr. David R. Cocker III, Chairperson

Anthropogenic and biogenic are two major air pollutants emitted from human activity and natural sources, respectively that generate primary atmospheric aerosols which are known for their direct or indirect adverse effects. These air pollutants can undergo photooxidation process by natural UV lights during the daytime and produce secondary atmospheric aerosols that adversely affect air quality, human health, visibility, and climate change. This study aided to understand the parameters that affect the secondary aerosol formation from both anthropogenic and biogenic precursors.

In-use diesel and natural gas heavy-duty vehicles (HDVs) are important mobile source emissions in urban areas. Heavy-duty diesel vehicles (HDDV) emit extremely high nitrogen oxide (NO_x) and particulate matter (PM) emissions, while CNG heavy-duty vehicles produce more aged emissions. In this dissertation, we first conducted a comprehensive fuel and aftertreatment system effect analysis on the primary and secondary emissions from HDDVs when operated with hydrogenated vegetable oil (HVO) and ultra-low sulfur diesel (ULSD) fuel on the chassis dynamometer. The SOA formations were then analyzed by collecting and photooxidizing the diluted vehicle exhaust using a 30 m^3 mobile

atmospheric chamber. The results showed that in the vehicles with no selective catalytic reduction (SCR), the secondary aerosol (SA) formations were ~2 times higher for ULSD compared to HVO. Moreover, both primary and secondary compositions were mostly organics for no-SCR vehicles. Then, we tested the primary and secondary emissions from natural gas heavy-duty vehicles equipped with three-way catalysts (TWC) using the same approach. Particulate matter, particle number, and non-methane organic gas (NMOG) emissions were found to be higher for the natural gas vehicles equipped with TWCs compared to diesel vehicles to the diesel trucks equipped with diesel oxidation catalysts (DOC), diesel particulate filters (DPF), and selective catalytic reduction (SCR) systems. The contribution of lubricant oil in the primary emissions of the CNG vehicles led to enhanced SOA formations compared to HDDVs equipped with advanced aftertreatments. The secondary inorganic aerosols were also significantly higher in CNG vehicles.

We also studied the SOA yields and chemical compositions from α-pinene (a biogenic volatile organic compounds) photooxidation in a new 118 m^3 fixed-volume environmental chamber under atmospherically relevant and controlled chemical conditions. The experiments were conducted at fixed branching ratios (β=0, 0.3, and 1.0), which were controlled via continuous NO injection throughout the experiment to resemble real atmospheric conditions. The corresponding classical experiments with variable β values with instantaneous NO injection prior to photooxidation were also performed to compare the SOA yields and gas-phase chemistry. The SOA yields for β=0.3 experiments (Y= 21.47%-30.45%) and β=0 conditions (Y= 20.22%-29.98%) were substantially higher compared to β=1 experiments with elevated NO level. It was found that the higher $RO_2^{\cdot}$

lifetime led to higher SOA yield due to the formation of next generation oxidized peroxy radicals ($R'O_2^{\cdot}$ and $R''O_2^{\cdot}$) from autoxidation reaction. Similarly, in elevated $HO_2^{\cdot}$ /$RO_2^{\cdot}$ conditions the higher SOA yields were obtained. The continuous NO injection method (constant β) revealed lower SOA yield than classical experiments (variable β) at lower initial hydrocarbon (HC) concentration and higher SOA yield at higher HC conditions.

Table of Contents:

List of Tables:

List of Figures:

List of Supplementary Figures:

Chapter 1 : Introduction

Air pollution is the world's largest environmental health threat, causing 4.2 million premature death per year worldwide (WHO, 2019). Anthropogenic and biogenic air pollutants adversely affect public health causing an acceleration in a number of diseases such as asthma, cardiovascular and respiratory diseases, cancer (Cohen et al., 2017).

Anthropogenic air pollutants are emitted from human activities such as fossil fuel combustion from power plants and transportation. These activities produce particulate matter (PM), and gas-phase emission such as nitrogen oxide (NO_x), sulfur oxides (SO_x), carbon dioxide (CO_2), carbon monoxide (CO), and methane (CH_4), which are known for their adverse effects on air pollution, climate change, and health impacts (Kanakidou et al., 2005; Shrivastava et al., 2017; Tuet, Chen, Fok, Champion, & Ng, 2017). On-road heavy-duty diesel vehicles (HDDVs) are important mobile source emissions in urban areas. The PM and NO_x emissions from heavy-duty diesel vehicles (HDDVs) are much higher compared to gasoline vehicles. Consequently, more aggressive preventive policies have been implemented to reduce these emissions (Ban-Weiss et al., 2008; Preble, Harley, & Kirchstetter, 2019). Over the past decades the emissions from heavy-duty diesel vehicles (HDDVs) have decreased substantially, however despite this decrease, they are still major contributors to emissions inventory, especially NO_x emissions (Anenberg et al., 2017).

The major component of atmospheric aerosol is organic aerosol (OA), which contributes largely to the atmospheric fine particulate matter. OA consists of both primary organic aerosol (POA) and secondary organic aerosol (SOA). The POA is emitted from the

combustion sources (e.g., vehicles' tailpipe) whereas the SOA is produced through the photochemical oxidation of gas-phase volatile organic compounds (VOCs) (Goldstein & Galbally, 2007; Robinson et al., 2007; Zhao et al., 2014). Unlike primary emissions, secondary aerosols are not regulated by environmental agencies. However, it has been illustrated that the secondary aerosol is the major constituent of ambient aerosol mass. Several studies have stated that the HDDVs and HDD engines are an important contributor to SOA formations from mobile sources in urban areas (Chirico et al., 2010; Deng et al., 2017; Gordon et al., 2014). However, a dramatic reductions in both PM emissions and SOA formations were reported for HDDVs equipped with advanced aftertreatment systems such as diesel particulate filter (DPF), diesel oxidation catalyst (DOC), and selective catalytic reduction (SCR) (Ghadimi, Zhu, Durbin, Cocker, & Karavalakis, 2022; Gordon et al., 2014). In addition to exhaust aftertreatments, improvement in the fuel quality, have positive impacts on PM and NO_x emissions from the HDDVs (Ghadimi et al., 2022). For on-road diesel engines, hydrogenated vegetable oil (HVO; also known as renewable diesel) has received a growing interest in recent years (Bohl, Smallbone, Tian, & Roskilly, 2018; Pirjola et al., 2019). HVO is a non-oxygenated, highly paraffinic, and free of aromatic and sulfur compounds fuel produced from vegetable oils and animal fats through hydrogenation of the double bonds in the fatty acids into straight chain alkanes (Singh, Subramanian, & Garg, 2018). Little is known about the impact of HVO fuel on SOA production and compositions when using in HDD engines.

Chapter 3 of this dissertation is seeking to expand the understanding of the secondary aerosol formation from on-road HDDVs with different exhaust aftertreatment

controls when operating with pure HVO and diesel fuel (ULSD) on chassis dynamometer. The pre-2010 model year HDDV was not equipped with an SCR system, while the 2016 HDDV was equipped with a DOC/DPF and SCR aftertreatment systems to meet the stringent NO_x emissions standards for 2010 and later engines. The vehicles were exercised over cold-start driving cycles. Primary gaseous and particulate emissions were also measured to better understand the impact of HVO on tailpipe emissions. Secondary aerosol production was evaluated using a 30 m^3 environmental chamber. Results are discussed as a function of engine technology and fuel type on both the primary emissions and SOA production.

Stoichiometric compressed natural gas (CNG) engines, especially those certified to 0.02 g/bhp-hr of NO_x emissions, have been shown to achieve significant NO_x reductions with additional reductions in PM and VOC emissions when equipped with TWC aftertreatment technology (McCaffery et al., 2021). These advances in fuel, engine technology and aftertreatment systems are critical to reduce other gas-phase emissions and PM formations. Several studies have evaluated the SOA formation from light-duty gasoline vehicles (Roth et al., 2020; Vu et al., 2019) and HDDVs and HDD engines (Ghadimi et al., 2022; Gordon et al., 2014); however, less is known regarding the impact of CNG vehicles on precursor emissions and SOA formation. There has been limited studies that evaluated the fresh and aged CNG vehicles emissions using different techniques rather than standard smog chamber conditions. These studies used remote sensing devices to capture and analyze vehicle plume for fresh and aged emissions when vehicles were passing through a sampling station. Watne *et al*. found little difference between aged and fresh emissions

from the tested CNG vehicles (Watne et al., 2018). Le Breton *et al.* analyzed the emissions using PAM reactor and stated that the aged emissions were higher than fresh emissions (Le Breton et al., 2019). Alanen *et al.* studied a retrofitted natural gas engine under steady state conditions using PAM reactor and stated that the SOA formations from these engines were at the same level or lower compared to diesel or gasoline engines (Alanen et al., 2017).

In chapter 4 of this dissertation, the primary and secondary aerosol formation from in-use CNG heavy-duty vehicles of different vocations were investigated when operated on a chassis dynamometer over multiple driving cycles and compared with HDDVs. Two HDDVs and six CNG vehicles were exercised over realistic driving cycles. Primary precursor emissions were collected in a 30 m^3 environmental chamber and underwent a photochemical oxidation reaction for SOA and secondary inorganic aerosol formation. The effect of fuel type, aftertreatment, and engine technology on CNG vehicles primary and secondary emissions was reported and compared to on-highway HDDVs.

Air pollutants are emitted not only from anthropogenic but also from natural sources. On a global scale, natural sources outweigh those from human activity (Wang et al., 2022). Organic aerosol (OA) accounts for 50% of the submicron ambient aerosol mass, mainly secondary organic aerosols (SOA) (Jimenez et al., 2009). Biogenic volatile organic compounds (BVOCs), such as monoterpenes ($C_{10}H_{16}$) are some of the most important contributors to atmospheric secondary organic aerosol emissions due to their combined emissions rates and propensity to form SOA (Ng et al., 2007). α-Pinene monoterpene is mainly found in the resins of pine trees and is a major contributor to primary biogenic hydrocarbon emission in the atmosphere that accounts for roughly 25.5 Tg yr^{-1}

(Sindelarova et al., 2022; Zhang, Shaw, Seinfeld, & Flagan, 1992). Monoterpenes are mainly oxidized by hydroxyl radicals ($\cdot OH$), ozone (O_3) and nitrate (NO_3^-) to form low volatile secondary organics and subsequent SOA (Guenther et al., 1995).

The hydroxyl radicals ($\cdot OH$) reacts with the endocyclic double bound of the α-pinene, followed by reaction with the O_2 leading to the formation of hydroxy peroxy radicals (known as $RO_2^\cdot$) (Eddingsaas, Loza, Yee, Seinfeld, & Wennberg, 2012; Piletic & Kleindienst, 2022). Based on different atmospheric conditions $RO_2^\cdot$ react with different species, including, $HO_2^\cdot$, NO, and other $RO_2^\cdot$ radicals. When $RO_2^\cdot$ liftetime is long enough it can undergo an intramolecular H-shift isomerization and subsequent O_2 addition (the whole process known as autoxidation) (Lee et al., 2023; Moller, Otkjaer, Chen, & Kjaergaard, 2020; Piletic & Kleindienst, 2022; Xu et al., 2019) to form second generation of oxidized peroxy radicals (named as $R'O_2^\cdot$ in this work, also known as $RO_5^\cdot$) and subsequently the third generation oxidized peroxy radicals (named as $R''O_2^\cdot$ in this work, also known as $RO_7^\cdot$), which accounts for 5.8% to 4.6% of α-Pinene consumption (Piletic & Kleindienst, 2022). These next generation of oxidized peroxy radicals products highly oxygenated organic molecules (HOMs) with lower vapor pressure.

SOA yield (Y) is a measure of the amount of SOA formed from consumption of a certain amount of the precursor hydrocarbon and is defined as the SOA mass formed at the end of the experiment (ΔM_0) divided by the total consumed SOA precursor (ΔHC) **(Equation 1.1).**

$$Y = \frac{\Delta M_0}{\Delta HC} \qquad \textbf{Equation 1.1}$$

SOA yield is highly dependent on atmospheric conditions, which one these conditions is NO_x levels (Ng et al., 2007). The NO_x levels affect SOA yields by altering the $RO_2^{\cdot}$ fate and thus the distribution of oxidation products. For instance, under low- NO conditions, $RO_2^{\cdot}$ tend to react more with $HO_2^{\cdot}$ To form lower volatility products. The products formed under $RO_2^{\cdot}+HO_2^{\cdot}$ Are low volatile organics containing hydroxy -OH, hydroperoxide -OOH, carbonyl -C=O, carboxylic acid O=C-OH and peroxyacid O=C-OOH functional groups (Eddingsaas, Loza, Yee, Chan, et al., 2012). Eddingsaas *et al.* reported that the first generation of oxidation products are α-pinene hydroxy hydroperoxides and pinonaldehyde and stated that only under low NO_x conditions the pinonaldehyde undergoes further $\cdot OH$ oxidation to produce a number of carboxylic acids and selected peroxyacids. These products are important low-volatile secondary organic components that form SOA (Eddingsaas, Loza, Yee, Chan, et al., 2012; Eddingsaas, Loza, Yee, Seinfeld, et al., 2012). Eddingsaas *et al.* also chemically analyzed the products that were formed under high NO_x conditions and mentioned that α-pinene and pinonaldehyde converted to organonitrates and peroxyacyl nitrates. These products are more volatile compared to the products that are formed under low NO conditions. According to Piletic *et al.*, high NO conditions suppresses the formation of next generation oxidized peroxy radicals ($R'O_2^{\cdot}$ and $R''O_2^{\cdot}$) (Piletic & Kleindienst, 2022). Piletic *et al.*, have reported that at lower than 10 ppb of NO the formation of next generation oxidized peroxy radicals ($R'O_2^{\cdot}$ and $R''O_2^{\cdot}$) from autoxidation reaction was higher and dramatically falloffs at about >10 ppb NO concentration (Piletic & Kleindienst, 2022).

The competition of $RO_2^{\cdot}$ Reaction between two different pathways NO or $HO_2^{\cdot}$ is defined by "branching ratio" (β) which is the ratio of NO + $RO_2^{\cdot}$ reaction rate over the total $RO_2^{\cdot}$ decay rate (in both NO and $HO_2^{\cdot}$ pathways) **(Equation 1.2).**

$$\beta = \frac{k_{RO_2+NO}[NO]}{k_{RO_2+NO}[NO]+k_{RO_2+HO_2}[HO_2]} \qquad \textbf{Equation 1.2}$$

Over the last two decades, there has been many studies on SOA formation potentials using biogenic precursors, especially α-pinene. However, most previous BVOC-NO_x studies have injected the NO instantaneously at the beginning of the experiments (Aruffo et al., 2022; Capouet et al., 2008; Capouet, Peeters, Noziere, & Muller, 2004; Ng et al., 2007). Under all these conditions the β value will decrease from ~1 to ~0 at the beginning of the experiment. However, Porter *et al.* modelled the mean atmospheric β values for different regions using GOES-Chem and reported that the β value remains constant throughout most of the day, and depending on the NO ls coming from anthropogenic sources it can vary from 0.25 to 0.75 (Porter, Jimenez, & Barsanti, 2021).

In chapter 5 of this dissertation, the SOA yield from α-pinene precursor as a biogenic emission was evaluated using controlled continuous NO injections to obtain constant branching ratio (β value) throughout the experiment which resemble real atmospheric conditions. All experiments were performed under 3 different branching ratios (β): 1) β equals to zero as no NO experiments, 2) β equals to 0.3 and 3) β equals to 1.0 as high NO experiments. Then, the SOA yields from these experiments were compared to the results from corresponding traditional VOC-NO_x experiments where NO was injected

instantaneously prior to photooxidation process. The outcomes of this novel study were used in GEOS-Chem simulation to develop a more accurate atmospheric SOA model.

References:

Alanen, J., Simonen, P., Saarikoski, S., Timonen, H., Kangasniemi, O., Saukko, E., . . . Rönkkö, T. (2017). Comparison of primary and secondary particle formation from natural gas engine exhaust and of their volatility characteristics. *Atmospheric Chemistry and Physics, 17*(14), 8739-8755. doi:10.5194/acp-17-8739-2017

Anenberg, S. C., Miller, J., Minjares, R., Du, L., Henze, D. K., Lacey, F., . . . Heyes, C. (2017). Impacts and mitigation of excess diesel-related NO(x) emissions in 11 major vehicle markets. *Nature, 545*(7655), 467-471. doi:10.1038/nature22086

Aruffo, E., Wang, J., Ye, J., Ohno, P., Qin, Y., Stewart, M., . . . Martin, S. T. (2022). Partitioning of Organonitrates in the Production of Secondary Organic Aerosols from alpha-Pinene Photo-Oxidation. *Environmental Science & Technology, 56*(9), 5421-5429. doi:10.1021/acs.est.1c08380

Ban-Weiss, G. A., McLaughlin, J. P., Harley, R. A., Kean, A. J., Grosjean, E., & Grosjean, D. (2008). Carbonyl and nitrogen dioxide emissions from gasoline- and diesel-powered motor vehicles. *Environmental Science & Technology, 42*(11), 3944-3950. doi:10.1021/es8002487

Bohl, T., Smallbone, A., Tian, G., & Roskilly, A. P. (2018). Particulate number and NO trade-off comparisons between HVO and mineral diesel in HD applications. *Fuel, 215*, 90-101. doi:10.1016/j.fuel.2017.11.023

Capouet, M., Müller, J. F., Ceulemans, K., Compernolle, S., Vereecken, L., & Peeters, J. (2008). Modeling aerosol formation in alpha-pinene photo-oxidation experiments. *Journal of Geophysical Research, 113*(D2), D02308. doi:10.1029/2007jd008995

Capouet, M., Peeters, J., Noziere, B., & Muller, J. F. (2004). Alpha-pinene oxidation by OH: simulations of laboratory experiments. *Atmospheric Chemistry and Physics, 4*(4), 2285-2311. doi:DOI 10.5194/acp-4-2285-2004

Chirico, R., DeCarlo, P. F., Heringa, M. F., Tritscher, T., Richter, R., Prévôt, A. S. H., . . . Baltensperger, U. (2010). Impact of aftertreatment devices on primary emissions and secondary organic aerosol formation potential from in-use diesel vehicles: results from smog chamber experiments. *Atmospheric Chemistry and Physics, 10*(23), 11545-11563. doi:10.5194/acp-10-11545-2010

Cohen, A. J., Brauer, M., Burnett, R., Anderson, H. R., Frostad, J., Estep, K., . . . Forouzanfar, M. H. (2017). Estimates and 25-year trends of the global burden of disease attributable to ambient air pollution: an analysis of data from the Global Burden of Diseases Study 2015. *Lancet, 389*(10082), 1907-1918. doi:10.1016/S0140-6736(17)30505-6

Deng, W., Hu, Q., Liu, T., Wang, X., Zhang, Y., Song, W., . . . George, C. (2017). Primary particulate emissions and secondary organic aerosol (SOA) formation from idling diesel vehicle exhaust in China. *Science of The Total Environment, 593-594*, 462-469. doi:10.1016/j.scitotenv.2017.03.088

Eddingsaas, N. C., Loza, C. L., Yee, L. D., Chan, M., Schilling, K. A., Chhabra, P. S., . . . Wennberg, P. O. (2012). α-pinene photooxidation under controlled chemical conditions – Part 2: SOA yield and composition in low- and high-NOx environments. *Atmospheric Chemistry and Physics, 12*(16), 7413-7427. doi:10.5194/acp-12-7413-2012

Eddingsaas, N. C., Loza, C. L., Yee, L. D., Seinfeld, J. H., & Wennberg, P. O. (2012). α-pinene photooxidation under controlled chemical conditions – Part 1: Gas-phase composition in low- and high-NOx environments. *Atmospheric Chemistry and Physics, 12*(14), 6489-6504. doi:10.5194/acp-12-6489-2012

Ghadimi, S., Zhu, H., Durbin, T. D., Cocker, D. R., & Karavalakis, G. (2022). The impact of hydrogenated vegetable oil (HVO) on the formation of secondary organic aerosol (SOA) from in-use heavy-duty diesel vehicles. *Science of The Total Environment, 822*, 153583. doi:10.1016/j.scitotenv.2022.153583

Goldstein, A. H., & Galbally, I. E. (2007). Known and unknown organic constituents in the Earth' s atmosphere. *Environmental Science & Technology, 41*(5), 1514-1521. doi:10.1021/es072476p

Gordon, T. D., Presto, A. A., Nguyen, N. T., Robertson, W. H., Na, K., Sahay, K. N., . . . Robinson, A. L. (2014). Secondary organic aerosol production from diesel vehicle exhaust: impact of aftertreatment, fuel chemistry and driving cycle. *Atmospheric Chemistry and Physics, 14*(9), 4643-4659. doi:10.5194/acp-14-4643-2014

Guenther, A., Hewitt, C. N., Erickson, D., Fall, R., Geron, C., Graedel, T., . . . Zimmerman, P. (1995). A global model of natural volatile organic compound emissions. *Journal of Geophysical Research, 100*(D5), 8873. doi:10.1029/94jd02950

Jimenez, J. L., Canagaratna, M. R., Donahue, N. M., Prevot, A. S., Zhang, Q., Kroll, J. H., . . . Worsnop, D. R. (2009). Evolution of organic aerosols in the atmosphere. *Science, 326*(5959), 1525-1529. doi:10.1126/science.1180353

Kanakidou, M., Seinfeld, J. H., Pandis, S. N., Barnes, I., Dentener, F. J., Facchini, M. C., . . . Wilson, J. (2005). Organic aerosol and global climate modelling: a review. *Atmospheric Chemistry and Physics, 5*(4), 1053-1123. doi:10.5194/acp-5-1053-2005

Le Breton, M., Psichoudaki, M., Hallquist, M., Watne, Å. K., Lutz, A., & Hallquist, Å. M. (2019). Application of a FIGAERO ToF CIMS for on-line characterization of real-

world fresh and aged particle emissions from buses. *Aerosol Science and Technology, 53*(3), 244-259. doi:10.1080/02786826.2019.1566592

Lee, B. H., Iyer, S., Kurtén, T., Varelas, J. G., Luo, J., Thomson, R. J., & Thornton, J. A. (2023). Ring-opening yields and auto-oxidation rates of the resulting peroxy radicals from OH-oxidation of α-pinene and β-pinene. *Environmental Science: Atmospheres, 3*(2), 399-407. doi:10.1039/d2ea00133k

McCaffery, C., Zhu, H., Tang, T., Li, C., Karavalakis, G., Cao, S., . . . Durbin, T. D. (2021). Real-world NOx emissions from heavy-duty diesel, natural gas, and diesel hybrid electric vehicles of different vocations on California roadways. *Science of The Total Environment, 784*, 147224. doi:10.1016/j.scitotenv.2021.147224

Moller, K. H., Otkjaer, R. V., Chen, J., & Kjaergaard, H. G. (2020). Double Bonds Are Key to Fast Unimolecular Reactivity in First-Generation Monoterpene Hydroxy Peroxy Radicals. *The Journal of Physical Chemistry A, 124*(14), 2885-2896. doi:10.1021/acs.jpca.0c01079

Ng, N. L., Chhabra, P. S., Chan, A. W. H., Surratt, J. D., Kroll, J. H., Kwan, A. J., . . . Seinfeld, J. H. (2007). Effect of NOx level on secondary organic aerosol (SOA) formation from the photooxidation of terpenes. *Atmospheric Chemistry and Physics, 7*(19), 5159-5174. doi:DOI 10.5194/acp-7-5159-2007

Piletic, I. R., & Kleindienst, T. E. (2022). Rates and Yields of Unimolecular Reactions Producing Highly Oxidized Peroxy Radicals in the OH-Induced Autoxidation of alpha-Pinene, beta-Pinene, and Limonene. *The Journal of Physical Chemistry A, 126*(1), 88-100. doi:10.1021/acs.jpca.1c07961

Pirjola, L., Kuuluvainen, H., Timonen, H., Saarikoski, S., Teinilä, K., Salo, L., . . . Rönkkö, T. (2019). Potential of renewable fuel to reduce diesel exhaust particle emissions. *Applied Energy, 254*, 113636. doi:10.1016/j.apenergy.2019.113636

Porter, W. C., Jimenez, J. L., & Barsanti, K. C. (2021). Quantifying Atmospheric Parameter Ranges for Ambient Secondary Organic Aerosol Formation. *ACS Earth and Space Chemistry, 5*(9), 2380-2397. doi:10.1021/acsearthspacechem.1c00090

Preble, C. V., Harley, R. A., & Kirchstetter, T. W. (2019). Control Technology-Driven Changes to In-Use Heavy-Duty Diesel Truck Emissions of Nitrogenous Species and Related Environmental Impacts. *Environmental Science & Technology, 53*(24), 14568-14576. doi:10.1021/acs.est.9b04763

Robinson, A. L., Donahue, N. M., Shrivastava, M. K., Weitkamp, E. A., Sage, A. M., Grieshop, A. P., . . . Pandis, S. N. (2007). Rethinking organic aerosols: semivolatile emissions and photochemical aging. *Science, 315*(5816), 1259-1262. doi:10.1126/science.1133061

Roth, P., Yang, J., Peng, W., Cocker, D. R., Durbin, T. D., Asa-Awuku, A., & Karavalakis, G. (2020). Intermediate and high ethanol blends reduce secondary organic aerosol formation from gasoline direct injection vehicles. *Atmospheric Environment, 220*, 117064. doi:10.1016/j.atmosenv.2019.117064

Shrivastava, M., Cappa, C. D., Fan, J., Goldstein, A. H., Guenther, A. B., Jimenez, J. L., . . . Zhang, Q. (2017). Recent advances in understanding secondary organic aerosol: Implications for global climate forcing. *Reviews of Geophysics, 55*(2), 509-559. doi:10.1002/2016rg000540

Sindelarova, K., Markova, J., Simpson, D., Huszar, P., Karlicky, J., Darras, S., & Granier, C. (2022). High-resolution biogenic global emission inventory for the time period 2000–2019 for air quality modelling. *Earth System Science Data, 14*(1), 251-270. doi:10.5194/essd-14-251-2022

Singh, D., Subramanian, K. A., & Garg, M. O. (2018). Comprehensive review of combustion, performance and emissions characteristics of a compression ignition engine fueled with hydroprocessed renewable diesel. *Renewable and Sustainable Energy Reviews, 81*, 2947-2954. doi:10.1016/j.rser.2017.06.104

Tuet, W. Y., Chen, Y., Fok, S., Champion, J. A., & Ng, N. L. (2017). Inflammatory responses to secondary organic aerosols (SOA) generated from biogenic and anthropogenic precursors. *Atmospheric Chemistry and Physics, 17*(18), 11423-11440. doi:10.5194/acp-17-11423-2017

Vu, D., Roth, P., Berte, T., Yang, J., Cocker, D., Durbin, T. D., . . . Asa-Awuku, A. (2019). Using a new Mobile Atmospheric Chamber (MACh) to investigate the formation of secondary aerosols from mobile sources: The case of gasoline direct injection vehicles. *Journal of Aerosol Science, 133*, 1-11. doi:10.1016/j.jaerosci.2019.03.009

Wang, X., Zhang, Y., Tan, Y., Tan, Y., Bai, J., Gu, D., . . . Han, Z. (2022). Effects of light on the emissions of biogenic isoprene and monoterpenes: A review. *Atmospheric Pollution Research, 13*(5), 101397. doi:10.1016/j.apr.2022.101397

Watne, A. K., Psichoudaki, M., Ljungstrom, E., Le Breton, M., Hallquist, M., Jerksjo, M., . . . Hallquist, A. M. (2018). Fresh and Oxidized Emissions from In-Use Transit Buses Running on Diesel, Biodiesel, and CNG. *Environmental Science & Technology, 52*(14), 7720-7728. doi:10.1021/acs.est.8b01394

WHO. (2019). https://www.who.int/health-topics/air-pollution#tab=tab_2. Retrieved from https://www.who.int/health-topics/air-pollution#tab=tab_2

Xu, L., Moller, K. H., Crounse, J. D., Otkjaer, R. V., Kjaergaard, H. G., & Wennberg, P. O. (2019). Unimolecular Reactions of Peroxy Radicals Formed in the Oxidation of

alpha-Pinene and beta-Pinene by Hydroxyl Radicals. *The Journal of Physical Chemistry A, 123*(8), 1661-1674. doi:10.1021/acs.jpca.8b11726

Zhang, S.-H., Shaw, M., Seinfeld, J. H., & Flagan, R. C. (1992). Photochemical aerosol formation from α-pinene- and β-pinene. *Journal of Geophysical Research, 97*(D18), 20717. doi:10.1029/92jd02156

Zhao, Y., Hennigan, C. J., May, A. A., Tkacik, D. S., de Gouw, J. A., Gilman, J. B., . . . Robinson, A. L. (2014). Intermediate-volatility organic compounds: a large source of secondary organic aerosol. *Environmental Science & Technology, 48*(23), 13743-13750. doi:10.1021/es5035188

Chapter 2 : The Impact of Hydrogenated Vegetable Oil (HVO) on the Formation of Secondary Organic Aerosol (SOA) from In-Use Heavy-Duty Diesel Vehicles

Sahar Ghadimi[1,2], Hanwei Zhu[1,2], Thomas D. Durbin[1,2], David R. Cocker[1,2], Georgios Karavalakis[1,2,]

[1]University of California, Bourns College of Engineering, Center for Environmental Research and Technology (CE-CERT), 1084 Columbia Avenue, Riverside, CA, USA

[2]Department of Chemical and Environmental Engineering, Bourns College of Engineering, University of California, Riverside, CA, USA

Abstract

This manuscript contains an assessment of tailpipe emissions and secondary aerosol formation from two in-use heavy-duty diesel vehicles (HDDVs) with different aftertreatment systems when operated with ultra-low sulfur diesel (ULSD) and hydrogenated vegetable oil (HVO) operated on a chassis dynamometer. Secondary aerosol formation was characterized from the HDDVs' diluted exhaust collected and photochemically aged in a 30 m^3 mobile atmospheric chamber. Primary nitrogen oxide (NO_x) and particulate matter (PM) emissions were reduced for both vehicles operating on HVO compared to ULSD. For the vehicles with no selective catalytic reduction (SCR) system, secondary aerosol production was ~2 times higher for ULSD compared to HVO. The composition of primary aerosol was exclusively organic for the vehicle with no SCR

system regardless of fuel type. The composition of secondary aerosol with HVO was primarily organic for the vehicle equipped with diesel particulate filter (DPF)/SCR system; however, when the same vehicle was tested with ULSD, the composition was ~20% organic (80% ammonium nitrate). The results reported here revealed that the in-use vehicle with no-SCR had a non-functioning DPF leading to dramatic increases in secondary aerosol formation when compared to the DPF/SCR vehicle. The high-resolution mass spectra analysis showed that the POA of HVO combustion contained relatively lower portion of CH class compounds (or higher CHO class compounds) compared to ULSD under the similar conditions, which can be rationalized by the higher cetane number of HVO. Substantial growth of oxidized organic aerosol (such as *m/z* 44 peak) were observed after 5 hours of photochemical oxidation, consistent with aged organic aerosols present in the atmosphere. The $C_4H_9^+$ fragment at *m/z* 57 peak was used as a tracer to calculate evolution of secondary organic aerosol formation.

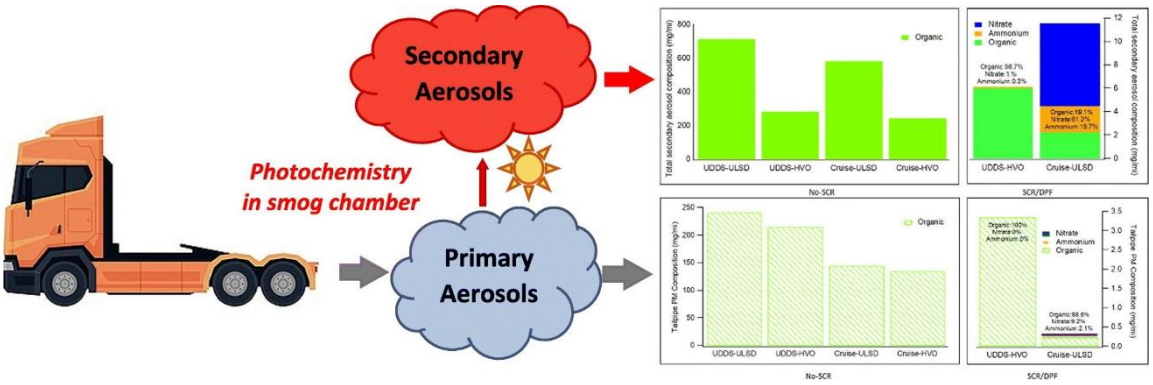

Introduction

Anthropogenic atmospheric aerosols are known for their contribution to air quality and visibility degradation, direct and indirect effects on climate change, and adverse health

effects (Kanakidou et al., 2005) (Tuet, Chen, Fok, Champion, & Ng, 2017) (Shrivastava et al., 2017). Organic aerosol (OA) is a major component of atmospheric aerosol and significantly contributes (fractions ranging from 20-90%) to atmospheric fine particulate matter pn a global scale (Kanakidou et al., 2005). OA consists of primary organic aerosol (POA), which is directly emitted from combustion sources, and secondary organic aerosol (SOA), which is the largest component of the OA budget and can be produced through the photochemical oxidation of gas-phase volatile organic compounds (VOCs), as well as from different organic compound classes, such as semivolatile organic compounds (SVOCs) and intermediate volatility organic compounds (IVOCs) (Robinson et al., 2007) (Goldstein & Galbally, 2007) (Zhao et al., 2014). Gasoline vehicles are major sources of organic compounds, including VOCs, SVOCs, and IVOCs that are known as SOA precursors (Zhao et al., 2016) (Zhao, Lambe, Saleh, Saliba, & Robinson, 2018) (Gentner et al., 2012). Previous studies utilizing environmental chambers and oxidation flow reactors have demonstrated that gasoline vehicles are important contributors to the SOA budget and the formation of secondary inorganic aerosol (Vu et al., 2019) (Simonen et al., 2019) (Zhao et al., 2018) (Nordin et al., 2013).

Heavy-duty diesel vehicles (HDDVs) emit disproportionately more nitrogen oxide (NO_x) and particulate matter (PM) emissions than gasoline vehicles, and therefore more aggressive preventive policies have been enacted in the United States and elsewhere to reduce these pollutants (Preble, Harley, & Kirchstetter, 2019) (Ban-Weiss et al., 2008). These policies have resulted in the widespread adoption of diesel particulate filters (DPFs) to control PM emissions and selective catalytic reduction (SCR) to control NO_x emissions.

HDDVs are also important sources of VOC emissions, comprising a large fraction (approximately 20-60%) of non-methane organic gases (NMOG) and largely depend on engine technology, exhaust aftertreatment, fuel type, and driving conditions (Wang et al., 2020) (Cross, Sappok, Wong, & Kroll, 2015) (George et al., 2014) (Schauer, Kleeman, Cass, & Simoneit, 1999) (Zhao et al., 2015). For example, (Tang et al., 2021) showed that diesel vehicles are major sources of IVOC emissions under real-world conditions that can contribute to SOA formation. Over the past decade, VOC, SVOC, and IVOC emissions in the heavy-duty transportation sector have generally decreased due to the presence of advanced aftertreatment controls in HDDVs. Despite the large reduction in emissions from HDDVs, they are still major contributors to the emissions inventory, especially for NO_x emissions (Anenberg et al., 2017). In addition, studies have shown that diesel combustion engines significantly contribute to the production of localized SOA in urban centers (Dunmore et al., 2015) (Ots et al., 2016) (Gentner et al., 2012). Several studies have investigated SOA formation from HDDVs and HDD engines and have provided evidence that these combustion systems are important sources of SOA formation (Deng et al., 2020) (Gordon et al., 2014) (Nakao, Shrivastava, Nguyen, Jung, & Cocker, 2011) (Deng et al., 2017) (Samy & Zielinska, 2010) (Chirico et al., 2010). For example, (Chirico et al., 2010) reported dramatic reductions in SOA formation for HDDVs equipped with diesel oxidation catalyst (DOC) and DPF systems compared to HDDVs without aftertreatment. (Gordon et al., 2014) showed similar findings of higher SOA formation for the HDDVs without aftertreatment and 3-4 times higher SOA during creep and idle operation compared to the more aggressive UDDS cycle.

In addition to exhaust aftertreatment advancements, important improvements in fuel quality and the introduction of biomass-derived fuels have the potential to provide emission reductions, especially for NO_x and PM emissions. Hydrogenated vegetable oil (HVO) has received a growing interest for use in on-road diesel engines (Pirjola et al., 2019) (Bhardwaj, Kolbeck, Kkoerfer, & Honkanen, 2013) (Bohl, Smallbone, Tian, & Roskilly, 2018). HVO (also known as renewable diesel) is a non-oxygenated, highly paraffinic, and free of aromatic and sulfur compounds fuel produced from vegetable oils and animal fats through hydrogenation of the double bonds in the fatty acids into straight chain alkanes (Singh, Subramanian, & Garg, 2018). A plethora of studies have demonstrated that the use of neat of blended HVO can reduce NOx, carbon monoxide (CO), total hydrocarbons (THC), and PM emissions (Happonen et al., 2012) (Heikkila et al., 2012) (Prokopowicz, Zaciera, Sobczak, Bielaczyc, & Woodburn, 2015) (Bhardwaj et al., 2013; Suarez-Bertoa et al., 2019). Little is known about the impact of HVO on secondary aerosol production, especially from HDDVs. A recent study showed reductions in SOA forming potential with renewable diesel compared to diesel fuel when they aged the exhaust of a 13-liter heavy-duty diesel engine equipped with a DOC and DPF system using an oxidation flow reactor (Gren et al., 2021). Similar findings were reported in a study utilized a non-road diesel engine equipped with various aftertreatment systems on renewable diesel (Karjalainen et al., 2019).

In this study, secondary aerosol formation was characterized for the first time from in-use HDDVs with different exhaust aftertreatment controls when operating with pure HVO and diesel fuel. The pre-2010 model year HDDV was not equipped with an SCR

system, while the 2016 HDDV was equipped with a DOC/DPF and SCR systems to meet the stringent NO_x emissions standards for 2010 and later engines. The vehicles were exercised over cold-start driving cycles using a chassis dynamometer. Primary gaseous and particulate emissions were also measured to better understand the impact of HVO on tailpipe emissions. Secondary aerosol production was evaluated using a 30 m^3 environmental chamber. Results are discussed as a function of engine technology and fuel type on both the primary emissions and SOA production.

Experimental

Vehicles and driving cycle

Two HDDVs were evaluated in this study: a delivery truck and a goods movement vehicle. The delivery truck (herein referred as DPF/SCR HDDV) was equipped with a 2016 Cummins ISL9 330 diesel engines equipped with a DOC, a DPF, a SCR, and an ammonia oxidation catalyst (AMOX). The engine had a displacement of 8.9 liters, a rated horsepower of 320 hp at 2200 rpm, and a torque of 1000 ft-lbs. at 1400 rpm. The goods movement vehicle (herein referred as no-SCR HDDV) was equipped with a 2009 Detroit Diesel DD13 engine equipped with a DOC and a DPF. The engine had a displacement of 12.8 liters, a rated horsepower of 410 hp at 1800 rpm, and a torque of 1450 ft-lbs. at 1200 rpm. Both engines used exhaust gas recirculation (EGR) to control in-cylinder NO_x emissions. The mileages at the start of the campaign were 27,414 and 13,134 for HDV1 and HDV2, respectively. Both vehicles were operated with a typical California ultra-low sulfur diesel (ULSD) and HVO. Some of the main properties are shown in Table S1, Supplementary Material (SM).

Testing was performed over the Urban Dynamometer Driving Schedule (UDDS), which simulates freeway and non-freeway of operation of a heavy-duty vehicle. The cycle covers a distance of 5.55 miles with an average speed of 18.8 miles/hr, and a maximum speed of 58 miles/hr. Testing was also conducted over the Heavy Heavy-Duty Diesel Truck (HHDDT) Cruise cycle, which was developed by the California Air Recourses Board (CARB). The HHDDT Cruise cycle was designed to simulate freeway driving through populated areas. It characterizes vehicles traveling along Highway 99 and Interstate 5, while also accounting for the more congested parts of the highways in the Bay Area and South Coast Basin. The cycle duration is 2083 seconds, with a distance of 23 miles. The average speed over the cycle is about 40 miles/hr with maximum vehicle speeds reaching about 60 miles/hr. Testing on both cycles was performed as a cold-start.

Emissions testing

Testing was performed at CE-CERT's Heavy-Duty Chassis Dynamometer facility, consisting of an electric AC type design chassis dynamometer that can simulate inertia loads from 10,000 lbs. to 80,000 lbs., which covers a broad range of in-use medium and heavy-duty vehicles. Primary emissions measurements were obtained using CE-CERT's Mobile Emissions Laboratory (MEL), with a more detailed description about the facility provided elsewhere (Cocker, Shah, Johnson, Miller, & Norbeck, 2004). Briefly, emission measurements included NO_x, CO, THC, non-methane hydrocarbons (NMHC), carbon dioxide (CO_2), and PM mass. Tailpipe ammonia (NH_3) emissions were obtained with a Horiba Quantum Cascade Laser (QCL) spectroscopy. PM emissions were collected on 47 mm diameter 2 μm pore Teflo filters (Whatman brand). The filters were measured for net

gains using a UMX2 ultra precision microbalance with buoyancy correction in accordance with the weighing procedure guidelines set forth in the Code of Federal Regulations (CFR). Total particle number (TPN) concentrations were measured using a TSI 3776 ultrafine-Condensation Particle Counter (CPC) with detection down to 2.5 nm and operated at a flowrate of 1.5 L/min.

Photochemical oxidation experiments in the chamber

For the chamber experiments, the exhaust of each HDDV was introduced into a 30 m^3 Mobile Atmospheric Chamber (MACh), which is a 2-mil fluorinated ethylene propylene Teflon film reactor. Details on the construction and characterization of MACh are provided elsewhere (Vu et al., 2019). Before the photochemical oxidation experiments, the chamber was repeatably flushed and filled using purified dry air for at least 24 hours until all gases and particles were below detection limits (H_2O < -50°C dew point; NO_x, CO, HC, O_3, and PM being below detection limits). Before the injection of HDDV exhaust, the chamber was half-filled with purified air. The exhaust was injected with two Ejector Dilutors (Air-Vac TD11OH) in parallel, connected to a house-built clean air system with filters and desiccants to remove the PM (HEPA filters), water (silica gel columns), NO_x (Purafil), CO (Carulite canister), and hydrocarbons (activated charcoal) from the house compressed air. At the end of the HDDV testing, the MACh was filled to maximum volume with purified air and primary emissions were characterized for about 30 min. H_2O_2 was then injected to achieve 1.0 ppm concentration into the MACh (for a period of ~15 min) to help initiate the reaction and act as an additional hydroxyl radical source. The chamber enclosure temperature was within 25 ℃-27 ℃ and the relative humidity (RH) was

maintained at <5%. The emissions were then photochemically aged with a controlled ultra-violet (UV) light source of 600 15W 18" black lights mounted onto the walls of the enclosure for at least 5 hours or until particle formation and ozone formation subsided.

The total number and volume of particles were monitored using a scanning mobility particle sizer (SMPS) consisting of a TSI 3080 Electrostatic Classifier, TSI 3081 long column Differential Mobility Analyzer (DMA) column, and a TSI 3776 CPC, which were used to measure the size-resolved number concentrations. Data were corrected for particle wall losses assuming first order wall loss kinetics as described in detail by (Cocker, Flagan, & Seinfeld, 2001). The effective particle density was measured with a Kanomax aerosol particle mass (APM) analyzer, as described in (Malloy et al., 2009).

Table 2.1. Tailpipe emissions for both HDDVs over the UDDS and HHDDT Cruise cycles

Experiment	THC (g/mi)	CO (g/mi)	NMHC (g/mi)	$\mathbf{NO_x}$ (g/mi)	NH_3 (mg/mi)	PM (mg/mi)
UDDS-ULSD (no-SCR)	0.2	1.3	0.2	5.5	0.00	241.4
UDDS-HVO (no-SCR)	0.07	1.2	0.05	5.3	0.00	214.2
Cruise-ULSD (no-SCR)	0.07	0.9	0.06	4.3	0.00	143.9
Cruise-HVO (no-SCR)	0.06	0.9	0.04	4.0	0.00	135.3
UDDS-HVO (SCR/DPF)	0.03	1.8	0.01	2.1	4.30	3.3
Cruise-ULSD (SCR/DPF)	0.01	0.9	0.01	0.6	1.80	0.2

Note that emissions testing over the HHDDT Cruise with HVO and the UDDS with ULSD were not possible due to equipment issues.

An Aerodyne high-resolution time-of-flight aerosol mass spectrometer (HR-ToF-AMS) was used to measure the chemical composition of the non-refractory aerosol. The

HR-ToF-AMS was operated in both V and W modes, and the data processing was completed using the ToF-AMS Analysis Toolkit 1.57 and ToF-AMS HR analysis 1.16. The Unit Mass Resolution (UMR) and HR Frag table for CO_2 were adjusted to the measured CO_2 concentration using a LI-COR ® LI-840A CO_2/H_2O analyzer.

Results and Discussion

Tailpipe gaseous and PM emissions

Tailpipe emissions for both HDDVs over the UDDS and HHDDT Cruise cycles are shown in

Table 2.1. Overall, the gaseous and particulate emissions of the HHDDT Cruise cycle were lower than those of the more transient and lower average speed UDDS. The high speed and load conditions for the HHDDT Cruise cycle led to higher exhaust temperatures and lower NO_x emissions for the SCR-equipped HDDV. NO_x removal efficiencies are higher when exhaust temperatures exceed 250 ℃, which are typically experienced during operation over the HHDDT Cruise cycle (Jiang et al., 2018). Consistent with previous studies, the use of HVO resulted in lower NO_x, CO, THC, and NMHC emissions (Happonen et al., 2012) (Heikkila et al., 2012) (Bohl et al., 2018) (Gren et al., 2021). NO_x reductions were 4% and 8% for the no-SCR HDDT over the UDDS and HDDTT Cruise, respectively, and 9% for the DPF/SCR HDDT over the UDDS. HVO is composed of straight-chain and branched hydrocarbons in the range of C15-C18 (Douvartzides, Charisiou, Papageridis, & Goula, 2019), while diesel fuel also contains cycloparaffins and aromatics, including naphthalene and alkylbenzenes in the C9-C20 range. The high boiling point, heavier fractions in diesel fuel cause higher in-cylinder

temperature and favor the formation of thermal NO_x (Ryoji Nishiumi, 2004). Moreover, the higher cetane number of HVO shortens the ignition delay period reducing NO_x formation rates (Bhardwaj et al., 2013).

Despite the fact that both HDDVs were equipped with a DPF, PM emissions from the older no-SCR HDDV were about 40-60 times higher than the DPF/SCR HDDV over the UDDS. PM emissions over the HHDDT Cruise for the DPF/SCR HDDV were practically zero. Our results indicate that the specific goods movement truck, that was pulled out for testing from an in-use fleet in the South Coast Air Basin (SCAB), was likely equipped with a damaged DPF (i.e., cracked or melted ceramic substrate) or blocked from overloaded soot. Although the condition of this HDDV might not be entirely representative of the SCAB HDDV fleet, HDDVs with damaged or tampered DPFs do represent an important fraction of diesel commercial fleets in the United States and Europe, and emit disproportionally higher PM than HDDVs with properly functioning DPFs (François Boveroux, 2019) (Preble et al., 2019). PM emissions with HVO were lower compared to ULSD, ranging from 11% and 6%, respectively, over the UDDS and HHDDT Cruise for the no-SCR HDDV, and 44% over the UDDS for the DPF/SCR HDDV. Reductions in PM emissions with HVO were likely due to the absence of aromatic and sulfur compounds in the fuel, which are considered major soot precursors (Bhardwaj et al., 2013) (Heikkila et al., 2012).

Primary PM composition

Figure 2.1 shows the tailpipe PM composition for both HDDVs. Organic mass dominated the total PM composition for the DPF/SCR HDDV for both test cycles, ranging

from 88.6% to 100%. Small contributions of nitrate (9.2%) and ammonium (2.1%) were also seen for the ULSD over the HHDDT Cruise for the DPF/SCR HDDV. For the no-SCR HDDV, the total PM composition was exclusively organic for all the experiments. Due to the absence of SCR, there were no NH_3 emissions in the tailpipe to produce ammonium nitrate (NH_4NO_3). It should be noted that the primary emissions from the no-SCR HDDV were lower over the HHDDT Cruise cycle compared to the UDDS, with PM emissions over the UDDS being ~ 1.6 times higher compared to the HHDDT Cruise cycle. The POA particle size distribution data for the no-SCR HDDV showed particle diameters ranging from 60 nm to 350 nm for UDDS-ULSD, 80 nm to 400 nm for Cruise-ULSD, and 100 nm to 450 nm for Cruise-HVO, as shown in **Figure S 2.1**.

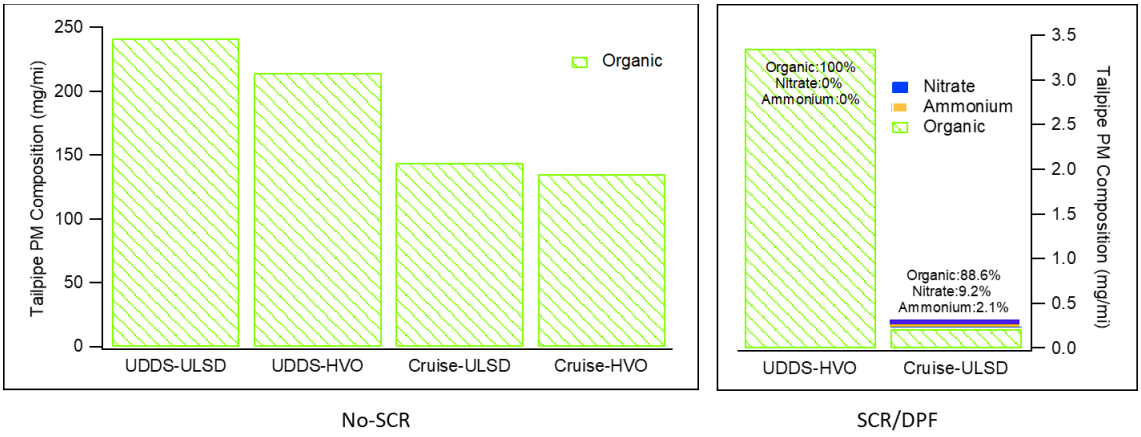

Figure 2.1. Tailpipe PM emissions composition from the no-SCR and SCR/DPF equipped HDDVs. Note the different y-axis scales for the no-SCR and SCR/DPF HDDVs. Chamber data unavailable for Cruise-HVO and UDDS-ULSD for the SCR/DPF HDDV.

Secondary aerosol composition

Figure 2.2 shows the total secondary aerosol mass composition after 300 min of photochemical oxidation in the environmental chamber. Clearly, total secondary aerosol mass significantly exceeded primary PM emissions for both HDDVs on a milligram per

mile basis. For the DPF/SCR HDDV, secondary aerosol mass was 48.4 and 1.8 times higher than primary PM for the HHDDT Cruise running with ULSD fuel and UDDS running with HVO fuel, respectively. Although direct comparisons between fuels cannot be made, the results indicate lower formation of total secondary aerosol mass for the HVO compared to ULSD. The use of HVO fuel resulted almost exclusively in organic secondary aerosols (98.7%), while the use of ULSD showed secondary aerosol comprising of 19% organics, 19.7% ammonium, and 61.2% nitrate. The higher amount of total OA in the UDDS-HVO (SCR/DPF) experiment compared to Cruise-ULSD (SCR/DPF) was consistent with the tailpipe THC emissions (

Table **2.1**). The particle size distribution of OA at 5 hours of photochemical oxidation for the no-SCR HDDV showed unimodal particle size distributions for both fuels with average diameters of ~150 nm for UDDS-ULSD, ~200 nm for Cruise-ULSD, and ~250 nm for Cruise-HVO. The primary particles were large enough that the condensation of photochemically aged species did not dramatically change the particle size distribution **(Figure S 2.1)**. Likewise, the number concentration of particles did not increase over time, which indicated that the formation of new particles was minimal.

The observation of elevated ammonium nitrate formation over the HHDDT Cruise cannot be attributed to higher tailpipe NH_3 emissions. On the contrary, tailpipe NH_3 emissions for HVO over the UDDS were more than double those of ULSD, but with almost negligible ammonium nitrate formation for this fuel. This is not a typical finding, since higher tailpipe NH_3 contributes to elevated ammonium nitrate formation (Link et al., 2017). For the no-SCR HDDV over the UDDS, secondary aerosol mass was 3 and 1.3 times higher

than primary PM for the ULSD and HVO, respectively, while over the HHDDT Cruise secondary aerosol was 4.1 and 1.8 times higher than primary PM for ULSD and HVO, respectively. There was a strong fuel effect for both test cycles, with ULSD resulting to 2.5 times and 2.4 times higher total secondary aerosol mass than HVO over the UDDS and HHDDT Cruise, respectively. The main contribution to secondary aerosol mass was exclusively organic aerosol for both tests since there are no mechanisms for NH_3 formation without SCR system (NH_3 is not a combustion by-product).

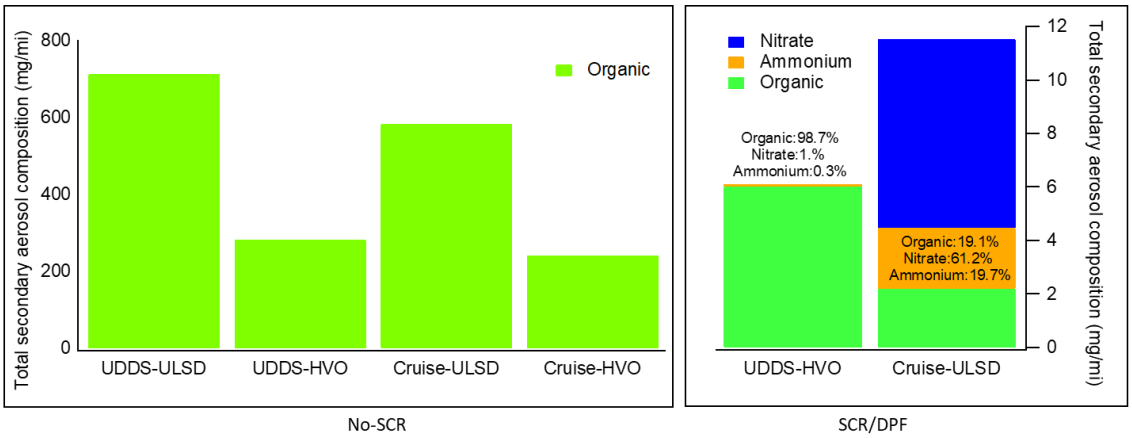

Figure 2.2: Chemical composition of secondary aerosol after 5 hours of photochemical oxidation for the no-SCR and SCR/DPF equipped HDDVs. Note the different y-axis scales for the no-SCR and SCR/DPF HDDVs.

POA versus SOA

Figure 2.3 shows the POA versus SOA for both HDDVs. The DPF/SCR HDDV showed substantially lower SOA production than the older no-SCR HDDV. Although both vehicles were equipped with DOCs, the newer vehicle with a less-aged DOC demonstrated more efficient oxidation of the NMHC emissions (including semi- and intermediate volatility hydrocarbons), which are known as SOA precursors. **Figure S 2.2** shows a reasonable correlation between the tailpipe NMHC emissions and SOA mass (R^2 ~ 0.7).

For the DPF/SCR HDDV, SOA mass for HVO over the UDDS was 2.68 mg/mile compared to 1.99 mg/mile for ULSD over the HHDDT Cruise. The use of ULSD in the no-SCR HDDV produced more SOA mass compared to HVO over both test cycles (UDDS: 470.6 mg/mile and 68.4 mg/mile for the ULSD and HVO, respectively; HHDDT Cruise: 439.0 mg/mile and 107.6 mg/mile for the ULSD and HVO, respectively). Approximately 90.4% of the total carbonaceous aerosol at the end of photochemical oxidation was SOA for the DPF/SCR HDDV on ULSD, while for the no-SCR HDDV on ULSD 75.3%-66.1% of the total carbonaceous aerosol was SOA.

The lower SOA production with HVO is consistent with the lower NMHC emissions for this fuel relative to ULSD due to the absence of aromatic hydrocarbons in HVO. Emissions of aromatic species are strongly associated with SOA formation. Previous studies have suggested that aromatic IVOCs are significant SOA precursors from diesel vehicles (Zhao et al., 2015) (Gentner et al., 2017). Therefore, the lower SOA formation with HVO was likely due to the reduction of aromatic precursor emissions. However, HVO typically includes some large hydrocarbons (i.e., alkanes) with high vaporization enthalpies and relatively high sooting propensities, which can provide different pathways than aromatic compounds for the generation of SOA precursors during combustion.

Total organic aerosol formation during operation over the HHDDT Cruise cycle was lower compared to the UDDS. This is attributed to the higher speed and load conditions of the CARB HHDDT cycle, which led to higher combustion and exhaust temperatures, and the enhanced in-cylinder oxidation of hydrocarbon species (including SOA precursors), as well as the more efficient operation of the DOC to oxidize these species.

The results reported here reveal that the non-functioning DPF for the no-SCR HDDV also played a key role in SOA formation. While the primary function of a DPF is to control PM emissions, DPFs are also capable of oxidizing semivolatile and intermediate volatility hydrocarbons that can contribute to SOA formation. Gordon *et al.* (2014) reported negligible SOA formation from DOC/DPF-equipped HDDVs. Here, SOA formation from the DPF/SCR HDDV was non-negligible, although dramatically lower SOA formation was observed relative to the no-SCR HDDV. Our results support the expectation that SOA formation will likely be mitigated from modern HDDVs with fully functioning aftertreatment systems, but also suggest that elevated SOA will still be formed from HDDVs with nonfunctional or tampered aftertreatment systems.

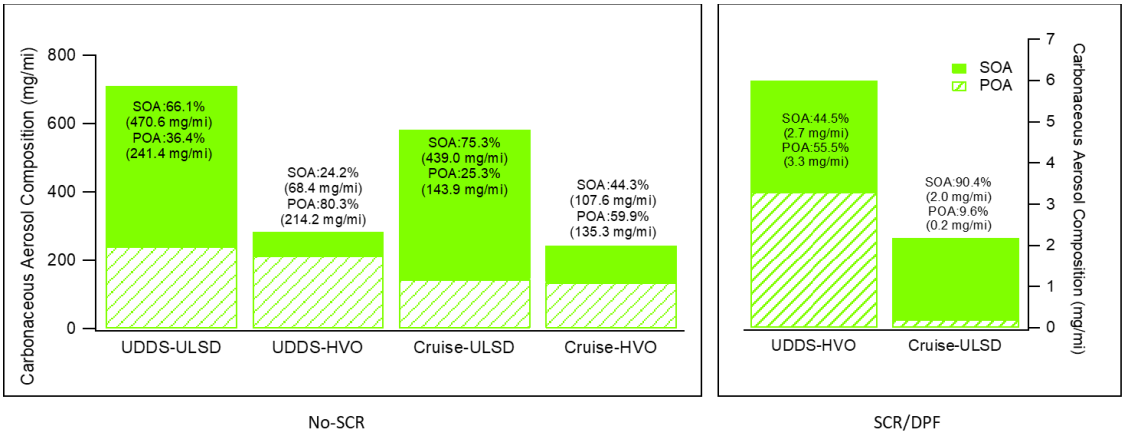

Figure 2.3. Carbonaceous aerosol composition after 5 hours of photochemical oxidation for the no-SCR and SCR/DPF equipped HDDVs. Note the different y-axis scales for the no-SCR and SCR/DPF HDDVs.

High-resolution mass spectra analysis of primary and secondary aerosols

Figure 2.4 (a-c) shows the average normalized high-resolution mass spectra of POA (**Figure 2.4** (a_1-c_1)) and OA(5h) (total organic aerosol after 5 hours photochemical oxidation) (**Figure 2.4** (a_2-c_2)), respectively, for the no-SCR HDDV on ULSD over the

HHDDT Cruise cycle and UDDS cycle, and HVO over the HHDDT Cruise cycle. POA was dominated by the organic CH class (ranging from 72.2% to 82.3%) in all experiments, followed by the CHO class (ranging from 17.7% to 25.7%) (**Figure 2.4** (a_1-c_1)). High-resolution mass spectra revealed that the CH class was predominantly comprised of saturated alkane fragments ($C_nH_{2n+1}^+$ family, alkyls: *m/z* 29, 43, 57, etc.) and unsaturated alkene/cycloalkane fragments ($C_nH_{2n-1}^+$ family, alkenyls/cycloalkyls: *m/z* 27, 41, 55, etc.), which mainly arise from unburned fuel fragments escaping the exhausts, especially during cold-start conditions. These hydrocarbon fragments are dominated by the ultrafine mode, which has been previously observed in ambient air as major peaks originating from vehicles during rush hours in urban areas (Allan, Delia, et al., 2004) (Allan, Bower, et al., 2004) (Zhang et al., 2004). POA of HVO (**Figure 2.4** c_1) contained a relatively lower fraction of CH class compounds (or higher fraction of CHO class) compared to ULSD over the HHDDT Cruise cycle (**Figure 2.4** b_1), which is attributed to the higher cetane number of HVO (see Table S1; $CN_{(HVO)}$ = ~80, $CN_{(ULSD)}$ = ~48) leading to lower emissions of unburned hydrocarbons (**Figure 2.4** (b-c)). Similarly, detailed chemical analysis of HVO (and ULSD) PM emissions over the HHDDT Cruise cycle illustrated that 8.1% (9.3%) and 7.5% (8.6%) of the total POA were comprised by *m/z* 43 and *m/z* 57 fragments, of which 86.4% (86.9%) and 93.2% (95.4%) can be assigned to $C_3H_7^+$ and $C_4H_9^+$ ion fragments, respectively. This finding agrees with the more unsaturated hydrocarbons present in ULSD compared to HVO (13.9% H_2 and 86.3% C for ULSD vs. 15% H_2 and 84.9% C for HVO), as represented by the $C_3H_7^+$ and $C_4H_9^+$ ion fragments. Likewise, detailed chemical analysis of unsaturated hydrocarbons in POA from the HDDV operating on HVO (and ULSD) over

the HHDDT Cruise cycle illustrated that 7.7% (8.8%) and 5.6% (6.9%) of the total POA was comprised by *m/z* 41 and *m/z* 55 fragments, of which 97.8% (99.5%) and 90.0% (92.8%) can be assigned to $C_3H_5^+$ and $C_4H_7^+$ unsaturated ion fragments, respectively. The abovementioned percentage values of the saturated and unsaturated hydrocarbon ion fragments suggest that HVO exhibited better burning properties compared to ULSD, which led to lower unburned hydrocarbons and subsequently lower POA emissions for similar operating conditions.

Hydrogen cyanide (HCN) and isocyanic acid (HNCO) from vehicle exhaust are two important members of the CHN and CHNO classes that are associated with adverse health effects (Moussa et al., 2016). They are produced in catalyst systems or via fuel combustion pathways (Dagaut, Glarborg, & Alzueta, 2008). Generally, the portion of CHN and CHNO classes in organic aerosol compositions was very low, similar to what was reported in other studies (Nakao et al., 2011) (Chirico et al., 2010) (Sage, Weitkamp, Robinson, & Donahue, 2008). The percent of CHN and CHNO classes in POA from both ULSD tests (**Figure 2.4** (a_1-b_1); $CHN_{(ULSD)}$: 3.4%-0.04%, $CHNO_{(ULSD)}$: 0.78%-0.04%) exceeded the HVO test (**Figure 2.4** c_1; $CHN_{(HVO)}$: 0.00%, $CHNO_{(ULSD)}$: 0.00%) consistent with the higher nitrogen content of ULSD fuel (see Table S1; $N_{(ULSD)}$ = 4.9 ppm, $N_{(HVO)}$ = <1.0 ppm). Primary aerosol data from the ULSD-UDDS experiment showed that the HCN fragment was composed of 17.7% of the total *m/z* 27 and 8.8% of CHN class, while HNCO was 12.5% of the CHNO class. Therefore, POA emissions obtained from HVO combustion may be less toxic than those of ULSD. The effect of the driving cycle on the chemical composition of the emissions was more pronounced for the CHN class. Higher fractions of

CHN class compounds (both POA and OA(5h)) were observed for the UDDS experiment (3.4% CHN in POA and 6.9% in OA(5h)) compared to the HHDDT Cruise experiment (0.04% CHN in POA and 0.2% in OA(5h)) using ULSD fuel (**Figure 2.4** (a_1, b_1, a_2 and b_2)). This result is supported by the elemental analysis of the test fuels **(Table S 2.1)**.

The CHO class in organic aerosols increased (**Figure 2.4** (a_2-c_2)) from 26.0% to 31.5% of OA after 5 hours of aging while and the percentage of CH class decreased to 61.3% - 73.7% of OA. The increase of CHO occurs as gas-phase organic emissions (e.g., unburnt hydrocarbons, classified as THC/NMHC) are oxidized to produce lower-volatility oxygenated organics that condense to form SOA. Chemical analysis of organic aerosols from HVO (and ULSD) exhaust emissions over the HHDDT Cruise cycle illustrated that 7.0% (8.1%) of the total POA was comprised by the $C_4H_9^+$ ion fragment, while after photochemical oxidation the peak intensities decreased to 3.7% (2.5%) of total OA(5h) as oxidized hydrocarbons formed SOA reducing the fraction of POA present in the chamber. This is consistent with the observation of greater decreases in the percent $C_4H_9^+$ ion in the ULSD experiment with larger SOA formation compared to decreases in the $C_4H_9^+$ ion in the HVO. Analysis of unsaturated ion fragments from HVO (and ULSD) exhaust emissions over the HHDDT Cruise cycle illustrated that 5.0% (5.5%) of the total POA was comprised of the $C_4H_7^+$ ion fragment, while after photochemical oxidation and SOA formation, the peak intensities decreased to 3.3% (2.7%). Similar to previous chamber studies with diesel engines/vehicles, the mass spectra analysis of all experiments clearly indicated that the CH family compounds progressively oxidized during photochemical oxidation (Nakao et al., 2011) (Chirico et al., 2010) (Sage et al., 2008).

After 5 hours photochemical oxidation (**Figure 2.4** (a_2-c_2)) the *m/z* 44 peak showed a large increase due to the increase of CO_2^+ ion fragments associated with heavily oxidized organics that contain mono- or poly-carboxylic acid functional group(s). Similar phenomena have been reported by (Chirico et al., 2010), showing that *m/z* 44 was one of the most prominent peaks in OA(5h) spectra. These highly oxidized organic species in SOA are observed routinely in urban areas (in accumulation mode), especially during an episode of intensive photochemistry (Allan, Bower, et al., 2004) (Allan, Delia, et al., 2004) (Zhang et al., 2004). For the HVO (and ULSD) exhaust emissions over the HHDDT Cruise cycle, the contribution of the CO_2^+ ion fragment increased from 11.5% (15.7%) in POA to 13.8% (34.2%) in the OA(5h), consistent with the higher SOA formation in the ULSD combustion experiment compared to the HVO for the HHDDT Cruise cycle (**Figure 2.3**). The peak at *m/z* 44 almost doubled from 8.8% in POA to 15.7% in OA(5h) for the UDDS-ULSD experiment, with 89.4% of this signal attributed to CO_2^+ and 5.7% to $C_2H_6N^+$ in POA and 71.8% attributed to CO_2^+ and 22.4% to $C_2H_6N^+$ in OA(5h). These nitrogen-containing organics at OA(5h) were attributed to the high concentrations of nitrogenous gases in the chamber for the ULSD experiment over the UDDS.

Other oxygenated organics, such aldehydes and ketones were formed during the photo-oxidation experiments, which contain a lower oxidation state (compare to carboxylic acid compounds) and appear as $C_2H_3O^+$ and $C_3H_5O^+$ for *m/z* 43 and *m/z* 57, respectively. The contribution of $C_3H_5O^+$ in *m/z* 57 peak increased from 3.4% (0.5%) in POA to 7.2% (14.6%) in OA(5h) for HVO (and ULSD) fuels over the HHDDT Cruise cycle emissions;

the greater increase for the ULSD fuel is consistent with the aforementioned higher observed SOA formation for the vehicles operated with ULSD (**Figure 2.3**).

Analysis of aromatics in POA and OA(5h) illustrated that more aromatic species (*m/z* 77, 110, etc.) were present in ULSD exhaust emissions when compared to HVO, consistent with the higher aromatic mass in the chemical composition of ULSD fuel (9.9%) compared to HVO fuel (1.2%) (Table S1, SM). For example, POA analysis of HVO and ULSD exhaust emissions over the HHDDT Cruise cycle illustrated that the contribution of $C_6H_5^+$ in *m/z* 77 peak was 80.6% and 91.1%, respectively. Similarly, the photochemical aromatic oxidation products such as $C_6H_5O^+$ (in *m/z* 93) and $C_6H_5O_2^+$ (in *m/z* 109) were higher in OA(5h) for the ULSD exhaust emissions compared to HVO experiment, consistent with the greater amount of aromatic mass available in the chemical composition of ULSD.

As illustrated in this section, after 5 hours of photochemical oxidation the overall contribution of *m/z* 57 decreased due to the condensation of highly oxidized species leading to dilution of the $C_4H_9^+$ ion fragment. The fragment $C_4H_9^+$ associated with primary emissions can be used as a tracer of POA allowing for estimation of percent SOA contribution during the course of photochemical aging as %ΔOA(t) (**(Equation** 2.1). The estimated ΔOA% fraction at 5 hours of photochemical oxidation was 81% and 71%, respectively, for ULSD and HVO over the HHDDT Cruise, and 80% for ULSD over the UDDS. Our results agree with those of (Nakao et al., 2011) when they photochemically oxidized the exhaust from a diesel generator and estimated 80% of the final OA to be SOA. The SOA evolution estimated from the fragment $C_4H_9^+$ by %ΔOA (5h) would be

overestimated compared to the SOA in mg per mile shown in **Figure 2.3**, due to wall loss effect (wall loss effects are higher in POA compared to SOA); however, very similar trends were observed in %ΔOA (5h) compared to SOA, showing that higher %ΔOA (5h) value was calculated for ULSD compared to HVO. This difference could be due to not accounting for wall losses in (**Equation 2.1**).

$$\% \, \Delta OA(t) = \frac{[Org(t) - \left(\frac{\% \, C_4H_9^+ \, (t)}{\% \, C_4H_9^+ \, (t_0)}\right) * Org \, (t_0)]}{Org \, (t)} \times 100 \qquad \textbf{(Equation 2.1)}$$

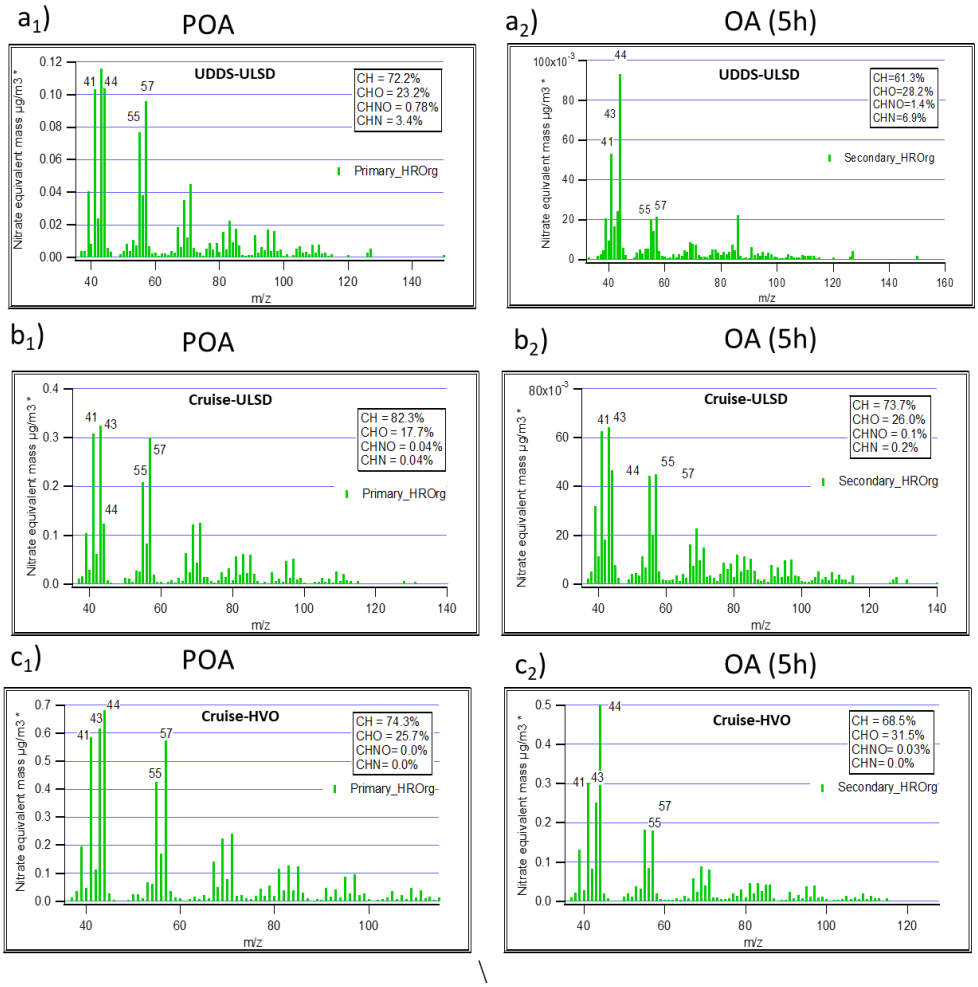

Figure 2.4. Average HR mass spectra of POA, and OA(5h) normalized to the total organic mass: a) UDDS-ULSD (No-SCR HDDV) POA (a_1) and OA(5h) (a_2); b) Cruise-ULSD (No-SCR HDDV) POA (b_1) and OA(5h) (b_2); c) Cruise-HVO (No-SCR HDDV) POA (c_1) and OA(5h) (c_2).

Figure 2.5 shows a Van Krevelen diagram describing the H:C versus O:C bulk atomic ratios for the no-SCR HDDV when operated with ULSD (green lines) and HVO (yellow lines) over the HHDDT Cruise cycle. The slope (m) indicates the oxidation pathway during OA evolution in the chamber with a slope of -2 (m= -2) suggesting the addition of a carbonyl group, a slope of -1 (m= -1) the simultaneous addition of carbonyl and alcohol groups, and the horizontal slope (m= 0) the addition of an alcohol group. The grey dashed lines indicate the carbon oxidation state (Heald et al., 2010). Prior to the photochemical oxidation, the H:C and O:C ratios were 2.06 and 0.11 for the ULSD, and 1.93 and 0.25 for the HVO, respectively, suggesting that POA formed from the vehicle operated with ULSD was less oxygenated. Previous studies of diesel engines have reported primary O:C ratios ranging from about 0.05 to 0.22, indicating the current O:C data being slightly higher but overall within range with past works (Nakao et al., 2011) (Chirico et al., 2010) (Presto, Gordon, & Robinson, 2014). After 5 hours of photochemical oxidation, the H:C and O:C ratios were 1.98 and 0.24 for the ULSD, and 1.88 and 0.32 for the HVO, respectively. The O:C ratio increased during photochemical oxidation for both fuels due to the condensation of oxidized gases onto the diesel agglomerate (Nakao et al., 2011). Comparing the oxidation state of primary species to secondary species for each fuel, the OA(5h) for ULSD exhibited an increase in oxygen content (15% CHO in POA vs. 28% CHO in OA(5h)) compared to HVO (26% CHO in POA vs. 31% CHO on OA(5h)) probably due to higher SOA formation from higher concentration of SOA precursors such as NMHC (

Table 2.1) in the ULSD experiment compared to the corresponding values in HVO experiment (**Figure 2.3**).

The driving cycle effect is visible when comparing the ULSD experiments over the UDDS (blue) and HHDDT Cruise (green). The primary H:C and O:C ratios were 2.24 and 0.21 for the ULSD over the UDDS, which after the photochemical oxidation were transformed to 2.11 and 0.29, respectively. The experiments over the UDDS with ULSD resulted to more oxidized POA and OA(5h) compared to those over the HHDDT Cruise cycle. The higher H:C ratio for both POA and OA(5h) over the UDDS compared to HHDDT Cruise was likely due to the higher CHN species formation for the UDDS (3% in POA and 7.6% in OA(5h) over the UDDS vs. 0.04% in POA and 0.2% in OA(5h) over the HHDDT Cruise). The results reported here agree with previous studies of diesel engines with and without aftertreatment systems using environmental chambers that reported O:C ratios ranged from 0.1 to 0.4 (Nakao et al., 2011) (Chirico et al., 2010) (Jathar et al., 2017).

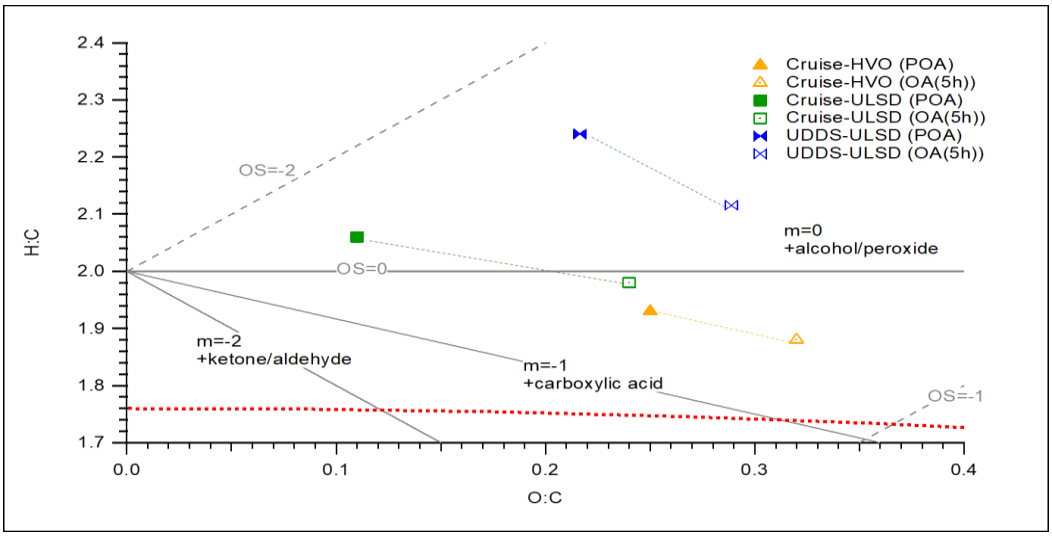

Figure 2.5. Van Krevelen diagram showing the atomic H:C vs. O:C ratios for POA and OA(5h). Data corresponds to the experiments for the no-SCR HDDV fueled with ULSD and HVO.

Conclusions

Primary emissions and secondary aerosol production were characterized from two in-use HDDVs operated with typical ULSD and HVO fuels over the UDDS and HHDDT Cruise cycles on a chassis dynamometer. HVO fuels resulted in lower THC, NO_x, and PM emissions compared to ULSD. The composition of primary PM emissions from both vehicles was dominated by organic mass. Secondary aerosol mass production during photochemical aging significantly exceeded primary PM emissions. The secondary aerosol mass for the DPF/SCR HDDV operated on HVO was almost exclusively comprised of organics (~99%), whereas the ULSD fueled DPF/SCR HDDV produced a substantial amount of secondary inorganic material (~20% ammonium and 61% nitrate). The DPF/SCR HDDV produced substantially lower secondary aerosol mass (lower than 12 mg/mile) compared to the no-SCR HDDV (up to 712 mg/mile) due to the non-functioning DPF, which affected both the primary PM emissions and secondary aerosol formation. Our results suggest that fully functioning DOC/DPF aftertreatment systems will likely decrease the SOA precursor emissions. On the other hand, more attention will be necessary for in-use HDDVs with malfunctioned or tampered aftertreatment devices, which will cause elevated tailpipe emissions and affect local air quality. Overall, this study exhibited that the use of HVO will provide additional benefits on primary emissions and secondary aerosol formation from in-use HDDVs.

Chemical composition analysis of organic aerosols by HR-ToF-AMS for all experiments illustrated that hydrocarbon species (C_xH_y) were dominant in POA, which originated from unburnt fuel. HVO exhaust emissions organic aerosols contained less CH

class compounds (or higher CHO class compounds) compared to ULSD under similar conditions due to higher cetane number of HVO fuel and its better burning properties. Similarly, more aromatic species (*m/z* 77, 110, etc.) were present in ULSD POA emissions compared to HVO due to higher aromatics content in ULSD fuel (9.9%) compared to HVO (1.2%). After 5 hours of photochemical oxidation, substantial growth of oxidized organic aerosols (such as *m/z* 44 peak) provided evidence of significant oxidation and photochemistry similar to what is observed in atmospheric aged organic aerosols. The $C_4H_9^+$ fragment for the *m/z* 57 peak was used as a tracer to calculate evolution of secondary organic aerosol formation during the photochemical oxidation. The percentage of ΔOA(5h) was calculated using $C_4H_9^+$ as a tracer and showed a range of 71% to 81% after 5 hours of irradiation, emphasizing the importance of diesel exhaust as a source of urban SOA, with size distributions dominated by the accumulation mode.

References:

Allan, J. D., Bower, K. N., Coe, H., Boudries, H., Jayne, J. T., Canagaratna, M. R., . . . Worsnop, D. R. (2004). Submicron aerosol composition at Trinidad Head, California, during ITCT 2K2: Its relationship with gas phase volatile organic carbon and assessment of instrument performance. *Journal of Geophysical Research: Atmospheres, 109*(D23), D23S24. doi:10.1029/2003jd004208

Allan, J. D., Delia, A. E., Coe, H., Bower, K. N., Alfarra, M. R., Jimenez, J. L., . . . Worsnop, D. R. (2004). A generalised method for the extraction of chemically resolved mass spectra from Aerodyne aerosol mass spectrometer data. *Journal of Aerosol Science, 35*(7), 909-922. doi:10.1016/j.jaerosci.2004.02.007

Anenberg, S. C., Miller, J., Minjares, R., Du, L., Henze, D. K., Lacey, F., . . . Heyes, C. (2017). Impacts and mitigation of excess diesel-related NO(x) emissions in 11 major vehicle markets. *Nature, 545*(7655), 467-471. doi:10.1038/nature22086

Ban-Weiss, G. A., McLaughlin, J. P., Harley, R. A., Kean, A. J., Grosjean, E., & Grosjean, D. (2008). Carbonyl and nitrogen dioxide emissions from gasoline- and diesel-powered motor vehicles. *Environmental Science & Technology, 42*(11), 3944-3950. doi:10.1021/es8002487

Bhardwaj, O. P., Kolbeck, A. F., Kkoerfer, T., & Honkanen, M. (2013). Potential of Hydrogenated Vegetable Oil (HVO) in Future High Efficiency Combustion System. *SAE International Journal of Fuels and Lubricants, 6*(1), 157-169. doi:10.4271/2013-01-1677

Bohl, T., Smallbone, A., Tian, G., & Roskilly, A. P. (2018). Particulate number and NO trade-off comparisons between HVO and mineral diesel in HD applications. *Fuel, 215*, 90-101. doi:10.1016/j.fuel.2017.11.023

Chirico, R., DeCarlo, P. F., Heringa, M. F., Tritscher, T., Richter, R., Prévôt, A. S. H., . . . Baltensperger, U. (2010). Impact of aftertreatment devices on primary emissions and secondary organic aerosol formation potential from in-use diesel vehicles: results from smog chamber experiments. *Atmospheric Chemistry and Physics, 10*(23), 11545-11563. doi:10.5194/acp-10-11545-2010

Cocker, D. R., 3rd, Flagan, R. C., & Seinfeld, J. H. (2001). State-of-the-art chamber facility for studying atmospheric aerosol chemistry. *Environmental Science & Technology, 35*(12), 2594-2601. doi:10.1021/es0019169

Cocker, D. R., 3rd, Shah, S. D., Johnson, K., Miller, J. W., & Norbeck, J. M. (2004). Development and application of a mobile laboratory for measuring emissions from

diesel engines. 1. Regulated gaseous emissions. *Environmental Science & Technology, 38*(7), 2182-2189. doi:10.1021/es034888d

Cross, E. S., Sappok, A. G., Wong, V. W., & Kroll, J. H. (2015). Load-Dependent Emission Factors and Chemical Characteristics of IVOCs from a Medium-Duty Diesel Engine. *Environmental Science & Technology, 49*(22), 13483-13491. doi:10.1021/acs.est.5b03954

Dagaut, P., Glarborg, P., & Alzueta, M. (2008). The oxidation of hydrogen cyanide and related chemistry. *Progress in Energy and Combustion Science, 34*(1), 1-46. doi:10.1016/j.pecs.2007.02.004

Deng, W., Fang, Z., Wang, Z., Zhu, M., Zhang, Y., Tang, M., . . . Wang, X. (2020). Primary emissions and secondary organic aerosol formation from in-use diesel vehicle exhaust: Comparison between idling and cruise mode. *Science of The Total Environment, 699*, 134357. doi:10.1016/j.scitotenv.2019.134357

Deng, W., Hu, Q., Liu, T., Wang, X., Zhang, Y., Song, W., . . . George, C. (2017). Primary particulate emissions and secondary organic aerosol (SOA) formation from idling diesel vehicle exhaust in China. *Science of The Total Environment, 593-594*, 462-469. doi:10.1016/j.scitotenv.2017.03.088

Douvartzides, S. L., Charisiou, N. D., Papageridis, K. N., & Goula, M. A. (2019). Green Diesel: Biomass Feedstocks, Production Technologies, Catalytic Research, Fuel Properties and Performance in Compression Ignition Internal Combustion Engines. *Energies, 12*(5), 809. doi:10.3390/en12050809

Dunmore, R. E., Hopkins, J. R., Lidster, R. T., Lee, J. D., Evans, M. J., Rickard, A. R., . . . Hamilton, J. F. (2015). Diesel-related hydrocarbons can dominate gas phase reactive carbon in megacities. *Atmospheric Chemistry and Physics, 15*(17), 9983-9996. doi:10.5194/acp-15-9983-2015

François Boveroux, S. C., Pascal Buekenhoudt, Laurent Chavatte, Philippe De Meyer, Hervé Jeanmart, Sebastian Verhelst, Francesco Contin. (2019). Feasibility Study of a New Test Procedure to Identify High Emitters of Particulate Matter during Periodic Technical Inspection doi:10.4271/2019-01-1190

Gentner, D. R., Isaacman, G., Worton, D. R., Chan, A. W., Dallmann, T. R., Davis, L., . . . Goldstein, A. H. (2012). Elucidating secondary organic aerosol from diesel and gasoline vehicles through detailed characterization of organic carbon emissions. *Proceedings of the National Academy of Sciences 109*(45), 18318-18323. doi:10.1073/pnas.1212272109

Gentner, D. R., Jathar, S. H., Gordon, T. D., Bahreini, R., Day, D. A., El Haddad, I., . . . Robinson, A. L. (2017). Review of Urban Secondary Organic Aerosol Formation

from Gasoline and Diesel Motor Vehicle Emissions. *Environmental Science & Technology, 51*(3), 1074-1093. doi:10.1021/acs.est.6b04509

George, I. J., Hays, M. D., Snow, R., Faircloth, J., George, B. J., Long, T., & Baldauf, R. W. (2014). Cold temperature and biodiesel fuel effects on speciated emissions of volatile organic compounds from diesel trucks. *Environmental Science & Technology, 48*(24), 14782-14789. doi:10.1021/es502949a

Goldstein, A. H., & Galbally, I. E. (2007). Known and unknown organic constituents in the Earth' s atmosphere. *Environmental Science & Technology, 41*(5), 1514-1521. doi:10.1021/es072476p

Gordon, T. D., Presto, A. A., Nguyen, N. T., Robertson, W. H., Na, K., Sahay, K. N., . . . Robinson, A. L. (2014). Secondary organic aerosol production from diesel vehicle exhaust: impact of aftertreatment, fuel chemistry and driving cycle. *Atmospheric Chemistry and Physics, 14*(9), 4643-4659. doi:10.5194/acp-14-4643-2014

Gren, L., Malmborg, V. B., Falk, J., Markula, L., Novakovic, M., Shamun, S., . . . Pagels, J. (2021). Effects of renewable fuel and exhaust aftertreatment on primary and secondary emissions from a modern heavy-duty diesel engine. *Journal of Aerosol Science, 156*, 105781. doi:10.1016/j.jaerosci.2021.105781

Happonen, M., Heikkila, J., Murtonen, T., Lehto, K., Sarjovaara, T., Larmi, M., . . . Virtanen, A. (2012). Reductions in particulate and NO(x) emissions by diesel engine parameter adjustments with HVO fuel. *Environmental Science & Technology, 46*(11), 6198-6204. doi:10.1021/es300447t

Heald, C. L., Kroll, J. H., Jimenez, J. L., Docherty, K. S., DeCarlo, P. F., Aiken, A. C., . . . Artaxo, P. (2010). A simplified description of the evolution of organic aerosol composition in the atmosphere. *Geophysical Research Letters, 37*(8), L088032. doi:10.1029/2010gl042737

Heikkila, J., Happonen, M., Murtonen, T., Lehto, K., Sarjovaara, T., Larmi, M., . . . Virtanen, A. (2012). Study of Miller timing on exhaust emissions of a hydrotreated vegetable oil (HVO)-fueled diesel engine. *Journal of the Air & Waste Management Association, 62*(11), 1305-1312. doi:10.1080/10962247.2012.708383

Jathar, S. H., Friedman, B., Galang, A. A., Link, M. F., Brophy, P., Volckens, J., . . . Farmer, D. K. (2017). Linking Load, Fuel, and Emission Controls to Photochemical Production of Secondary Organic Aerosol from a Diesel Engine. *Environmental Science & Technology, 51*(3), 1377-1386. doi:10.1021/acs.est.6b04602

Jiang, Y., Yang, J., Cocker, D., 3rd, Karavalakis, G., Johnson, K. C., & Durbin, T. D. (2018). Characterizing emission rates of regulated pollutants from model year

2012+ heavy-duty diesel vehicles equipped with DPF and SCR systems. *Science of The Total Environment, 619-620,* 765-771. doi:10.1016/j.scitotenv.2017.11.120

Kanakidou, M., Seinfeld, J. H., Pandis, S. N., Barnes, I., Dentener, F. J., Facchini, M. C., . . . Wilson, J. (2005). Organic aerosol and global climate modelling: a review. *Atmospheric Chemistry and Physics, 5*(4), 1053-1123. doi:10.5194/acp-5-1053-2005

Karjalainen, P., Ronkko, T., Simonen, P., Ntziachristos, L., Juuti, P., Timonen, H., . . . Keskinen, J. (2019). Strategies To Diminish the Emissions of Particles and Secondary Aerosol Formation from Diesel Engines. *Environmental Science & Technology, 53*(17), 10408-10416. doi:10.1021/acs.est.9b04073

Link, M. F., Kim, J., Park, G., Lee, T., Park, T., Babar, Z. B., . . . Farmer, D. K. (2017). Elevated production of NH 4 NO 3 from the photochemical processing of vehicle exhaust: Implications for air quality in the Seoul Metropolitan Region. *Atmospheric Environment, 156,* 95-101. doi:10.1016/j.atmosenv.2017.02.031

Malloy, Q. G. J., Nakao, S., Qi, L., Austin, R., Stothers, C., Hagino, H., & Cocker, D. R. (2009). Real-Time Aerosol Density Determination Utilizing a Modified Scanning Mobility Particle Sizer—Aerosol Particle Mass Analyzer System. *Aerosol Science and Technology, 43*(7), 673-678. doi:10.1080/02786820902832960

Moussa, S. G., Leithead, A., Li, S.-M., Chan, T. W., Wentzell, J. J. B., Stroud, C., . . . Liggio, J. (2016). Emissions of hydrogen cyanide from on-road gasoline and diesel vehicles. *Atmospheric Environment, 131*, 185-195. doi:10.1016/j.atmosenv.2016.01.050

Nakao, S., Shrivastava, M., Nguyen, A., Jung, H., & Cocker, D. (2011). Interpretation of Secondary Organic Aerosol Formation from Diesel Exhaust Photooxidation in an Environmental Chamber. *Aerosol Science and Technology, 45*(8), 964-972. doi:10.1080/02786826.2011.573510

Nordin, E. Z., Eriksson, A. C., Roldin, P., Nilsson, P. T., Carlsson, J. E., Kajos, M. K., . . . Pagels, J. H. (2013). Secondary organic aerosol formation from idling gasoline passenger vehicle emissions investigated in a smog chamber. *Atmospheric Chemistry and Physics, 13*(12), 6101-6116. doi:10.5194/acp-13-6101-2013

Ots, R., Young, D. E., Vieno, M., Xu, L., Dunmore, R. E., Allan, J. D., . . . Heal, M. R. (2016). Simulating secondary organic aerosol from missing diesel-related intermediate-volatility organic compound emissions during the Clean Air for London (ClearfLo) campaign. *Atmospheric Chemistry and Physics, 16*(10), 6453-6473. doi:10.5194/acp-16-6453-2016

Pirjola, L., Kuuluvainen, H., Timonen, H., Saarikoski, S., Teinilä, K., Salo, L., . . . Rönkkö, T. (2019). Potential of renewable fuel to reduce diesel exhaust particle emissions. *Applied Energy, 254*, 113636. doi:10.1016/j.apenergy.2019.113636

Preble, C. V., Harley, R. A., & Kirchstetter, T. W. (2019). Control Technology-Driven Changes to In-Use Heavy-Duty Diesel Truck Emissions of Nitrogenous Species and Related Environmental Impacts. *Environmental Science & Technology, 53*(24), 14568-14576. doi:10.1021/acs.est.9b04763

Presto, A. A., Gordon, T. D., & Robinson, A. L. (2014). Primary to secondary organic aerosol: evolution of organic emissions from mobile combustion sources. *Atmospheric Chemistry and Physics, 14*(10), 5015-5036. doi:10.5194/acp-14-5015-2014

Prokopowicz, A., Zaciera, M., Sobczak, A., Bielaczyc, P., & Woodburn, J. (2015). The effects of neat biodiesel and biodiesel and HVO blends in diesel fuel on exhaust emissions from a light duty vehicle with a diesel engine. *Environmental Science & Technology, 49*(12), 7473-7482. doi:10.1021/acs.est.5b00648

Robinson, A. L., Donahue, N. M., Shrivastava, M. K., Weitkamp, E. A., Sage, A. M., Grieshop, A. P., . . . Pandis, S. N. (2007). Rethinking organic aerosols: semivolatile emissions and photochemical aging. *Science, 315*(5816), 1259-1262. doi:10.1126/science.1133061

Ryoji Nishiumi, A. Y., Yukihiro Tsukasaki, Toshiaki Tanaka. (2004). Effects of Cetane Number and Distillation Characteristics of Paraffinic Diesel Fuels on PM Emission from a DI Diesel Engine. doi:10.4271/2004-01-2960

Sage, A. M., Weitkamp, E. A., Robinson, A. L., & Donahue, N. M. (2008). Evolving mass spectra of the oxidized component of organic aerosol: results from aerosol mass spectrometer analyses of aged diesel emissions. *Atmospheric Chemistry and Physics, 8*(5), 1139-1152. doi:10.5194/acp-8-1139-2008

Samy, S., & Zielinska, B. (2010). Secondary organic aerosol production from modern diesel engine emissions. *Atmospheric Chemistry and Physics, 10*(2), 609-625. doi:10.5194/acp-10-609-2010

Schauer, J. J., Kleeman, M. J., Cass, G. R., & Simoneit, B. R. T. (1999). Measurement of Emissions from Air Pollution Sources. 2. C1 through C30 Organic Compounds from Medium Duty Diesel Trucks. *Environmental Science & Technology, 33*(10), 1578-1587. doi:10.1021/es980081n

Shrivastava, M., Cappa, C. D., Fan, J., Goldstein, A. H., Guenther, A. B., Jimenez, J. L., . . . Zhang, Q. (2017). Recent advances in understanding secondary organic aerosol:

Implications for global climate forcing. *Reviews of Geophysics, 55*(2), 509-559. doi:10.1002/2016rg000540

Simonen, P., Kalliokoski, J., Karjalainen, P., Ronkko, T., Timonen, H., Saarikoski, S., . . . Ntziachristos, L. (2019). Characterization of laboratory and real driving emissions of individual Euro 6 light-duty vehicles - Fresh particles and secondary aerosol formation. *Environmental Pollution, 255*(Pt 1), 113175. doi:10.1016/j.envpol.2019.113175

Singh, D., Subramanian, K. A., & Garg, M. O. (2018). Comprehensive review of combustion, performance and emissions characteristics of a compression ignition engine fueled with hydroprocessed renewable diesel. *Renewable and Sustainable Energy Reviews, 81*, 2947-2954. doi:10.1016/j.rser.2017.06.104

Suarez-Bertoa, R., Kousoulidou, M., Clairotte, M., Giechaskiel, B., Nuottimäki, J., Sarjovaara, T., & Lonza, L. (2019). Impact of HVO blends on modern diesel passenger cars emissions during real world operation. *Fuel, 235*, 1427-1435. doi:10.1016/j.fuel.2018.08.031

Tang, J., Li, Y., Li, X., Jing, S., Huang, C., Zhu, J., . . . Huang, D. (2021). Intermediate volatile organic compounds emissions from vehicles under real world conditions. *Science of The Total Environment, 788*, 147795. doi:10.1016/j.scitotenv.2021.147795

Tuet, W. Y., Chen, Y., Fok, S., Champion, J. A., & Ng, N. L. (2017). Inflammatory responses to secondary organic aerosols (SOA) generated from biogenic and anthropogenic precursors. *Atmospheric Chemistry and Physics, 17*(18), 11423-11440. doi:10.5194/acp-17-11423-2017

Vu, D., Roth, P., Berte, T., Yang, J., Cocker, D., Durbin, T. D., . . . Asa-Awuku, A. (2019). Using a new Mobile Atmospheric Chamber (MACh) to investigate the formation of secondary aerosols from mobile sources: The case of gasoline direct injection vehicles. *Journal of Aerosol Science, 133*, 1-11. doi:10.1016/j.jaerosci.2019.03.009

Wang, M., Li, S., Zhu, R., Zhang, R., Zu, L., Wang, Y., & Bao, X. (2020). On-road tailpipe emission characteristics and ozone formation potentials of VOCs from gasoline, diesel and liquefied petroleum gas fueled vehicles. *Atmospheric Environment, 223*, 117294. doi:10.1016/j.atmosenv.2020.117294

Zhang, Q., Stanier, C. O., Canagaratna, M. R., Jayne, J. T., Worsnop, D. R., Pandis, S. N., & Jimenez, J. L. (2004). Insights into the chemistry of new particle formation and growth events in Pittsburgh based on aerosol mass spectrometry. *Environmental Science & Technology, 38*(18), 4797-4809. doi:10.1021/es035417u

Zhao, Y., Hennigan, C. J., May, A. A., Tkacik, D. S., de Gouw, J. A., Gilman, J. B., . . . Robinson, A. L. (2014). Intermediate-volatility organic compounds: a large source of secondary organic aerosol. *Environmental Science & Technology, 48*(23), 13743-13750. doi:10.1021/es5035188

Zhao, Y., Lambe, A. T., Saleh, R., Saliba, G., & Robinson, A. L. (2018). Secondary Organic Aerosol Production from Gasoline Vehicle Exhaust: Effects of Engine Technology, Cold Start, and Emission Certification Standard. *Environmental Science & Technology, 52*(3), 1253-1261. doi:10.1021/acs.est.7b05045

Zhao, Y., Nguyen, N. T., Presto, A. A., Hennigan, C. J., May, A. A., & Robinson, A. L. (2015). Intermediate Volatility Organic Compound Emissions from On-Road Diesel Vehicles: Chemical Composition, Emission Factors, and Estimated Secondary Organic Aerosol Production. *Environmental Science & Technology, 49*(19), 11516-11526. doi:10.1021/acs.est.5b02841

Zhao, Y., Nguyen, N. T., Presto, A. A., Hennigan, C. J., May, A. A., & Robinson, A. L. (2016). Intermediate Volatility Organic Compound Emissions from On-Road Gasoline Vehicles and Small Off-Road Gasoline Engines. *Environmental Science & Technology, 50*(8), 4554-4563. doi:10.1021/acs.est.5b06247

Supplementary material of chapter 2

The Impact of Hydrogenated Vegetable Oil (HVO) on the Formation of Secondary Organic Aerosol (SOA) from In-Use Heavy-Duty Diesel Vehicles

Sahar Ghadimi[1,2], Hanwei Zhu[1,2], Thomas D. Durbin[1,2], David R. Cocker[1,2], Georgios Karavalakis[1,2]

[1]University of California, Bourns College of Engineering, Center for Environmental Research and Technology (CE-CERT), 1084 Columbia Avenue, Riverside, CA, USA

[2]Department of Chemical and Environmental Engineering, Bourns College of Engineering, University of California, Riverside, CA, USA

Table S 2.1. Fuel properties for CARB ULSD and HVO fuels

Property	Test Method	CARB ULSD	HVO
Viscosity (cSt)	ASTM D4440c	0.83	0.78
Density (g/ml)		0.83	0.78
Nitrogen (ppm)	ASTM D4629	4.9	<1.0
Total Aromatics (mass%)	ASTM D5186	9.9	1.2
Carbon (wt%)	ASTM D5291	86.3	84.96
Hydrogen (wt%)		13.9	15.0
Cetane number	ASTM D613	48.1	79.6

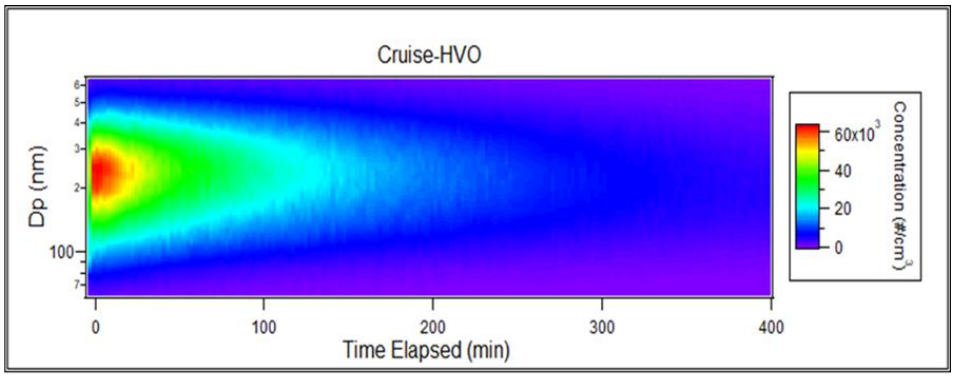

PA: Org 87.2%, 12.8% NH_4NO_3 Dp range(nm): 100-450
SA: Org 80.7%, 19.1% NH_4NO_3 Average Dp: 250nm

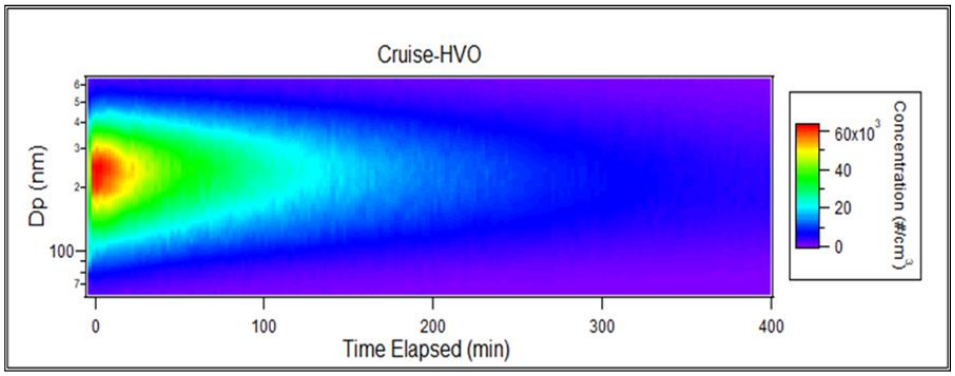

PA: Org 87.2%, 12.8% NH_4NO_3 Dp range(nm): 100-450
SA: Org 80.7%, 19.1% NH_4NO_3 Average Dp: 250nm

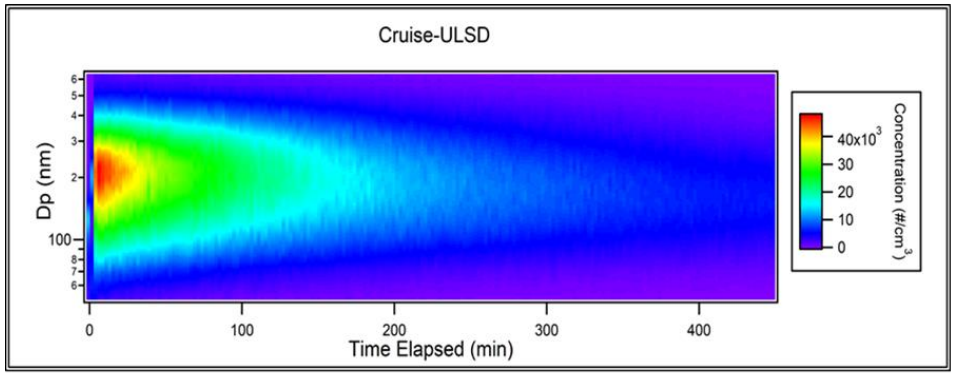

PA: Org 90.7%, 9.3% NH_4NO_3 Dp range(nm): 80-400
SA: Org 91.5%, 8.5% NH_4NO_3 Average Dp: 200nm

Figure S 2.1. Particle size-number concentration distribution and particle's density behavior.

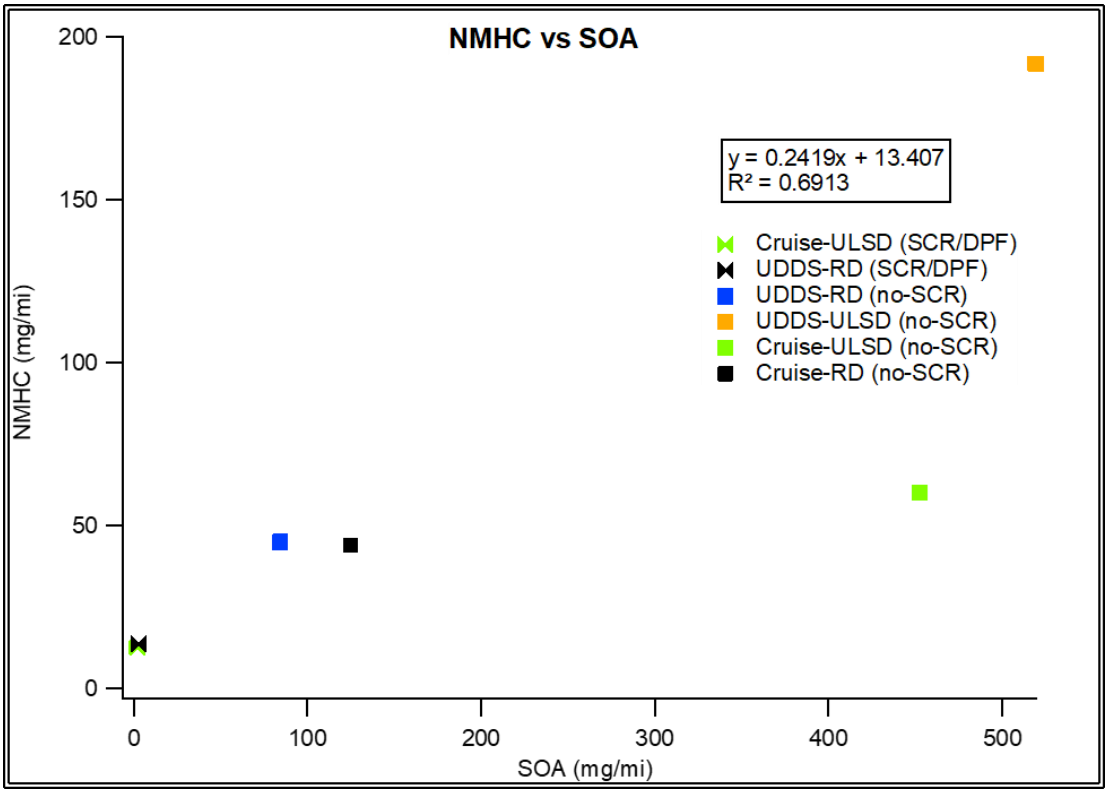

Figure S 2.2. Relationship between tailpipe NMHC emissions and SOA formation for both HDDVs.

Chapter 3 : Exceedances of Secondary Aerosol Formation from In-Use Natural Gas Heavy-Duty Vehicles compared to Diesel Heavy-Duty Vehicles

Sahar Ghadimi [†], *Hanwei Zhu* [†], *Thomas D. Durbin* [†], *David R. Cocker III* [†], *Georgios Karavalakis* [†]

[†]University of California, Bourns College of Engineering, Center for Environmental Research and Technology (CE-CERT), 1084 Columbia Avenue, Riverside, CA, USA

Abstract

This work, for the first time, assessed the primary emissions and secondary aerosol formation from in-use diesel and natural gas heavy-duty vehicles of different vocations. Emissions testing was performed on a chassis dynamometer while the vehicles were exercised on different driving cycles. Secondary aerosol was measured after introducing dilute exhaust into a 30 m^3 environmental chamber. Particulate matter, particle number, and non-methane organic gas (NMOG) emissions were found to be higher for the natural gas vehicles equipped with three-way catalysts (TWCs) compared to the diesel trucks equipped with diesel oxidation catalysts (DOC), diesel particulate filters (DPF), and selective catalytic reduction (SCR) systems. Ammonia formation was favored in the TWC and was found in higher concentrations for the natural gas vehicles than diesel vehicles, leading to substantial secondary ammonium nitrate formation. The advanced aftertreatment controls in diesel vehicles resulted in almost negligible secondary organic aerosol (SOA)

formation, while the natural gas vehicles led to elevated SOA formation that was likely enhanced by the inherent inorganic seed aerosol. For some natural gas vehicles, the contribution of lubricating oil in primary organic aerosol was dominant (as shown in the mass spectra analysis) leading to enhanced SOA mass.

Introduction

On-road heavy-duty (diesel) vehicles are major emission sources of nitrogen oxides (NO_x), particulate matter (PM), and volatile organic compounds (VOCs) that contribute to urban atmospheric pollution (Anenberg et al., 2017; Bishop, Schuchmann, & Stedman, 2013; Wang et al., 2020). Recent advances in engine technology and aftertreatment controls driven by strict policies to tighten emission certification standards have led to a steady reduction of these pollutants (Haugen & Bishop, 2018; Jiang et al., 2018). Further measures to reduce tailpipe emissions from heavy-duty vehicles include the use of biomass-derived low-carbon fuels, such as hydrogenated vegetable oils (HVO), and the widespread use of natural gas vehicles (Gren et al., 2021; Cavan McCaffery et al., 2022; Thiruvengadam et al., 2015; Zhu et al., 2020). HVO is a highly paraffinic diesel-like fuel, free of sulfur and aromatic compounds that has been shown to provide generous reductions in NO_x, PM, and other harmful pollutants (Singh, Subramanian, & Garg, 2018). On the other hand, stoichiometric compressed natural gas (CNG) engines, especially those certified to 0.02 g/bhp-hr of NO_x emissions, have been shown to achieve significant NO_x reductions with additional reductions in PM and VOC emissions (C. McCaffery et al., 2021; Zhu et al., 2020). These advances for on-road heavy-duty vehicles are particularly

important in California, where major regions including the South Coast Air Basin are in non-attainment for PM and ozone.

Mobile sources are also known to contribute to secondary organic aerosol (SOA) formation (Gentner et al., 2017; Ortega et al., 2016), which unlike primary emissions, is not a regulated metric in any part of the world. SOA is a major constituent of ambient aerosol mass and forms in the atmosphere through oxidation reactions of VOC precursors with varying volatilities (Jimenez et al., 2009; Robinson et al., 2007). A number of studies have shown that organic compounds with intermediate volatility (IVOCs) are important precursors of SOA formation (Gordon et al., 2014; Robinson et al., 2007; Zhao et al., 2014). Other studies have discussed the relative contribution of precursor emissions from gasoline vehicles and heavy-duty diesel vehicles on SOA production (Bahreini et al., 2012; Gentner et al., 2012; Platt et al., 2017). Gentner *et al.* reported 2-7 times more SOA for diesel vehicles than gasoline vehicles, while Tang *et al.* showed elevated IVOC emissions from in-use diesel vehicles that contribute to SOA growth (Tang et al., 2021). In contrast, Morino *et al.* showed more SOA for gasoline vehicles versus diesel vehicles when they tested on a chassis dynamometer (Morino et al., 2022). They explained the differences in SOA formation due to the aromatic VOCs in gasoline exhaust and alkane IVOC in diesel exhaust. Recently, Ghadimi *et al.* demonstrated that the use of the biomass-derived HVO fuel will reduce SOA from in-use diesel trucks, whereas trucks with non-functioning aftertreatment systems will lead to more SOA (Ghadimi, Zhu, Durbin, Cocker, & Karavalakis, 2022). Similar findings were observed in a study with in-use vehicles where

newer trucks produced less SOA than older trucks without aftertreatment systems (Zhou et al., 2021).

Although several works have investigated the SOA formation from light-duty gasoline vehicles (Gentner et al., 2017; Roth et al., 2020; Vu et al., 2019) and heavy-duty diesel vehicles and engines (Chirico et al., 2010; Ghadimi et al., 2022; Gordon et al., 2014; Zhou et al., 2021), less is known on the impact of CNG vehicles on precursor emissions and SOA formation. To the best of our knowledge, there is a limited number of studies that employed a different approach than the typical laboratory conditions. These studies used remote sensing devices where measurements for fresh and aged emissions were conducted when vehicles were passing through a sampling station and the vehicle plume was captured for analysis. For example, Watne *et al.* found small differences between fresh and aged emissions for select CNG buses (Watne et al., 2018), whereas other CNG vehicles showed higher secondary mass emissions than diesel vehicles. Le Breton *et al.* utilized the same approach using a potential aerosol mass (PAM) reactor and found an order of magnitude higher aged emissions than fresh emissions from CNG buses (Le Breton et al., 2019). They also suggested that lubricant oil compounds contributed up to 13% of SOA formation in CNG buses when using Gothenburg potential aerosol mass (Go:PAM) reactor. Alanen *et al.* tested a retrofitted natural gas engine under steady-state conditions using a PAM reactor and showed substantially higher SOA formation than primary emissions, but when compared to diesel or gasoline vehicles SOA was at the same levels or lower (Alanen et al., 2017).

This is the first study that measured and compared secondary aerosol formation from in-use diesel and CNG heavy-duty vehicles of different vocations when operated on a chassis dynamometer over multiple driving cycles. Two diesel trucks and six CNG vehicles were exercised over realistic driving cycles. Primary precursor emissions responsible for SOA and secondary inorganic aerosol formation were measured. Secondary aerosol production was assessed in a 30 m^3 environmental chamber. Here, we focus on the fuel, aftertreatment, and engine technology effects on emissions and provide a comparison of the air quality impacts between on-highway diesel and natural gas engines.

Experimental Methods

Test Vehicles and Fuels

A total of eight in-use heavy-duty vehicles were tested in this study. A table describing the technical specifications of the test vehicles is provided in Table S 3.2. Briefly, two diesel goods movement trucks equipped with diesel oxidation catalysts (DOCs), diesel particulate filters (DPFs), and selective catalytic reduction (SCR) were used. For the CNG vehicles, three were transit buses and three were refuse haulers. Three vehicles were fitted with newer Cummins engines certified to meet 0.02 g/bhp-hr of NO_x emissions. All CNG vehicles were equipped with three-way catalysts (TWCs). Both diesel trucks were operated with standard California ultra-low sulfur diesel (ULSD) and one truck was also operated with HVO.

Test Cycles. The diesel trucks were exercised over the Goods Movement cycle that was developed by West Virginia University using Markov chain analysis from the Portable Activity Measurement (PAMS) activity data based on a combination of the drayage trucks

with other goods movement vehicles. The CNG transit buses were tested over the Urban Dynamometer Driving Schedule (UDDS) that simulates the freeway and non-freeway operation of a heavy-duty vehicle. The CNG waste haulers were tested over the UDDS and the SCAQMD (South Coast Air Quality Management District) Refuse Truck Cycle (RTC). The latter cycle consists of two modes, namely the transportation mode and the curbside pick-up mode.

Vehicle Testing and Primary Emissions

All vehicles were tested at CE-CERT's heavy-duty chassis dynamometer facility that consists of a dual 48" roller electric AC design, simulating inertia loads from 10,000 lb. to 80,000 lb. Emission measurements of NO_x, PM, total hydrocarbons (THC), non-methane hydrocarbons (NMHC), and carbon monoxide (CO) were made using CE-CERT's Mobile Emissions Laboratory (Cocker, Shah, Johnson, Miller, & Norbeck, 2004) following procedures set forth in the Code of Federal Regulations (CFR). Ammonia (NH_3) was measured with a Horiba Quantum Cascade Laser (QCL) spectroscopy. Total particle number (TPN) emissions were measured with a TSI 3776 ultrafine-Condensation Particle Counter (CPC) with a cut point of 2.5 nm.

Photooxidation Chamber Experiments

Diluted exhaust from all test vehicles was introduced into a 30 m^3, 2 mil fluorinated ethylene propylene Teflon film Mobile Atmospheric Chamber (MACh). The MACh construction and characterization have been described in detail elsewhere (Vu et al., 2019). Prior to each experiment, the MACh was flushed with clean air for at least 24 hours to ensure the particles and gases level are below detection limits (H_2O < -50°C dew point; NO_x, CO, NMHC, and O_3 at ~0 ppb; and PM= 0 μg m^{-3}). Exhaust emissions were injected

through two Ejector Dilutors (Air-Vac TD11OH) in parallel into the MACh already half-filled with purified air. The chamber was then filled to its maximum volume with purified air. Primary emissions were characterized in the chamber for 30 minutes prior to commencing photooxidation. 1.0 ppm of H_2O_2 was injected as an OH radical source into the chamber. The exhaust was then photooxidized for at least 5 hours or until particle formation and ozone formation subsided, using a UV source consisting of 600 15 W, 18", T8 black light fluorescent bulbs.

A scanning mobility particle sizer (SMPS) consisting of a TSI 3080 electrostatic classifier, TSI 3081 long column differential mobility analyzer (DMA) column, and a TSI 3776 CPC were used to measure the total number, size, and volume of particles. The SMPS data was corrected for particle wall losses to the chamber walls using first-order wall loss kinetics, as described in Cocker *et al.* (Cocker, Flagan, & Seinfeld, 2001). The SMPS data were interpolated using R language to cover more diameter bins for further smoother heatmaps (plotted by Igor). The changes in effective particle density, ρ_{eff}, was monitored throughout the photooxidation process using a Kanomax aerosol particle mass (APM) analyzer coupled to an SMPS (Malloy et al., 2009). The chemical composition of the non-refractory aerosol was measured with an Aerodyne high-resolution time-of-flight aerosol mass spectrometer (HR-ToF-AMS). The unit was operated on both the W and V modes, and data analysis was performed using the ToF-AMS Analysis toolkit 1.57 and AMS HR analysis 1.16.

Results and Discussion:

Primary Emissions and PM Composition

Table S 3.1 shows the THC, CO, NH_3, PM, and the calculated non-methane organic gas (NMOG) primary emissions. For the diesel trucks, THC and CO were measured at very low levels (THC: 0.023-0.035 g/mi; CO: 0.00-0.026 g/mi) indicating that the presence of DOC efficiently controlled emissions at the tailpipe. PM mass emissions ranged from 0.18-0.53 mg/mi. The use of HVO fuel led to lower NMOG emissions (0.032 mg/mi), due to lower NMHC, formaldehyde, and acetaldehyde emissions for this fuel, as well as lower TPN emissions compared with operating on ULSD fuel. For the stoichiometric CNG vehicles, THC and CO emissions (THC: up to 11 g/mi; CO: up to 66 g/mi) were significantly higher than those of the diesel trucks. THC emissions, mainly comprised of CH_4 with a minor NMHC fraction, mainly originated from unburnt fuel. NMOG emissions were higher for the CNG vehicles due to the higher formaldehyde and acetaldehyde emissions compared to diesel vehicles. PM mass emissions were found significantly higher than those of diesel vehicles (CNG: PM 1.4-85 mg/mi; diesel: PM 0.18-0.53 mg/mi). These results are consistent with those reported in previous studies, suggesting that lubricant oil leakage contributes to PM formation in CNG engines, especially in CNG1 and CNG2 experiments (Guido, Napolitano, Alfuso, Corsetti, & Beatrice, 2021; Karavalakis et al., 2016; L. Pirjola et al., 2016; Thiruvengadam et al., 2014). NH_3 is formed in the TWC or SCR systems for stoichiometric CNG and diesel engines, respectively, rather than during the combustion process (Suarez-Bertoa & Astorga, 2016). NH_3 emissions from the CNG vehicles (up to 1.7 g/mi) were considerably higher than those of diesel vehicles (up to 0.40 g/mi), indicating a more dominant formation chemistry in the TWC compared to the SCR

system where ammonia is controlled by the optimization of urea dosing and ammonia storage in the SCR. An exception was seen for CNG2, where NH_3 emissions were almost nonexistent due to the TWC being aged and likely damaged (as indicated by the increased CH_4 emission levels and significantly higher CO and NMOG emissions).

The composition of the tailpipe PM emissions for all test vehicles is shown in **Figure 3.1**. Both diesel vehicles PM emission rates were several orders of magnitude lower than those of the CNG vehicles. PM composition for both vehicles was dominated by organics (HDDV1: ~100%; HDDV2-ULSD: 73%; and HDDV2-HVO: 96.6%), with HDDV2 also showing some ammonium nitrate (NH_4NO_3) attributed to tailpipe NH_3 emissions for this vehicle, which coincidently was an older model year vehicle with more miles than HDDV1 and likely with a more deteriorated catalyst. Similar to diesel trucks, the mass fraction in primary for all CNG vehicles was largely organic, ranging from 63% to 99% of total PM. CNG1 (47 mg/mi) and CNG2 (85 mg/mi) showed dramatically higher PM emissions than the other CNG vehicles, with the older technology and higher mileage CNG2 having almost double the primary PM than CNG1. The results for all CNG vehicles, and especially for CNG1 and CNG2, indicate a nonfuel source of PM, since natural gas (consisting primarily of CH_4) does not have C-C bonds making it difficult to form benzene rings and thus soot. The primary emissions in CNG1-UDDS (PA: 47 mg/mi) and CNG2-UDDS (PA: 85 mg/mi) were substantially higher than the other CNG vehicles and diesel trucks due to more lubricant oil passage through the combustion chamber.

Previous studies have reported the contribution of lubricant oil to primary organic aerosol (POA) emitted from diesel and gasoline vehicles (Carbone et al., 2019; Worton et

al., 2014). For example, Sonntag *et al.* showed that the contribution of lubricant oil to PM was over 25% across a fleet of 99 vehicles. As mentioned earlier, the main source of POA in CNG vehicles is due to the lubricant oil passage into the combustion chamber. Thiruvengadam *et al.* showed that the elemental species detected in PM emissions from CNG transit buses were similar to the elemental composition of the lubricating oil used in these vehicles (Thiruvengadam et al., 2014).

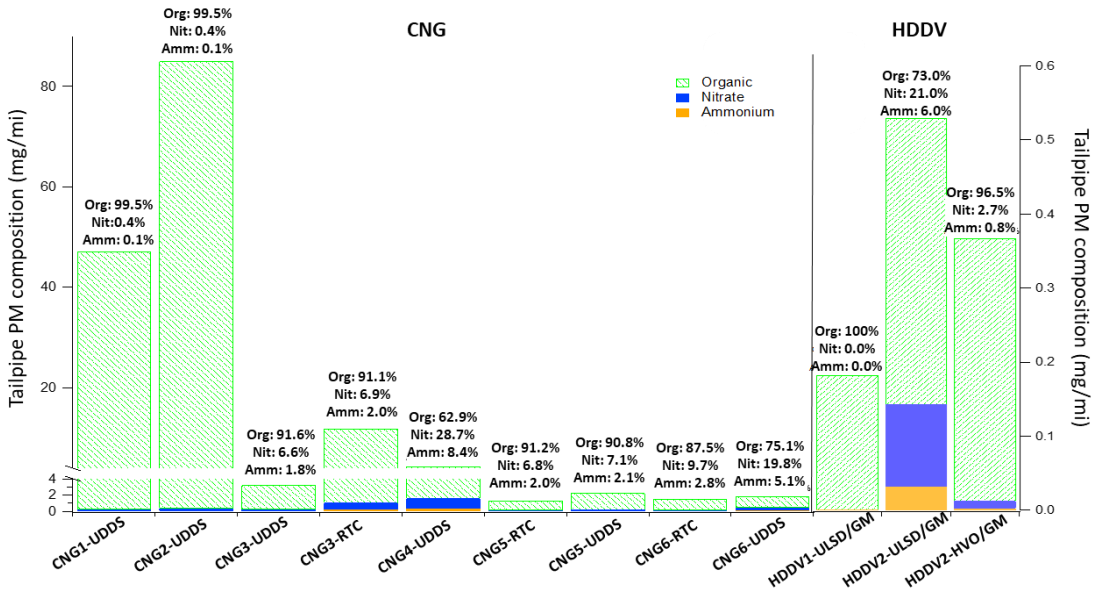

Figure 3.1. Chemical characterization of primary aerosols: Tailpipe emissions composition (Org = Organic, Nit = Nitrate, Amm = Ammonium).

Secondary Aerosol Composition

Figure 3.2 shows the composition of total secondary aerosol mass after 5 hours of photooxidation in the chamber. Consistent with previous works, total secondary aerosol mass significantly exceeded primary PM (Ghadimi et al., 2022; Vu et al., 2019), with the exception of HDDV1 where no appreciable growth was observed. For HDDV2, secondary aerosol mass was 172 and 144 times higher for ULSD and HVO, respectively, than primary

PM. The difference between the two diesel vehicles was the formation of ammonium nitrate (89 mg/mi for USLD and 51.5 mg/mi for HVO) compared to the negligible ammonium nitrate formation for HDDV1 which was consistent with the zero tailpipe NH_3 and lower NO_x emissions from this vehicle compared to HDDV2 (Table S 3.1).

Ammonium nitrate formation dominated the total secondary aerosol mass for CNG vehicles, ranging from 23.1% to 96.5% of total secondary particulate. CNG2 was an exception, where the inorganic mass portion was lower in total secondary aerosol due to the lower NH_3 emissions. Tailpipe NH_3 was the major driver of secondary ammonium nitrate production in the chamber. Natural gas vehicles equipped with spark ignition engines and TWCs produce NH_3 inside the catalyst during the reduction reactions of NO through a mechanism that involves hydrogen production via the water-gas shift reaction between CO and water (Nevalainen et al., 2018). The negligible NH_3 emissions and therefore lower secondary ammonium formation for CNG2 were due to a damaged TWC. The results reported here suggest that CNG goods movement trucks and refuse haulers are important sources of urban inorganic aerosols.

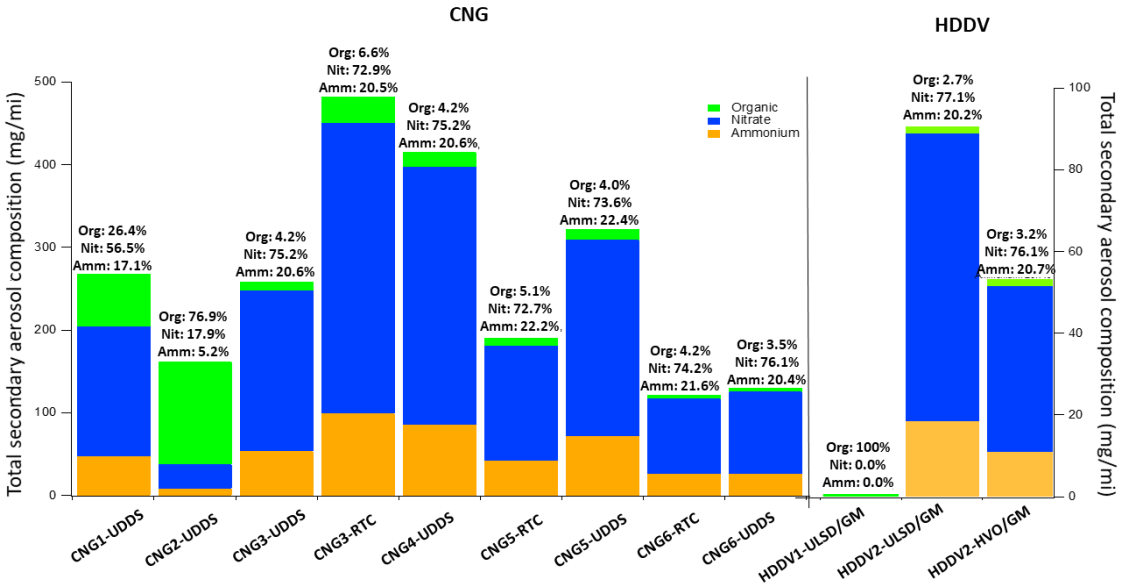

Figure 3.2. Chemical characterization of secondary aerosols: Aerosol composition after 5 hours irradiation. The green portion illustrates total organic mass after 5 hours of photooxidation (OA(5h)). The blue and orange portions are illustrating the total inorganic mass after 5 hours of photooxidation.

Carbonaceous Aerosol Composition

Figure 3.3 shows the relative primary and secondary production of carbonaceous aerosol for diesel trucks and CNG vehicles after 5 hours of photooxidation. For HDDV2, the use of HVO resulted in lower SOA mass production compared to ULSD. Similar results were recently reported by Ghadimi *et al.* and were attributed to the absence of aromatic hydrocarbons in HVO. HDDV2 produced substantially more SOA compared to HDDV1, despite the very similar levels of tailpipe NMOG emissions from both trucks (Ghadimi et al., 2022). It is theorized that the higher SOA formation for HDDV2 was likely due to the presence of ammonium nitrate in the chamber, which acted as a seed aerosol for SOA formation (Huang et al., 2016; Lu, Hao, Takekawa, Hu, & Li, 2009). Lu *et al.* have shown that SOA generation and yields positively correlate with the inorganic seed surface concentrations. Kroll *et al.* found the SOA yields were significantly lower when inorganic

seed particles were not present and described that the seed effect could go beyond the surface effect so that in the presence of seed particles the absorbed products undergo additional reaction processes, leading to enhancements in lower-volatility compounds.

All CNG vehicles showed substantial SOA formation (7.78-39.7 mg/mi). The highest SOA formation was seen for CNG2 (39.7 mg/mi), consistent with the highest NMOG emissions for this vehicle as well as significant lubricant oil leakage. Similarly, this significant lubricant oil leakage led to enhanced SOA formation in CNG1. Despite the highest absolute SOA mass for CNG2, the SOA did not exceed the POA, which can be likely explained by the higher lubricant oil in primary emission, as well as the cracked TWC both causing POA formation. With the exception of CNG1 and CNG2 with significant primary lubricant oil leakage, all the other CNG vehicles showed higher SOA than POA. Interestingly, for CNG3, CNG4, CNG5, and CNG6 vehicles, the SOA mass formation was directly proportional (R^2=0.98) to their ammonium nitrate formation **Figure S 3.2**, supporting the theory that ammonium nitrate aerosols promoted the secondary organic gas-phase condensation and enhanced SOA formation (Kroll, Chan, Ng, Flagan, & Seinfeld, 2007).

Since many parameters affect the SOA formation, we performed a multivariant linear regression model (using R language) on all CNG experiments (including CNG1 and CNG2) to evaluate the effect of tailpipe emissions (such as NMOG and POA) and secondary inorganic (NH_4NO_3) mass on the formation of SOA mass. It was observed that the SOA formation exhibited strong correlations with the above-mentioned variables (R^2

= 99.2%, *p*-value= 0.00018, see **(Equation 3.1**), illustrating the effect of NH_4NO_3 seeds on SOA formations. **(see Figure S 3.5)**.

SOA (mg/mi) = -2.54 + 1.57×NMOG (mg/mi) + 0.11×THC (g/mi) + 0.44×POA (mg/mi) + 0.04×NH_4NO_3 (mg/mi) **(Equation 3.1)**

CNG2 was an interesting case because this vehicle had an aged and likely structurally damaged TWC, which resulted in higher primary (i.e., PM, NMOG) and secondary organic emissions due to the deteriorated catalytic activity. Aging effects in the TWC can cause sintering of the precious metals and the wash coat, as well as catalyst deactivation through poisoning of active centers or suppression of oxygen storage capacity due to metals and elements, originated from the lubricant oil. Ghadimi *et al.* showed that a damaged or tampered DPF can cause disproportionately higher primary emissions and SOA formation compared to properly functioned aftertreatment systems. Similarly, the current work demonstrated that non-functioning aftertreatment systems for in-use natural gas vehicles can also produce more primary emissions and SOA formation.

When comparing earlier studies, it should be noted that the current dataset was unique as it was derived from chassis dynamometer testing over realistic transient driving cycles. SOA formed from CNG vehicles tested in this work ranged from 0.012 to 0.100 g kg-fuel^{-1}. Alanen *et al.* found lower SOA formation (0.0090 to 0.020 g kg-fuel^{-1}) when they tested a light-duty 2.0 L natural gas engine equipped with non-commercial aftertreatment systems over steady-state engine conditions (Alanen et al., 2017). In contrast, Watne *et al.* reported higher secondary mass formed from CNG buses (i.e., 0.12-7.7 g kg-fuel^{-1}) relative to this study using an oxidation flow reactor and capturing the vehicle plume during full

throttle acceleration from standstill (Watne et al., 2018). Interestingly, our results were also comparable to those of Roth *et al.*, who tested light-duty spark ignition gasoline direct injection engines equipped with TWCs operated with low-carbon ethanol blends (0.0095-0.021 g kg-fuel^{-1}) (Roth et al., 2020). The diesel vehicles tested here produced insignificant SOA mass (less than 2.0 mg/mi) and certainly lower than those equipped with non-functioning aftertreatment controls (Ghadimi *et al.*), as well as older vehicles lacking robust aftertreatment systems and operating over idling or steady-state conditions (Chirico et al., 2010; Deng et al., 2020).

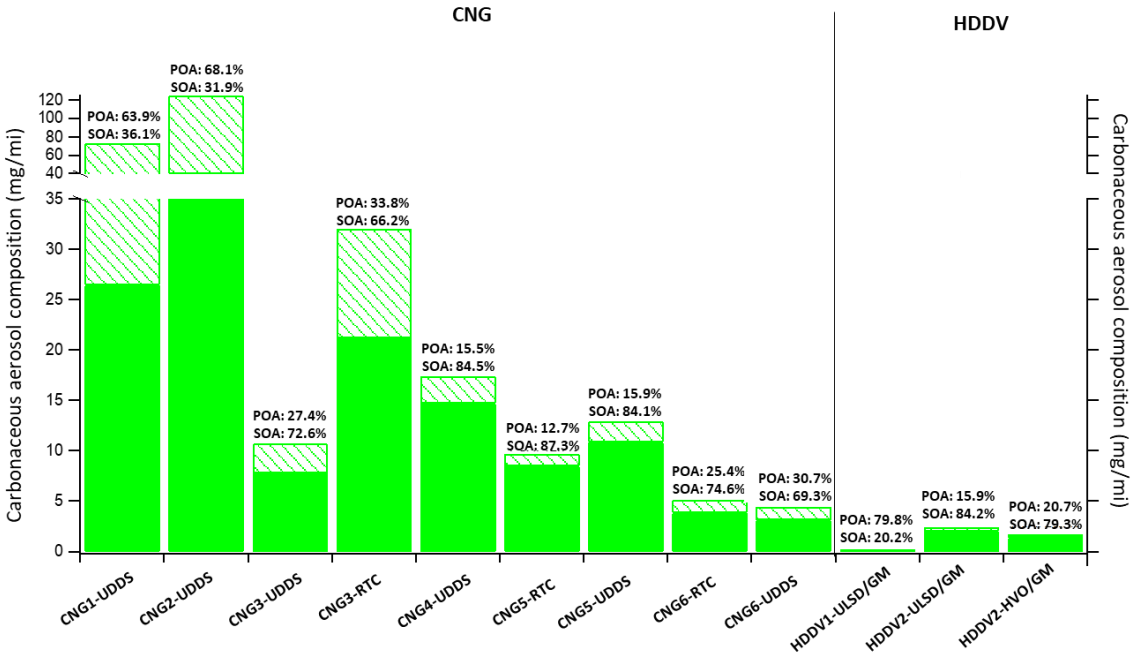

Figure 3.3. Carbonaceous Aerosol Composition of aerosols: Aerosol Composition after 5-hour Irradiation. (SOA was calculated from the subtraction of the total primary organic at time zero from the total organic mass after 5 hours irradiation).

Figure S 3.3 shows a Van Krevelen (VK) diagram illustrating the O:C vs. H:C atomic ratios of POA and SOA for the test vehicles. All the corresponding O:C and H:C values reported for SOA were calculated by subtracting the chemical compositions of

OA(5h) from POA using mass balance. For the diesel trucks, primary emissions contained organic particles with O:C ratio ranging from 0.14-0.18 and H:C ratio ranging from 2.13-2.23. After 5 hours of photooxidation, the range of O:C ratio increased to 0.26-0.70 and the range of H:C ratio decreased to 1.68-2.16. The primary aerosol for the experiment with ULSD was slightly more oxidized after 5 hours of photooxidation when compared to the aromatics-free HVO fuel. For the CNG trucks, the O:C and H:C ratios in POA ranged from 0.07-0.45 and from 1.86-2.11, respectively. These O:C values are slightly higher than those reported by Pirjola *et al.* for CNG buses (0.02-0.12) (Liisa Pirjola et al., 2019). The O:C and H:C ratios in SOA ranged from 0.36-1.33 and from 1.52-2.1, respectively, for all CNG trucks. For CNG1 (CNG2) over the UDDS, the O:C vs. H:C values in POA were 0.07 (0.11) vs. 2.04 (2.01). As the average chemical formula of POA composition in CNG1 ($C_nH_{2.04n}O_{0.07n}$; typical long chain fatty acid formula in lubricant oil) and CNG2 ($C_nH_{2.01n}O_{0.11n}$) experiments indicate, the chemical composition of POA for these vehicles is consistent with that of long chain hydrocarbons typically present in lubricant oil. After 5 hours of photooxidation for the CNG1 (CNG2) experiment, the O:C vs. H:C ratios changed to 0.72 (0.36) vs. 2.1 (1.90). As evident from the VK diagram, the O:C ratios of SOA after 5 hours of photooxidation for both CNG1 and CNG2 increased by 4-10 times compared to the primary O:C ratios, but still lower compared to the O:C ratios of SOA in other CNG vehicles. Lower O:C ratios of SOA in CNG1-2 compared to other CNG vehicles can be explained by the oxidation of lubricant oil precursors (long chain hydrocarbons) in CNG1 and CNG2. Overall, the higher O:C ratios of SOA for CNG3-CNG6 vehicles (with lower lubricant oil leakage) compared to the diesel trucks and CNG1-

CNG2 were likely due to the smaller hydrocarbon species with non-lubricant oil origin for CNG3- CNG6 combustion precursors, indicating that the addition of one oxygen to a smaller molecule can result in higher O:C values.

Aerosol Size Distributions

Figure 3.4 shows the particle size distribution and particle effective density as a function of photooxidation time in the chamber for HDDV1 (**Figure 3.4 A-B**) and CNG3 (C-D), respectively. For HDDV1, particle size distribution was largely unimodal, ranging between 50 nm to 200 nm in diameter with an effective density of 0.7 g cm^{-3}, which was consistent with organic aerosols (see HDDV1-ULSD/GM in **Figure 3.1** and **Figure 3.2**). After 5 hours of photooxidation the density increased to 0.9 g cm^{-3}, suggesting that condensing secondary organic products (about 20% SOA formation) onto the existing particles resulting in increased aerosol mass. At the onset of the photooxidation, the particle size range was broader (50 nm to 200 nm) and became narrower (70 nm to 90 nm) after 5 hours of irradiation.

For CNG3, the diameter of primary particles was smaller (<50 nm) than those of the HDDV1, with an initial density of 1.14 g cm^{-3}. The aerosol composition before the UV lights were turned on was primarily organics (~91%) with some ammonium nitrate (~8.4%), which explains the higher initial density. During the photooxidation process, particle diameters peaked at ~250 nm, with the composition of particles shifting more to ammonium nitrate (~80%). The density at the end of the photooxidation increased to ~1.5 g cm^{-3}, consistent with condensation of ammonium nitrate (density of 1.72 g cm^{-3}) onto the particulate. Information about the particle size distributions and effective density for the

other CNG trucks is provided in **Figure S 2.1**. Primary particles for CNG1 and CNG2 had larger sizes (50 nm to 170 nm) than the other CNG trucks, which can be attributed to the greater contribution of lubricant oil to the emissions of these vehicles. For CNG1 and CNG2, the average size of particles grew from 90 nm (primary aerosol of 47.1 mg/mi) to ~200 nm (secondary aerosol of 277.7 mg/mi) and from 90 nm (primary aerosol of 84.9 mg/mi) to ~110 nm (secondary aerosol of 161.7 mg/mi), respectively, after 400 minutes of photooxidation. The higher secondary inorganic composition for CNG1 (73.6%) compared to CNG2 (23.1%) was reflected in the higher density (CNG1: 1.5 g cm^{-3}, CNG2: 1.1 g cm^{-3}) as well as higher particle diameter for this vehicle. For CNG3-6, two distinct particle peaks were seen during the photooxidation process, suggesting the formation of new secondary inorganic particles in addition to the growth of existing primary particles (mainly organics).

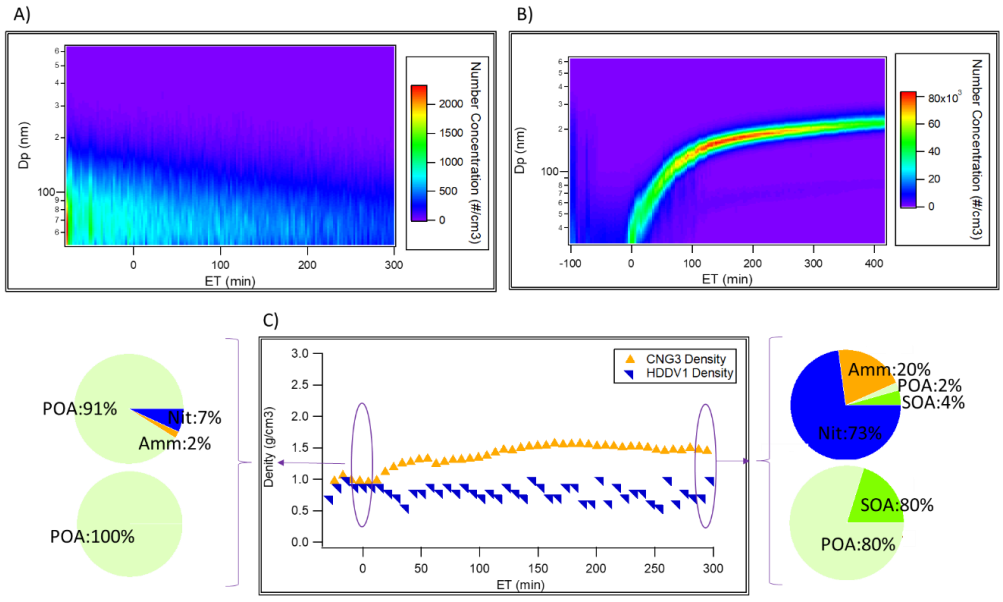

Figure 3.4. Particle size-number concentration distribution and particle density behavior: A) Goods movement-ULSD (HDDV1); B) Refuse-0.2g CNG (CNG3); C) The effective density for CNG1 and HDDV1 throughout the experiment.

High-Resolution Mass Spectra Analysis of POA and SOA in CNG Vehicles

The influence of lubricant oil on POA and OA(5h) of CNG vehicles was shown in **Figure 3.5 A-D. Figure 3.5A-B** shows the mass spectra from CNG1 truck that lightly combusted lubricant oil leakage (lightly oxidized) and **Figure 3.5 C-D** shows the mass spectra from CNG4 truck with heavily combusted lubricant oil (heavily oxidized) both running over the UDDS driving cycle. It is important to note that, due to the nature of natural gas (mostly comprised of CH_4) higher m/z are indication of a non-fuel source. The mass spectra showed the ion fragments of linear and branched alkyl ions ($C_nH_{2n+1}^+$: m/z 57, 71, 85, 99, …), alkeny and cycloalkyl ions ($C_nH_{2n-1}^+$: m/z 55, 69, 83, 97, 111, …), cycloalkenyl ions $C_nH_{2n-3}^+$ (m/z 67, 81, 95, 109, ...), and phenyl alkyls ions ($C_6H_5C_nH_{2n}^+$: m/z 77, 91, 105, 119, …) that formed during the harsh ionization process in the HR-ToF-AMS (Tobias et al., 2001). The results reported here are consistent with previous studies that reported the important contribution of lubricant oil on SOA formation from natural gas vehicles (Le Breton et al., 2019; Tobias et al., 2001; Watne et al., 2018). For CNG1, there was a greater abundance of the ion fragment mass spectra with m/z 83 (cyclohexyl) than with m/z 85 (the non-cyclic ion fragment of n-hexyl and its branched derivatives), indicating that the primary particles were enriched with cycloalkanes that are typically linked in emissions from unburnt lubricant oil. Similar observations were made in an earlier study that showed greater amounts of cycloalkanes compared to n-alkanes and branched alkanes in aerosol composition for the lubricant oil (Tobias et al., 2001). The footprint of combusted lubricant oil was observed in the spectra of CNG4, as evident in their higher

CHO class in both primary and secondary mass spectra of CNG 4 compared to CNG1 with unburnt lubricant oil. The m/z 57 mostly consist of $C_4H_9^+$, $C_3H_5O^+$ ion fragments. In POA of CNG1, the m/z 57 peak comprised of 97.6% $C_4H_9^+$ and only 1.2% $C_3H_5O^+$, while in CNG4 $C_4H_9^+$ was 83.5%, and $C_3H_5O^+$ was 13.6% of m/z 57 peak, showing higher oxidation state of primary emissions in CNG4 compared to CNG1. Moreover, after 5 hours of photooxidation, the percentage of $C_4H_9^+$and $C_3H_5O^+$ in m/z 57 of CNG1 were 93.5% and 5.3%, respectively, while the percentage of $C_4H_9^+$and $C_3H_5O^+$ in m/z 57 of CNG4 were 69.6% and 23.5%, respectively showing higher oxidation state of secondary emissions in CNG4 compared to CNG1.

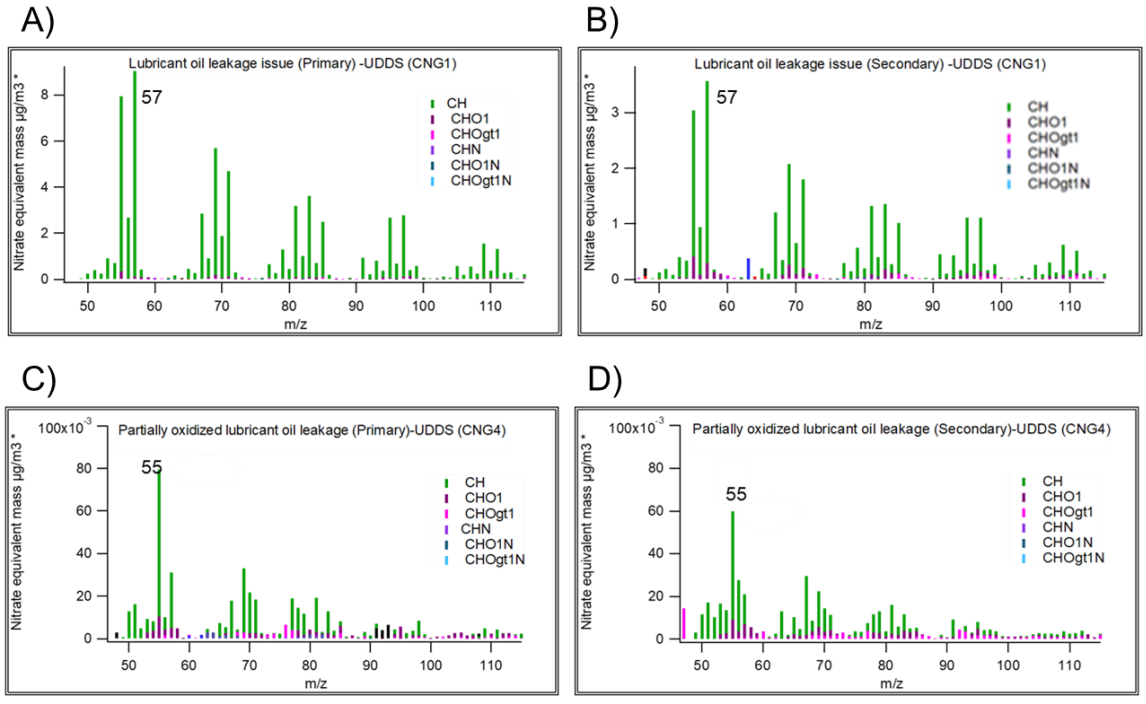

Figure 3.5. Average HR mass spectra of POA and OA(5h) in CNG with unburnt and combusted lubricant oil leakage. A) POA of CNG1 with unburnt lubricant oil leakage; B) OA(5h) of CNG1 with unburnt lubricant oil leakage; C) POA of CNG4 with combusted lubricant oil; D) OA(5h) of CNG4 with combusted lubricant oil.

Implications

With the rapid pace of electric vehicle adoption in the light-duty sector, heavy-duty vehicles of different vocations will largely be the major emissions from the on-road transport sector. Heavy-duty vehicle electrification is more difficult to be achieved in large scale because these vehicles are highly sensitive to operating costs, driving range, and battery life. While some vocational types such as transit buses and refuse haulers have shown a better potential for electrification due to their consistent trip schedules, other vocations such as goods movement and delivery vehicles will operate with internal combustion engines for the foreseeable future. Advancements in engine technology and aftertreatment controls, and the widespread use of low- or zero-carbon fuels will be necessary for the further reduction of tailpipe emissions and secondary aerosols. Our work showed that current diesel vehicles with well-functioning robust aftertreatment controls will not only provide significant tailpipe emission benefits but will also be an almost negligible source of SOA formation from the transportation sector. The use of aromatics-free renewable diesel is expected to further lower SOA mass. Vehicles equipped with spark ignition engines and operated with natural gas are likely sources of SOA production and will likely be contributors to inorganic aerosol in the atmosphere. This work did not show a clear relationship for the natural gas vehicles between engine technology (as indicated by the engine certification for engines certified to 0.2 g/bhp-hr NO_x emissions vs. 0.02 g/bhp-hr ultra-low NO_x emissions) or vehicle mileage. In contrast, our work showed a nonfuel source of SOA formation from some natural gas vehicles. Better control of lubricant oil consumption and new lubricant oil formulations in natural gas engines will result in lower

POA emissions and reduced SOA formation. Our work suggests the need for catalyzed gasoline particulate filters in natural gas engines for the reduction of particles related to lubricant oil and SOA precursor emissions. More efficient control of ammonia emissions (ammonia slip) from SCR-equipped and TWC-equipped vehicles via advanced oxidation catalysts will also result in the reduction of secondary ammonium nitrate aerosol that will in turn lead to lower SOA yields.

References:

Alanen, J., Simonen, P., Saarikoski, S., Timonen, H., Kangasniemi, O., Saukko, E., . . . Rönkkö, T. (2017). Comparison of primary and secondary particle formation from natural gas engine exhaust and of their volatility characteristics. *Atmospheric Chemistry and Physics*, *17*(14), 8739-8755. doi:10.5194/acp-17-8739-2017

Anenberg, S. C., Miller, J., Minjares, R., Du, L., Henze, D. K., Lacey, F., . . . Heyes, C. (2017). Impacts and mitigation of excess diesel-related NO(x) emissions in 11 major vehicle markets. *Nature*, *545*(7655), 467-471. doi:10.1038/nature22086

Bahreini, R., Middlebrook, A. M., de Gouw, J. A., Warneke, C., Trainer, M., Brock, C. A., . . . Parrish, D. D. (2012). Gasoline emissions dominate over diesel in formation of secondary organic aerosol mass. *Geophysical Research Letters*, *39*(6), L06805. doi:10.1029/2011gl050718

Bishop, G. A., Schuchmann, B. G., & Stedman, D. H. (2013). Heavy-duty truck emissions in the South Coast Air Basin of California. *Environmental Science & Technology*, *47*(16), 9523-9529. doi:10.1021/es401487b

Carbone, S., Timonen, H. J., Rostedt, A., Happonen, M., Rönkkö, T., Keskinen, J., . . . Saarikoski, S. (2019). Distinguishing fuel and lubricating oil combustion products in diesel engine exhaust particles. *Aerosol Science and Technology*, *53*(5), 594-607. doi:10.1080/02786826.2019.1584389

Chirico, R., DeCarlo, P. F., Heringa, M. F., Tritscher, T., Richter, R., Prévôt, A. S. H., . . . Baltensperger, U. (2010). Impact of aftertreatment devices on primary emissions and secondary organic aerosol formation potential from in-use diesel vehicles: results from smog chamber experiments. *Atmospheric Chemistry and Physics*, *10*(23), 11545-11563. doi:10.5194/acp-10-11545-2010

Cocker, D. R., 3rd, Flagan, R. C., & Seinfeld, J. H. (2001). State-of-the-art chamber facility for studying atmospheric aerosol chemistry. *Environmental Science & Technology*, *35*(12), 2594-2601. doi:10.1021/es0019169

Cocker, D. R., 3rd, Shah, S. D., Johnson, K., Miller, J. W., & Norbeck, J. M. (2004). Development and application of a mobile laboratory for measuring emissions from diesel engines. 1. Regulated gaseous emissions. *Environmental Science & Technology*, *38*(7), 2182-2189. doi:10.1021/es034888d

Deng, W., Fang, Z., Wang, Z., Zhu, M., Zhang, Y., Tang, M., . . . Wang, X. (2020). Primary emissions and secondary organic aerosol formation from in-use diesel vehicle exhaust: Comparison between idling and cruise mode. *Science of The Total Environment*, *699*, 134357. doi:10.1016/j.scitotenv.2019.134357

Gentner, D. R., Isaacman, G., Worton, D. R., Chan, A. W., Dallmann, T. R., Davis, L., . . . Goldstein, A. H. (2012). Elucidating secondary organic aerosol from diesel and gasoline vehicles through detailed characterization of organic carbon emissions. *Proceedings of the National Academy of Sciences 109*(45), 18318-18323. doi:10.1073/pnas.1212272109

Gentner, D. R., Jathar, S. H., Gordon, T. D., Bahreini, R., Day, D. A., El Haddad, I., . . . Robinson, A. L. (2017). Review of Urban Secondary Organic Aerosol Formation from Gasoline and Diesel Motor Vehicle Emissions. *Environmental Science & Technology, 51*(3), 1074-1093. doi:10.1021/acs.est.6b04509

Ghadimi, S., Zhu, H., Durbin, T. D., Cocker, D. R., & Karavalakis, G. (2022). The impact of hydrogenated vegetable oil (HVO) on the formation of secondary organic aerosol (SOA) from in-use heavy-duty diesel vehicles. *Science of The Total Environment, 822*, 153583. doi:10.1016/j.scitotenv.2022.153583

Gordon, T. D., Presto, A. A., Nguyen, N. T., Robertson, W. H., Na, K., Sahay, K. N., . . . Robinson, A. L. (2014). Secondary organic aerosol production from diesel vehicle exhaust: impact of aftertreatment, fuel chemistry and driving cycle. *Atmospheric Chemistry and Physics, 14*(9), 4643-4659. doi:10.5194/acp-14-4643-2014

Gren, L., Malmborg, V. B., Falk, J., Markula, L., Novakovic, M., Shamun, S., . . . Pagels, J. (2021). Effects of renewable fuel and exhaust aftertreatment on primary and secondary emissions from a modern heavy-duty diesel engine. *Journal of Aerosol Science, 156*, 105781. doi:10.1016/j.jaerosci.2021.105781

Guido, C., Napolitano, P., Alfuso, S., Corsetti, C., & Beatrice, C. (2021). How engine design improvement impacts on particle emissions from an HD SI natural gas engine. *Energy, 231*, 120748. doi:10.1016/j.energy.2021.120748

Haugen, M. J., & Bishop, G. A. (2018). Long-Term Fuel-Specific NO (x) and Particle Emission Trends for In-Use Heavy-Duty Vehicles in California. *Environmental Science & Technology, 52*(10), 6070-6076. doi:10.1021/acs.est.8b00621

Huang, D. D., Zhang, X., Dalleska, N. F., Lignell, H., Coggon, M. M., Chan, C.-M., . . . Chan, C. K. (2016). A note on the effects of inorganic seed aerosol on the oxidation state of secondary organic aerosol-α-Pinene ozonolysis. *Journal of Geophysical Research: Atmospheres, 121*(20), 12,476-412,483. doi:10.1002/2016jd025999

Jiang, Y., Yang, J., Cocker, D., 3rd, Karavalakis, G., Johnson, K. C., & Durbin, T. D. (2018). Characterizing emission rates of regulated pollutants from model year 2012+ heavy-duty diesel vehicles equipped with DPF and SCR systems. *Science of The Total Environment, 619-620*, 765-771. doi:10.1016/j.scitotenv.2017.11.120

Jimenez, J. L., Canagaratna, M. R., Donahue, N. M., Prevot, A. S., Zhang, Q., Kroll, J. H., . . . Worsnop, D. R. (2009). Evolution of organic aerosols in the atmosphere. *Science, 326*(5959), 1525-1529. doi:10.1126/science.1180353

Karavalakis, G., Hajbabaei, M., Jiang, Y., Yang, J., Johnson, K. C., Cocker, D. R., & Durbin, T. D. (2016). Regulated, greenhouse gas, and particulate emissions from lean-burn and stoichiometric natural gas heavy-duty vehicles on different fuel compositions. *Fuel, 175*, 146-156. doi:10.1016/j.fuel.2016.02.034

Kroll, J. H., Chan, A. W., Ng, N. L., Flagan, R. C., & Seinfeld, J. H. (2007). Reactions of semivolatile organics and their effects on secondary organic aerosol formation. *Environmental Science & Technology, 41*(10), 3545-3550. doi:10.1021/es062059x

Le Breton, M., Psichoudaki, M., Hallquist, M., Watne, Å. K., Lutz, A., & Hallquist, Å. M. (2019). Application of a FIGAERO ToF CIMS for on-line characterization of real-world fresh and aged particle emissions from buses. *Aerosol Science and Technology, 53*(3), 244-259. doi:10.1080/02786826.2019.1566592

Lu, Z., Hao, J., Takekawa, H., Hu, L., & Li, J. (2009). Effect of high concentrations of inorganic seed aerosols on secondary organic aerosol formation in the m-xylene/NOx photooxidation system. *Atmospheric Environment, 43*(4), 897-904. doi:10.1016/j.atmosenv.2008.10.047

Malloy, Q. G. J., Nakao, S., Qi, L., Austin, R., Stothers, C., Hagino, H., & Cocker, D. R. (2009). Real-Time Aerosol Density Determination Utilizing a Modified Scanning Mobility Particle Sizer—Aerosol Particle Mass Analyzer System. *Aerosol Science and Technology, 43*(7), 673-678. doi:10.1080/02786820902832960

McCaffery, C., Zhu, H., Sabbir Ahmed, C. M., Canchola, A., Chen, J. Y., Li, C., . . . Karavalakis, G. (2022). Effects of hydrogenated vegetable oil (HVO) and HVO/biodiesel blends on the physicochemical and toxicological properties of emissions from an off-road heavy-duty diesel engine. *Fuel, 323*, 124283. doi:10.1016/j.fuel.2022.124283

McCaffery, C., Zhu, H., Tang, T., Li, C., Karavalakis, G., Cao, S., . . . Durbin, T. D. (2021). Real-world NOx emissions from heavy-duty diesel, natural gas, and diesel hybrid electric vehicles of different vocations on California roadways. *Science of The Total Environment, 784*, 147224. doi:10.1016/j.scitotenv.2021.147224

Morino, Y., Li, Y., Fujitani, Y., Sato, K., Inomata, S., Tanabe, K., . . . Kobayashi, S. (2022). Secondary organic aerosol formation from gasoline and diesel vehicle exhaust under light and dark conditions. *Environmental Science: Atmospheres, 2*(1), 46-64. doi:10.1039/d1ea00045d

Nevalainen, P., Kinnunen, N. M., Kirveslahti, A., Kallinen, K., Maunula, T., Keenan, M., & Suvanto, M. (2018). Formation of NH 3 and N 2 O in a modern natural gas three-way catalyst designed for heavy-duty vehicles: the effects of simulated exhaust gas composition and ageing. *Applied Catalysis A: General, 552*, 30-37. doi:10.1016/j.apcata.2017.12.017

Ortega, A. M., Hayes, P. L., Peng, Z., Palm, B. B., Hu, W., Day, D. A., . . . Jimenez, J. L. (2016). Real-time measurements of secondary organic aerosol formation and aging from ambient air in an oxidation flow reactor in the Los Angeles area. *Atmospheric Chemistry and Physics, 16*(11), 7411-7433. doi:10.5194/acp-16-7411-2016

Pirjola, L., Dittrich, A., Niemi, J. V., Saarikoski, S., Timonen, H., Kuuluvainen, H., . . . Hillamo, R. (2016). Physical and Chemical Characterization of Real-World Particle Number and Mass Emissions from City Buses in Finland. *Environmental Science & Technology, 50*(1), 294-304. doi:10.1021/acs.est.5b04105

Pirjola, L., Kuuluvainen, H., Timonen, H., Saarikoski, S., Teinilä, K., Salo, L., . . . Rönkkö, T. (2019). Potential of renewable fuel to reduce diesel exhaust particle emissions. *Applied Energy, 254*, 113636. doi:10.1016/j.apenergy.2019.113636

Platt, S. M., El Haddad, I., Pieber, S. M., Zardini, A. A., Suarez-Bertoa, R., Clairotte, M., . . . Prevot, A. S. H. (2017). Gasoline cars produce more carbonaceous particulate matter than modern filter-equipped diesel cars. *Sci Rep, 7*(1), 4926. doi:10.1038/s41598-017-03714-9

Robinson, A. L., Donahue, N. M., Shrivastava, M. K., Weitkamp, E. A., Sage, A. M., Grieshop, A. P., . . . Pandis, S. N. (2007). Rethinking organic aerosols: semivolatile emissions and photochemical aging. *Science, 315*(5816), 1259-1262. doi:10.1126/science.1133061

Roth, P., Yang, J., Peng, W., Cocker, D. R., Durbin, T. D., Asa-Awuku, A., & Karavalakis, G. (2020). Intermediate and high ethanol blends reduce secondary organic aerosol formation from gasoline direct injection vehicles. *Atmospheric Environment, 220*, 117064. doi:10.1016/j.atmosenv.2019.117064

Singh, D., Subramanian, K. A., & Garg, M. O. (2018). Comprehensive review of combustion, performance and emissions characteristics of a compression ignition engine fueled with hydroprocessed renewable diesel. *Renewable and Sustainable Energy Reviews, 81*, 2947-2954. doi:10.1016/j.rser.2017.06.104

Suarez-Bertoa, R., & Astorga, C. (2016). Isocyanic acid and ammonia in vehicle emissions. *Transportation Research Part D: Transport and Environment, 49*, 259-270. doi:10.1016/j.trd.2016.08.039

Tang, J., Li, Y., Li, X., Jing, S., Huang, C., Zhu, J., . . . Huang, D. (2021). Intermediate volatile organic compounds emissions from vehicles under real world conditions. *Science of The Total Environment, 788*, 147795. doi:10.1016/j.scitotenv.2021.147795

Thiruvengadam, A., Besch, M. C., Thiruvengadam, P., Pradhan, S., Carder, D., Kappanna, H., . . . Miyasato, M. (2015). Emission rates of regulated pollutants from current technology heavy-duty diesel and natural gas goods movement vehicles. *Environmental Science & Technology, 49*(8), 5236-5244. doi:10.1021/acs.est.5b00943

Thiruvengadam, A., Besch, M. C., Yoon, S., Collins, J., Kappanna, H., Carder, D. K., . . . Gautam, M. (2014). Characterization of particulate matter emissions from a current technology natural gas engine. *Environmental Science & Technology, 48*(14), 8235-8242. doi:10.1021/es5005973

Tobias, H. J., Beving, D. E., Ziemann, P. J., Sakurai, H., Zuk, M., McMurry, P. H., . . . Kittelson, D. B. (2001). Chemical analysis of diesel engine nanoparticles using a nano-DMA/thermal desorption particle beam mass spectrometer. *Environmental Science & Technology, 35*(11), 2233-2243. doi:10.1021/es0016654

Vu, D., Roth, P., Berte, T., Yang, J., Cocker, D., Durbin, T. D., . . . Asa-Awuku, A. (2019). Using a new Mobile Atmospheric Chamber (MACh) to investigate the formation of secondary aerosols from mobile sources: The case of gasoline direct injection vehicles. *Journal of Aerosol Science, 133*, 1-11. doi:10.1016/j.jaerosci.2019.03.009

Wang, M., Li, S., Zhu, R., Zhang, R., Zu, L., Wang, Y., & Bao, X. (2020). On-road tailpipe emission characteristics and ozone formation potentials of VOCs from gasoline, diesel and liquefied petroleum gas fueled vehicles. *Atmospheric Environment, 223*, 117294. doi:10.1016/j.atmosenv.2020.117294

Watne, A. K., Psichoudaki, M., Ljungstrom, E., Le Breton, M., Hallquist, M., Jerksjo, M., . . . Hallquist, A. M. (2018). Fresh and Oxidized Emissions from In-Use Transit Buses Running on Diesel, Biodiesel, and CNG. *Environmental Science & Technology, 52*(14), 7720-7728. doi:10.1021/acs.est.8b01394

Worton, D. R., Isaacman, G., Gentner, D. R., Dallmann, T. R., Chan, A. W., Ruehl, C., . . . Goldstein, A. H. (2014). Lubricating oil dominates primary organic aerosol emissions from motor vehicles. *Environmental Science & Technology, 48*(7), 3698-3706. doi:10.1021/es405375j

Zhao, Y., Hennigan, C. J., May, A. A., Tkacik, D. S., de Gouw, J. A., Gilman, J. B., . . . Robinson, A. L. (2014). Intermediate-volatility organic compounds: a large source of secondary organic aerosol. *Environmental Science & Technology, 48*(23), 13743-13750. doi:10.1021/es5035188

Zhou, L., Salvador, C. M., Priestley, M., Hallquist, M., Liu, Q., Chan, C. K., & Hallquist, A. M. (2021). Emissions and Secondary Formation of Air Pollutants from Modern Heavy-Duty Trucks in Real-World Traffic-Chemical Characteristics Using On-Line Mass Spectrometry. *Environmental Science & Technology, 55*(21), 14515-14525. doi:10.1021/acs.est.1c00412

Zhu, H., McCaffery, C., Yang, J., Li, C., Karavalakis, G., Johnson, K. C., & Durbin, T. D. (2020). Characterizing emission rates of regulated and unregulated pollutants from two ultra-low NOx CNG heavy-duty vehicles. *Fuel, 277*, 118192. doi:10.1016/j.fuel.2020.118192

Supplementary material of chapter 3

Exceedances of Secondary Aerosol Formation from In-Use Natural Gas Heavy-Duty Vehicles compared to Diesel Heavy-Duty Vehicles

Sahar Ghadimi [†], *Hanwei Zhu* [†], *Thomas D. Durbin* [†], *David R. Cocker III* [†], *Georgios Karavalakis* [†,*].

[†]University of California, Bourns College of Engineering, Center for Environmental Research and Technology (CE-CERT), 1084 Columbia Avenue, Riverside, CA, USA

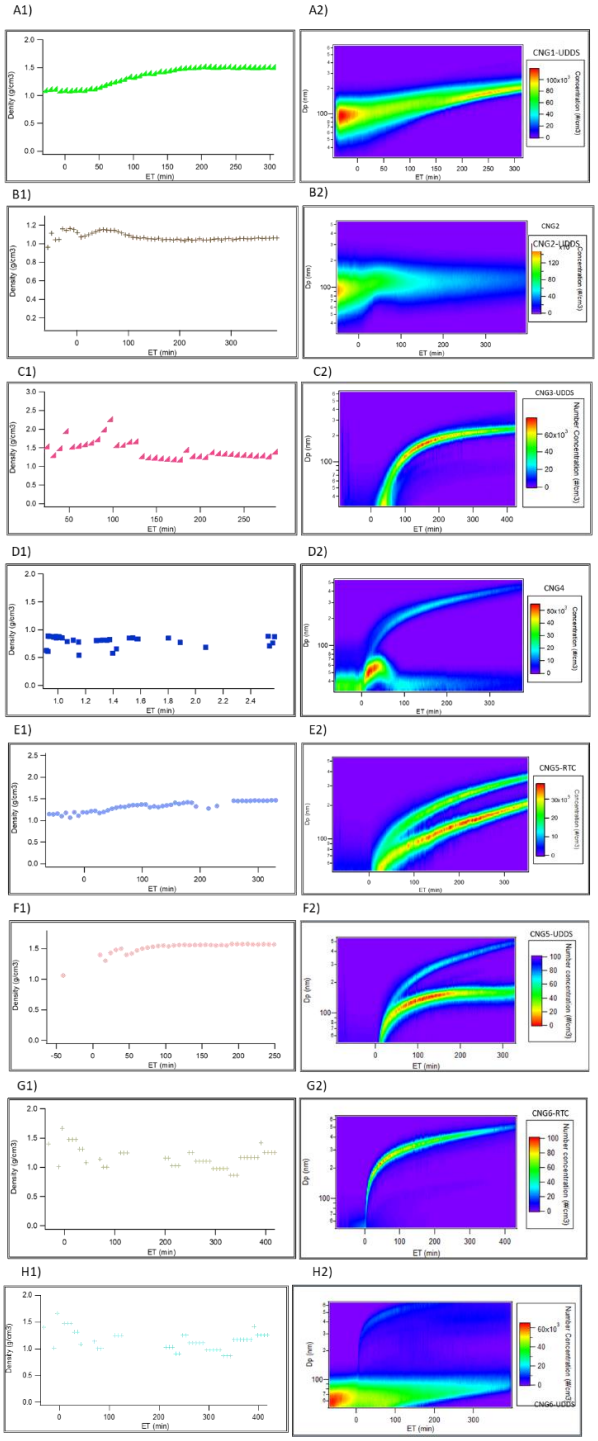

Figure S 3.1. Particle size-number concentration distribution and particle's density behavior: A1&A2) UDDS-0.02 CNG (CNG1); B1&B2) UDDS-0.2 CNG (CNG2); C1&C2) UDDS-0.02 CNG (CNG3); D1&D2) UDDS-0.02 CNG (CNG4); E1&E2) RTC-0.2 CNG (CNG5); F1&F2) UDDS-0.2 CNG (CNG5); B1&B2) UDDS-0.2 CNG (CNG5); G1&G2) RTC-0.2 CNG (CNG6); H1&H2) UDDS-0.2 CNG (CNG6).

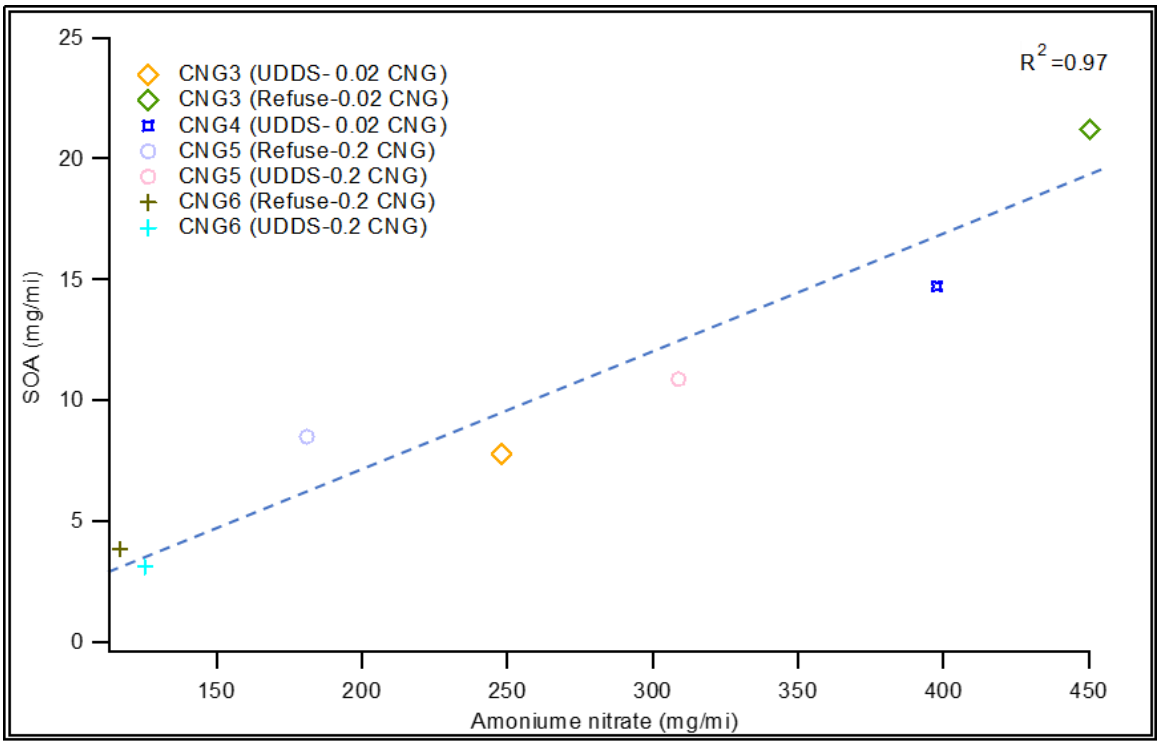

Figure S 3.2. The correlation between SOA formation and Ammonium nitrate formations in the CNG3-6 vehicles.

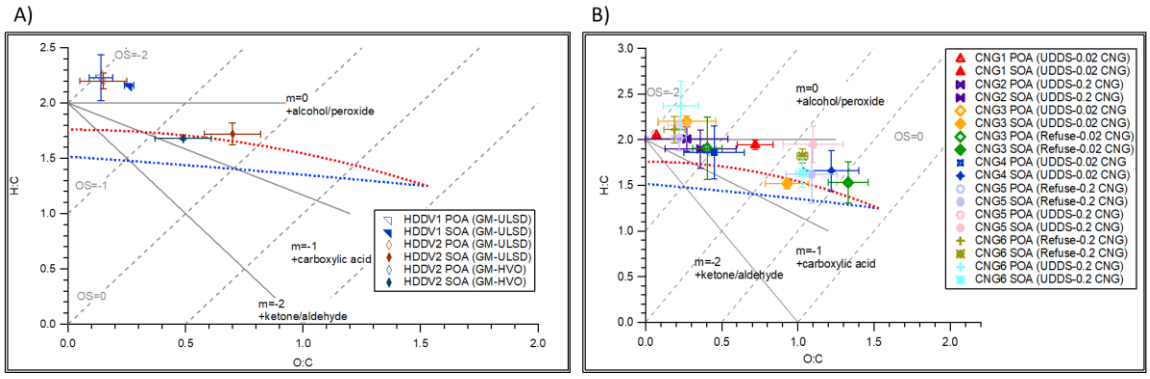

Figure S 3.3. Van Krevelen diagram showing the atomic H:C vs. O:C ratios for POA and SOA. Data corresponds to the A) HDDV1 and HDDV2; B) GNG1-CNG6; Note: the less oxidized points refer to POA, and the corresponding more oxidized points refer to SOA. All the corresponding O:C and H:C reported for SOA were calculated by subtracting the chemical compositions OA(5h) from POA using mass balance.

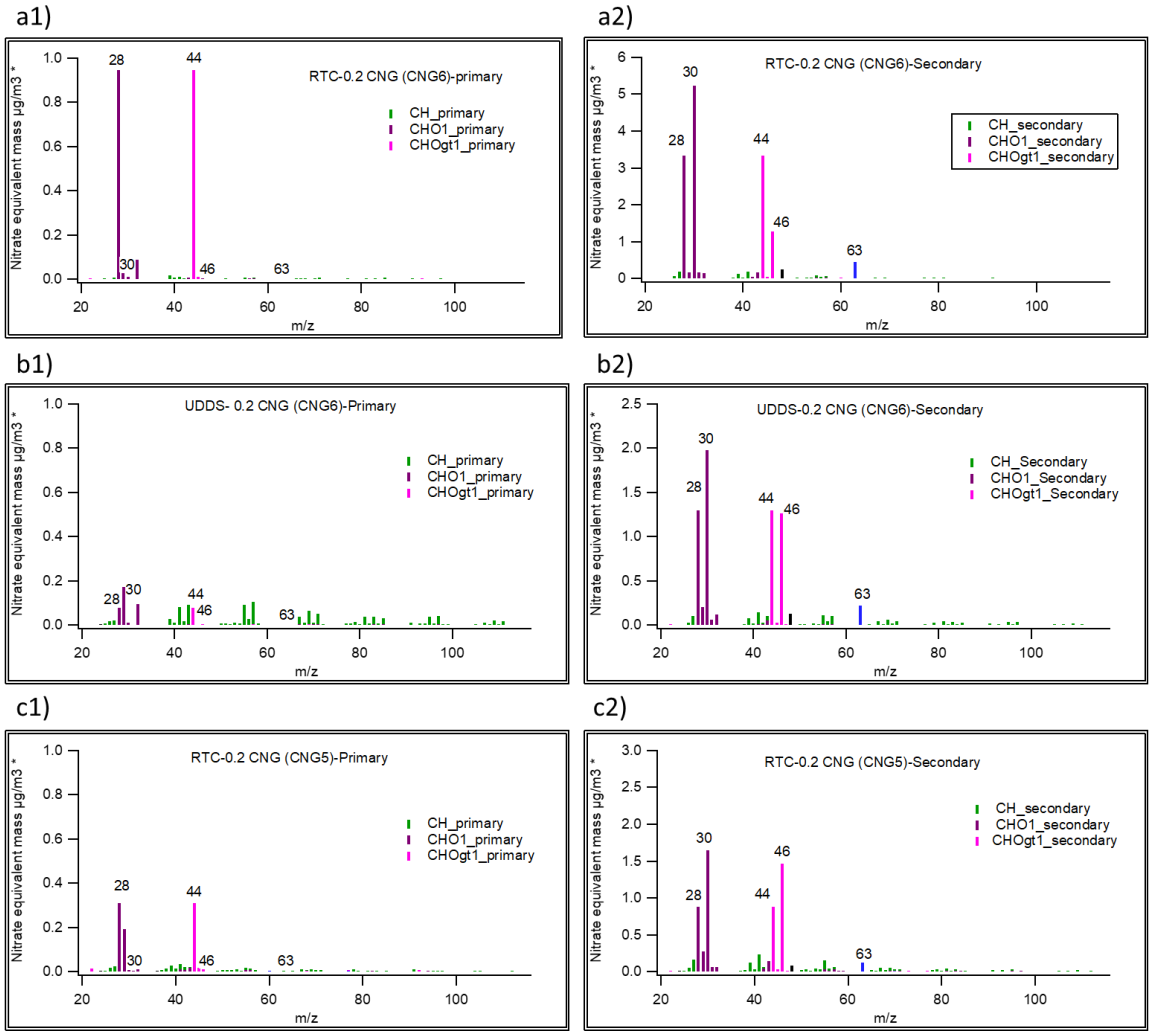

Figure S 3.4. Average HR mass spectra of POA, and OA (5 h) normalized to the total organic mass for CNG vehicle using two different fuel technology (0.02 CNG vs 0.2 CNG): a) CNG6 (RTC-0.2 CNG) POA (a1) and OA (5 h) (a2); b) CNG6 (UDDS-0.2 CNG) POA (b1) and OA (5 h) (b2); c) CNG5 (RTC-0.2 CNG) POA (c1) and OA (5 h) (c2).

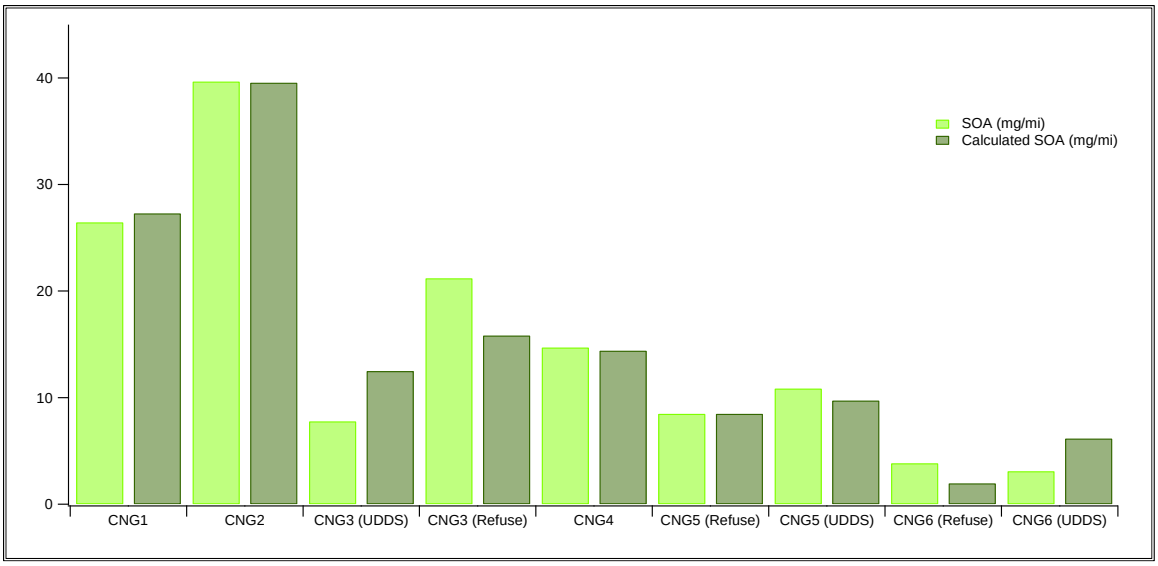

Figure S 3.5. The SOA calculation using equation 1 vs the SOA measured form the chamber experiments.

Table S 3.1. Shows the THC, CO, NH_3, PM, and the calculated non-methane organic gas (NMOG) emissions.

Experiment	THC (g/mi)	CO (g/mi)	NMHC (g/mi)	NOx (g/mi)	NH_3 (g/mi)	PM (mg/mi)	NMOG (mg/mi)
HDDV1 (GM-ULSD)	0.035	0.026	0.025	0.70	0.00	0.18	0.049
HDDV2 (GM-ULSD)	0.028	0.00	0.014	1.9	0.40	0.53	0.050
HDDV2 (GM-HVO)	0.023	0.00	0.013	2.7	0.044	0.37	0.032
CNG1 (0.02 CNG-UDDS)	0.50	5.04	0.00	1.4	0.35	47	0.012
CNG 2 (0.2 CNG-UDDS)	11	66	1.02	16	0.0011	85	1.4
CNG 3 (0.02 CNG-UDDS)	2.3	16	0.00	0.15	0.87	3.2	0.026
CNG3 (0.02 CNG-Refuse)	1.6	29	0.00	0.16	1.2	12	0.032
CNG 4 (0.02 CNG-UDDS)	1.2	12	0.00	1.8	0.35	4.4	0.054
CNG 5 (0.2 CNG-Refuse)	5.0	41	0.00	2.7	1.2	1.4	0.065
CNG 5 (0.2 CNG-UDDS)	4.2	23	0.00	4.3	1.7	2.3	0.051
CNG 6 (0.2 CNG-Refuse)	9.6	39	0.00	2.5	0.77	1.5	0.090
CNG 6 (0.2 CNG-UDDS)	6.7	41	0.00	3.8	1.1	1.8	0.079

Table S 3.2. Shows the tested vehicles information.

Experiment	After-treatments	Fuel Type	Driving Cycle	Engine Size (L)	Model year	ODO miles
HDDV1	**DOC+DPF+SCR**	**ULSD**	**GM**	**11.9**	**2016**	**221,199**
HDDV2	**DOC+DPF+SCR**	**ULSD&HVO**	**GM**	**12.8**	**2015**	**372,191**
CNG1	**TWC**	**0.02 CNG**	**UDDS**	**8.9**	**2018**	**52,884**
CNG2	**TWC**	**0.2 CNG**	**UDDS**	**8.9**	**2012**	**324,785**
CNG3	**TWC**	**0.02 CNG**	**UDDS & Refuse**	**8.9**	**2018**	**146**
CNG4	**TWC**	**0.02 CNG**	**UDDS**	**8.9**	**2018**	**96,698**
CNG5	**TWC**	**0.2 CNG**	**UDDS & Refuse**	**8.9**	**2011**	**67,291**
CNG6	**TWC**	**0.2 CNG**	**UDDS & Refuse**	**8.9**	**2017**	**31,510**

Chapter 4 : Influence of Continuous NO Injection on SOA Yield from Biogenic Precursors: A Comprehensive Branching Ratio Study

Sahar Ghadimi[1], Huawei Li[1], William Porter[2], David R. Cocker[1]

[1]University of California, Bourns College of Engineering, Center for Environmental Research and Technology (CE-CERT), 1084 Columbia Avenue, Riverside, CA, USA

[2]Department of Chemical and Environmental Engineering, Bourns College of Engineering, University of California, Riverside, CA, USA

Abstract:

Oxidation of α-pinene as a biogenic precursor is responsible for a large amount of secondary organic aerosol (SOA) formations in the atmosphere but detailed mechanisms and effects are still elusive. α-Pinene reacts with $\cdot OH$ and O_3 in the atmosphere, following by the bimolecular reactions with both NO and $HO_2^{\cdot}$ to form SOA. The fate of gas-phase organic oxidation reactions is dependent on NO and $HO_2^{\cdot}$ levels. The branching ratio, β, is defined as the fraction of organic peroxy radical ($RO_2^{\cdot}$) consumption by NO over both NO and $HO_2^{\cdot}$ pathways. The SOA yields and chemical compositions from α-pinene photooxidation was evaluated in a newly designed 118 m^3 fixed-volume environmental chamber under atmospherically relevant and controlled chemical conditions. The experiments were designed using SAPRC-11 simulation and conducted at fixed β values, which were controlled via continuous NO injection. For no NO experiments (β=0), the NO concentration remained below 0.2 ppb during the photooxidation process for all 20, 40 and

80 ppb α-pinene concentrations. Despite continuous NO injection in β=0.3 experiments, the low NO concentrations were achieved due to both continuous NO injection and the presence of H_2O_2. In β=0.3 experiments, the NO level was below 0.5 for both 20 and 40 ppb α-pinene, while in 80 ppb α-pinene experiment the NO level gradually increased to ~2 ppb in 300 min (when all HC consumed). Roughly the same SOA yields were obtained for β=0.3 experiments (Y= 21.47%-30.45%) compared to β=0 conditions (Y= 20.22%-29.98%). The SOA yields were also investigated for different high NO regimes (all b=1) including high NO (minimum sufficient NO to achieve b=1), 1.5X high NO and 2X high NO conditions. SOA formation was substantially suppressed at 2X high NO levels (Y=0.56%-5.75%) compared to high NO levels (Y=5.94%-16.74%) all under β=1 condition. For experiments with lower 10 ppb NO concentration (β=0, 0.3), a direct correlation was observed between the SOA yields and both $RO_2^{\cdot}$ life-time and $HO_2^{\cdot}/RO_2^{\cdot}$. The $HO_2^{\cdot}/RO_2^{\cdot}$ ratio was higher in β=0.3 experiments, while $RO_2^{\cdot}$ autooxidation was higher in β=0 experiments due to the prolonged $RO_2^{\cdot}$ half-life. SOA formed from α-pinene photooxidation have O/C ranging from 0.40 to 0.65 along with H/C ranging from 1.48 to 1.80, under all b conditions. Regardless of the NO level, a little dependence in the degree of oxidation is observed in O/C and H/C of SOA in all experiments. Moreover, the SOA formation were also evaluated under classical experiment conditions in which the NO was added instantaneously at the beginning of the experiment. The continuous NO injection method (constant β) revealed lower SOA yield than variable β (traditional VOC-NO) experiments at lower initial hydrocarbon (HC) concentration and higher SOA yield at higher HC conditions. On the global scale, the modified set of VBS yield parameters from

β=0 and β=1 experiments were incorporated into GOES-Chem modeling to be able to perform a sensitivity test to observe the impact of the modified yields on a global scale. It was observed that increases of up to 1.1 ug m^{-3} were found in areas of high precursor emissions and base terpene SOA formation when using continuous NO injection experimental data under constant β conditions, representing concentration changes of up to 24% in those locations across modeled months.

Introduction and motivation:

Particulate matter (PM) adversely affects human health, environment, and climate change (H. Zhang et al., 2018). In troposphere, roughly 50% fraction of the submicron ambient aerosols mass consists of organic aerosols (OA), mainly secondary organic aerosols (SOA) (Jimenez et al., 2009). Biogenic volatile organic compounds (BVOCs), such as monoterpenes ($C_{10}H_{16}$) are some of the most important contributors to atmospheric secondary organic aerosol emissions due to their combined emissions rates and propensity to form SOA (Ng, Chhabra, et al., 2007). α-Pinene and β-pinene are two examples of monoterpenes and are mainly found in the resins of pine trees which are major contributors to primary biogenic hydrocarbon emission in the atmosphere (S.-H. Zhang, Shaw, Seinfeld, & Flagan, 1992). The total global monoterpene emissions are roughly 78 Tg yr^{-1} annually, which α-pinene accounting for roughly 25.5 Tg yr^{-1} (Sindelarova et al., 2022), Monoterpenes are mainly oxidized by hydroxyl radicals ($\cdot OH$), ozone (O_3) and nitrate (NO_3), leading to the formation of SOA (Guenther et al., 1995). $\cdot OH$ and O_3 are the main oxidants during the day, while NO_3 is the most abundant oxidant at night-times (Capouet

et al., 2008). α-Pinene is oxidized by ·OH radicals (to yield hydroxy alkyl radical) predominantly through the endocyclic double bond, followed by the reaction with O_2 to produce hydroxy peroxy radicals (known as $RO_2^{\cdot}$ in this work or also known as $RO_3^{\cdot}$ by considering all oxygen atoms) (Eddingsaas, Loza, Yee, Seinfeld, & Wennberg, 2012; Piletic & Kleindienst, 2022).

Depending on atmospheric conditions, the $RO_2^{\cdot}$ will react with different species, including, HO_2, NO, and other $RO_2^{\cdot}$ radicals. Moreover, when the $RO_2^{\cdot}$ life-time is sufficiently long, $RO_2^{\cdot}$ can undergo an intramolecular H-shift reaction (also known as $RO_2^{\cdot}$ isomerization) and subsequent O_2 addition (the combination of reactions known as autoxidation (Lee et al., 2023; Moller, Otkjaer, Chen, & Kjaergaard, 2020; Piletic & Kleindienst, 2022; Xu et al., 2019)), to form second generation oxidized peroxy radicals (named as $R'O_2^{\cdot}$ in this work, also known as $RO_5^{\cdot}$) and third generation oxidized peroxy radicals (named as $R''O_2^{\cdot}$ in this work, also known as $RO_7^{\cdot}$), which account for 5.8% and 4.6% of α-pinene products, respectively (Piletic & Kleindienst, 2022). These next generation products are highly oxygenated organic molecules (HOMs) with lower vapor pressures (Bianchi et al., 2019; Piletic & Kleindienst, 2022).

The SOA formation potential is represented by SOA yield (Y), which is defined as the produced aerosol mass (Mo) per hydrocarbon consumed (ΔHC). SOA yield highly depends on atmospheric conditions. Nitrogen oxides (NO_x) level is one of the key factors that impacts SOA yield (Ng, Chhabra, et al., 2007). The NO level alters the direction of peroxy-radical ($RO_2^{\cdot}$) reaction pathways, which then affects the distribution of oxidation products leading to different SOA yields. Under low-NO conditions, $RO_2^{\cdot}$ tend to react

more with $HO_2^{\cdot}$ to yield low volatility products. These products mainly contain hydroxy -OH, hydroperoxide -OOH, carbonyl -C=O, carboxylic acid O=C-OH and peroxyacid O=C-OOH functional groups that allow new particle formation via hydrogen bonding interactions (Eddingsaas, Loza, Yee, Chan, et al., 2012). According to Piletic *et al.*, formation of $R'O_2^{\cdot}$ and $R''O_2^{\cdot}$ is reported to be higher for low NO conditions (<10 ppb NO) and fall-off sharply >~10 ppb NO concentration (Piletic & Kleindienst, 2022). Chemical analysis of α-pinene photooxidation products by Eddingsaas *et al.* illustrated that under low NO conditions, the main first-generation oxidation products include a number of α-pinene hydroxy hydroperoxides and pinonaldehyde. They reported that only under low-NO conditions, pinonaldehyde undergoes further $^{\cdot}OH$ oxidation to produce a number of carboxylic acids and peroxyacids (pinic and pinonic acid) that are important low-volatile secondary organic components (Eddingsaas, Loza, Yee, Chan, et al., 2012; Eddingsaas, Loza, Yee, Seinfeld, et al., 2012).

Contrary, under high-NO conditions, $RO_2^{\cdot}$ radicals (obtained from α-pinene reaction with $^{\cdot}OH$ and O_2) reacts with NO resulting in the formation of organic nitrates and/or alkoxy radicals. Under high-NO conditions, pinonaldehyde was also found to be the major first-generation $^{\cdot}OH$ oxidation product. Eddingsaas *et al.* also claimed that under high-NO conditions, α-pinene and pinonaldehyde converted to organonitrates and peroxyacyl nitrates(Eddingsaas, Loza, Yee, Seinfeld, et al., 2012). These products are more volatile compared to the products formed under low NO conditions leading to lower SOA formations. According to Piletic *et al.*, high NO condition suppresses the formation of $R'O_2^{\cdot}$ and $R''O_2^{\cdot}$ (Piletic & Kleindienst, 2022).

However, only considering low-NO or high-NO conditions in SOA yield study do not account for the complex photooxidation conditions that many gas-phase species encounter. Likewise, Li *et al.* stated that at sub-ppb NO levels, $^{\cdot}OH$ formation was enhanced resulting in increasing $HO_2^{\cdot}$ and $RO_2^{\cdot}$ formation leading to higher SOA formation from aromatic precursors. The sub-ppb NO levels were achieved via continuous NO injection at low level. Also, they observed that both high initial NO concentration and NO free conditions resulted lower the SOA formation which arises from both NO suppression and promotion pathways to SOA formation (Li, Tang, & Cocker, 2015).

The competition of $RO_2^{\cdot}$ reaction in either NO or $HO_2^{\cdot}$ pathways are defined by "branching ratio" (β) which is the ratio of NO + $RO_2^{\cdot}$ reaction rate over the total $RO_2^{\cdot}$ decay rate (in both NO and $HO_2^{\cdot}$ pathways) **Equation 4.1** (Farina, Adams, & Pandis, 2010; Pye, Chan, Barkley, & Seinfeld, 2010). The rate constants for reactions of peroxy radical with NO and $HO_2^{\cdot}$ were shown as k ($RO_2^{\cdot}$ + NO) = 8.43×10^{-12} cm^3.$molecules^{-1}s^{-1}$ and k ($RO_2^{\cdot}$ + $HO_2^{\cdot}$) = 1.87×10^{-11} cm^3. $molecules^{-1}s^{-1}$, respectively.

$$\beta = \frac{k_{RO_2+NO}[NO]}{k_{RO_2+NO}[NO]+k_{RO_2+HO_2}[HO_2]} \qquad \textbf{Equation 4.1}$$

Over the last two decades, there have been many environmental chamber laboratory studies on aerosol formations from biogenic hydrocarbons. Most previous BVOC-NO_x photooxidation studies injected NO instantaneously at the beginning of the experiment (Aruffo et al., 2022; Ng, Chhabra, et al., 2007); consequently, the BVOC experience different branching ratio that decreases substantially from β ~ 1 to β ~ 0 throughout the experiment, providing multiple NO conditions **Figure S 4.1**. In these studies, a high NO

experiment starts under high-NO conditions but rapidly progresses to low NO conditions. However, Porter *et al.* modeled the mean atmospheric β value using GEOS-Chem for different regions and reported that the β value "remains relatively constant" through most of the day-time; depending on the NO concentrations coming from anthropogenic activities in different regions that value is typically in the 0.25 to 0.75 range (Porter, Jimenez, & Barsanti, 2021). Ng. *et al.* investigated the SOA formations from α-pinene under no NO (just H_2O_2), mid-NO (H_2O_2 + instantaneous NO injections: $\frac{\Delta HC}{NO} = 0.07$), and high NO (HONO injected before photooxidation: $\frac{\Delta HC}{NO} = 0.03$ to 0.12) and reported SOA yields of 38-46%, 21%, and 7-16%, respectively (Ng, Chhabra, et al., 2007). Eddingsaas *et al.* also investigated the SOA formation from α-pinene precursor using HONO injections (before initiation of photooxidation) and reported an SOA yield ~7% at high NO_x conditions ($\frac{\Delta HC}{NO_x} = 0.025$ to 0.065) while H_2O_2 injections in the absence of NO_x were reported to have ~26% SOA yield (Eddingsaas, Loza, Yee, Chan, et al., 2012). Biwu *et al.* investigated the SOA formations under high NO_x conditions, by injecting the NO concentrations at the beginning of the experiment, and reported SOA yields ranging between 4% to 11% ($\frac{\Delta HC}{NO_x} = 0.2$) (Chu et al., 2012). Zhoa *et al.* investigated the SOA formations under no NO and high NO ($\frac{\Delta HC}{NO} = 1.0$), and reported the SOA yields of ~10% and ~3.0%, respectively (Zhao et al., 2018).

In this study, the SOA yield from α-pinene precursor as a biogenic emission was evaluated using controlled continuous NO injections to obtain constant branching ratio (β value) throughout the experiment which resemble real atmospheric conditions. All

experiments were performed under 3 different branching ratio β: 1) β equals to zero as no NO experiments, 2) β equals to 0.3 and 3) β equals to 1.0 as high NO experiments. Then, the corresponding experiments were performed to evaluate SOA yield from α-pinene precursor under classical experimental conditions by injecting NO instantaneously at the beginning of each experiment. The outcomes of this novel study were used in GEOS-Chem simulation to develop more accurate representation of aerosol formation potential during day-time for improve prediction of the atmospheric SOA model.

Methods:

All experiments were conducted in a 118 m^3 fixed-volume UC Riverside/CE-CERT environmental chamber illuminated with 272 Sylvania 350 nm 115 W black-lights, within a temperature controlled enclosure flushed with purified air. All experiments were run at 298 ± 1 K, under dry conditions (RH < 0.1%) and with a NO_2 photolysis rate (J_{NO2} , or k_1) of 0.401 min^{-1}.

α-Pinene (>99%) was purchased from Sigma-Aldrich and its purity was confirmed by ^1H NMR and ^{13}C NMR (**Figure S 4.6**-**Figure S 4.7**). H_2O_2 (50 wt % in H_2O) was used as a hydroxyl and hydroperoxide radical source (HO_x); 1 ppm of H_2O_2 was injected initially for 15 min into the chamber before initiation of photooxidation process for β=0 and β=0.3 experiments conditions, while "no" H_2O_2 was injected for β=1 experiments. The ·OH concentrations were estimated using measured HC decay rates (Eq. 4) and also evaluated using SAPRC-11 simulation. The initial concentration of injected α-pinene ranged between 20 ppb to 100 ppb.

The NO injection rates for each continuous experiment were designed and calculated using SAPRC-11 modelling to achieve constant β values (either 0, 0.3, 1) for the duration of the run. Real-time concentrations of NO and radical species such as $HO_2^{\cdot}$ that are important for β calculation were predicted using SAPRC-11 and Eq. 1 (Carter & Heo, 2013). **Figure S 4.1** shows the calculated β ratios for each β=0.3 and β=1 experiments. Each experiment was performed without seed aerosols. The NO injection started with the initiation of photooxidation when the UV light was turned on in continuous NO experiments.

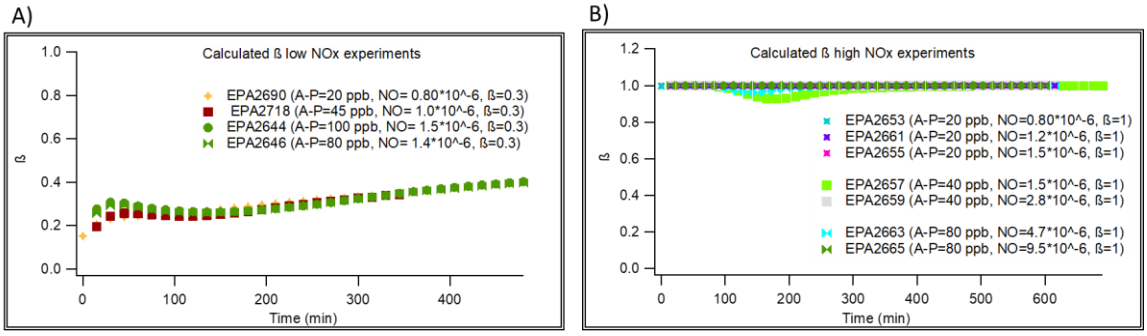

Figure 4.1. Calculated β ratio using SAPRAC-11: A) A) calculated β values for low NO experiments, β=0.3. B) calculated β values for high NO experiments, β=1.

In low NO experiment, the continuous NO injection (cc/min) into the chamber for β=0.3 experiments were achieved using a gas-phase titration calibrator (model CSI 1700). Higher NO injection rates (>50 cc/min) for β=1 experiments used a calibrated NO mass flow controller. The SAPRC-11 simulations were verified by comparing experimental gas-phase traces (O_3, NO_x, and HC) with SAPRC-11 simulations. Classical experiments were designed to correspond to continuous injection experiments; in classical experiments the NO injections (target ppb) were calculated using $RO_2^{\cdot}$ radical "depletion time" multiplied

by the NO injection rate in the corresponding continuous experiments and were injected before irradiation commenced. The SOA yield (Y) is defined **Equation 4.2** as the ratio of measured SOA formation (SOA mass: ΔM_0) at the end of the experiment (corrected for particle wall-loss) divided by the total consumed SOA precursor (ΔHC). Experimental conditions including target β values, gas-phase data, and SOA yield for each experiment is documented in **Table 4.1**.

$$Y = \frac{\Delta M_0}{\Delta HC} \qquad \text{Equation 4.2}$$

The organic species were grouped into five volatility bins (C_i^* ; 0.1, 1, 10, and 100 ug m^{-3}) (Donahue, Robinson, Stanier, & Pandis, 2006). The volatility basis set parameters (α_{i,HO_2}, $\alpha_{i,NO}$) were calculated using β=0 and β=1 experiments for α_{i,HO_2} and $\alpha_{i,NO}$, respectively. In this work, α_{i,HO_2} and $\alpha_{i,NO}$ were determined via MATLAB Curve Fitting Tool by minimizing the square of the residuals between the theoretical fit **(Equation** 4.3**)** and experimental data (M_O vs Y).

$$\mathbf{Y} = \left(\sum\left(\mathbf{1} + \frac{c_i^*}{M_o}\right)^{-1} * \boldsymbol{\alpha_{i,NO}} * \boldsymbol{\beta}\right) + \left(\sum\left(\mathbf{1} + \frac{c_i^*}{M_o}\right)^{-1} * \boldsymbol{\alpha_{i,HO_2}} * (\mathbf{1} - \boldsymbol{\beta})\right) \qquad \textbf{Equation 4.3}$$

A home-built scanning mobility particle sizer (SMPS) consisting of a TSI 3080 Electrostatic Classifier, TSI 3081 long column Differential Mobility Analyzer (DMA) column, and a TSI 3776 CPC was used to obtain the particle size distribution (27 nm to 686 nm). The effective particle density was measured with a Kanomax aerosol particle mass (APM) analyzer coupled to an SMPS, as described in Malloy *et al.* (Malloy et al., 2009). An Agilent gas chromatography (model 6890) with flame ion detectors (GC-FID) was used to measure VOC concentrations. An Aerodyne high-resolution time-of-flight

aerosol mass spectrometer (HR-ToF-AMS) was used to measure the chemical composition of the non-refractory aerosol. The HR-ToF-AMS was operated in both V and W modes, and the data processing was completed using the ToF-AMS Analysis Toolkit 1.57 and ToF-AMS HR analysis 1.16. Gas-phase data were analyzed using a Thermal Environmental Instruments Model 42C chemiluminescence NO analyzer and a Dasibi Environmental Corp. Model 1003-AH O_3 analyzer.

Global branching ratios were simulated from a global 3-D model of atmospheric chemistry driven by meteorological input from the Goddard Earth Observing System (GEOS-Chem) based on NO and HO_2 concentrations. The GEOS-Chem version 14.0.2 at 4ºx5º horizontal resolution was used, driven by the MERRA-2 meteorology data product from the NASA Global Modeling and Assimilation Office (GMAO). Aerosol formation was represented in part by a two-product reversible partitioning model for monoterpene and aromatic oxidation based on Pye *et al.* with updates from Marais *et al.* (Marais et al., 2016; Pai et al., 2020; Pye et al., 2010). The monthly mean model output after a one-month spin up for terpene SOA (TSOA) was provided using base GEOS-Chem, as well as total and percent change in output when using modified yield parameters.

Table 4.1. Experimental conditions for α-pinene photooxidation for both continuous NO injection and classical experiments.

Run Number	β	α-pinene (ppb)	H_2O_2	NO (ppm/sec) or NO (ppb)	Avg. $\cdot OH$ (ppm)	Yield %
EPA2628	0.3	19	1	0.80×10^{-6}	3.86×10^{-7}	27.29
EPA2690	0.3	17	1	0.85×10^{-6}	4.05×10^{-7}	30.45
EPA2630	0	18	1	0	3.95×10^{-7}	26.96
EPA2709	0	20	1	0	2.14×10^{-7}	29.98

EPA2632	0.3	44	1	0.90×10^{-6}	3.56×10^{-7}	21.47
EPA2718	0.3	46	1	1.0×10^{-6}	2.56×10^{-7}	23.52
EPA2634	0	46	1	0	1.07×10^{-7}	20.85
EPA2747	0	45	1	0	2.52×10^{-7}	20.22
EPA2646	0.3	82	1	1.4×10^{-6}	3.53×10^{-7}	25.93
EPA2642	0	81	1	0	9.10×10^{-8}	24.33
EPA2644	0.3	102	1	1.5×10^{-6}	2.95×10^{-7}	23.6
EPA2714	0	103	1	0	1.18×10^{-7}	22.22
EPA2641	0	105	1	0	3.01×10^{-7}	22.87
EPA2653	1	20	0	0.80×10^{-6}	2.37×10^{-7}	5.94
EPA2661	1	20	0	1.2×10^{-6}	2.44×10^{-7}	1.99
EPA2655	1	21	0	1.5×10^{-6}	2.33×10^{-7}	1.03
EPA2657	1	41	0	1.5×10^{-6}	2.96×10^{-7}	11.90
EPA2659	1	41	0	2.8×10^{-6}	2.59×10^{-7}	5.75
EPA2663	1	82	0	4.7×10^{-6}	5.32×10^{-8}	16.74
EPA2665	1	80	0	9.5×10^{-6}	3.22×10^{-8}	0.564
EPA2692	Classical (equal to $\beta = 0.3$)	21	1	26	5.92×10^{-7}	18.1
EPA2694	Classical (equal to $\beta = 0.3$)	20	1	27	2.18×10^{-7}	19.4
EPA2674	Classical (equal to $\beta = 0.3$)	80	1	43	2.51×10^{-7}	37.41
EPA2682	Classical (equal to $\beta = 0.3$)	100	1	52	2.63×10^{-7}	41
EPA2697	Classical (equal to $\beta = 0.3$)	39	1	40	1.18×10^{-7}	38.3
EPA2687	Classical (equal to $\beta = 1$)	75	0	141	2.55×10^{-7}	16.3
EPA2695	Classical (equal to $\beta = 1$)	23	0	40	2.48×10^{-7}	1.9
EPA2698	Classical (equal to $\beta = 1$)	39	0	63	4.46×10^{-7}	15.2

Result and Discussion:

Each chamber expperiment was performed for more than 20 hours, to obtain a plateau in particle volume before ending the experiments. The average experimental β values varies from 0 to 1, depending on the NO level, VOC concentrations and H_2O_2 injection. The average ·OH radical concentration in the chamber was estimated to be ~10^{-7} ppm by **Equation 4.4 (Figure 4.2)**

$$\frac{\Delta(HC)}{[HC]*\Delta t} = k_{OH} \times [OH] + k_{O_3} \times [O_3] \qquad \textbf{Equation 4.4}$$

where k_{OH} (5.3×10^{-11} cm^3 $molec.^{-1}$ s^{-1}) and k_{O_3} (8.4×10^{-17} cm^3 $molec.^{-1}$ s^{-1}) (Gill & Hites, 2002; Khamaganov & Hites, 2001) are the reaction rate constant of α-pinene with ·OH and O_3, respectively, [HC] is the average hydrocarbon concentration (μg m^{-3}) for a given time step Δt, and Δ[HC] was the change of hydrocarbon mass concentration (μg m^{-3}) during the Δt interval. **Equation 4.5** assumes α-pinene only reacts with ·OH and O_3. Estimated chamber ·OH radical concentration is typical for midday ambient values (10^{-6}-10^{-7} ppm (Tanner & Eisele, 1995)).

Between 83.0% to 96.1% of α-pinene was consumed in reaction with ·OH for all experimental conditions. It was also observed that the O_3 was negligible at the beginning of the experiments and was formed at the point of the experiments when most of the α-pinene had already been consumed by reacting with ·OH **Figure S 4.1.** Calculated β ratio using SAPRAC-11: A) The β values of classical experiment vs β=0.3 for 20 ppb. B) The β values of classical experiment vs β=0.3 for 80 ppb.. It is also important to note that under high NO conditions, the O_3 formations were significantly higher in classical experiments

compared to continuous experiments (**Figure S 4.1B**). HC decay rates were higher in the presence of NO (β=0.3 and 1) compared to the β=0 conditions, where there was no NO added into the system. For example, when using 20 ppb α-pinene, it took about 100 min, 300 min, and 500 min to completely consume all HC under β=1, 0.3 and 0 conditions, respectively (**Figure S 4.2A**).

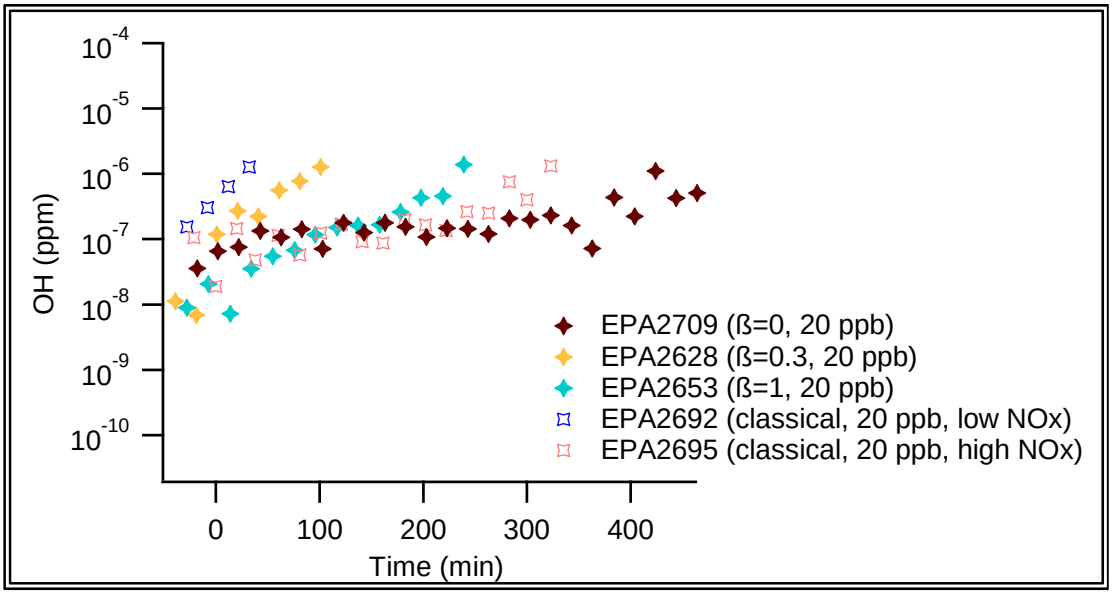

Figure 4.2. The average ·**OH** concentrations for β equals to 0, 0.3, 1, and corresponding classical experiments for 20 ppb of α-pinene concentration. Note: ·**OH** concentration measured until all HC was consumed (see **Equation 4.4**).

Figure 4.4 A-B shows final SOA yields (%) vs SOA mass formed (ug/m^3) for 20 ppb, 40 ppb, 80 ppb, 100 ppb target a-pinene concentrations for both β=0.3 and β=0 conditions. A higher a-pinene decay rate for β=0.3 were observed compared to β=0 conditions which was consistent with a higher ·OH concentration in β=0.3 compared to β=0 experiment **Figure 4.2**. The SOA yield for β=0.3 (Y= 21.47%-30.45%) were roughly the same as β=0 conditions (Y= 20.22%-29.98%) with yields for β=0.3 being slightly higher. Simulated gas-phase data suggested that the $RO_2^{\cdot}$ lifetime (leading to further autooxidation)

and $HO_2^{\cdot}/RO_2^{\cdot}$ ratios directly affect the SOA formation. The $HO_2^{\cdot}/RO_2^{\cdot}$ ratios (calculated from SAPRAC11 gas-phase data) were higher in β=0.3 conditions compared to both β=0, and 1 (**Figure 4.3A-B)**. On the other hand, the $RO_2^{\cdot}$ lifetime was higher in β=0 condition (**Figure 4.3C-D)** leading to multi-generation oxidized peroxy radicals (autooxidation) and subsequent formation of highly oxygenated organic molecules (HOMs) (Bianchi et al., 2019; Lee et al., 2023; Moller et al., 2020; Piletic & Kleindienst, 2022; Xu et al., 2019). The $RO_2^{\cdot}$ lifetime was simulated using SAPRC-11 for all β values in this study (β=0, 0.3, 1) with increased $RO_2^{\cdot}$ lifetime for lower β values **Figure 4.3** (**Figure S 4.3**).

The NO concentration remained below 0.2 ppb during the photooxidation process for no NO experiments (β=0) for all 20, 40 and 80 ppb α-pinene concentrations (**Figure S 4.3)**. The NO level for β=0.3 experiments was below 0.5 for both 20 and 40 ppb α-pinene, while in 80 ppb α-pinene experiment the NO level gradually increased to ~2 ppb in 300 min (when all HC consumed) **Figure S 4.3**. Despite continuous NO injection in β=0.3 experiments, the low NO concentrations remained low with ~95% converting to NO to NO_2. Under these low NO levels, the formation of next generation oxidized peroxy radicals ($R'O_2^{\cdot}$ and $R"O_2^{\cdot}$) from autoxidation reaction is expected (Piletic & Kleindienst, 2022). The NO_x concentrations in the β=0 experiment remained below 2 ppb during the photooxidation process for all 20, 40 and 80 ppb α-pinene concentrations **(Figure S 4.3).**

It was observed that the SOA yield was slightly higher at 20 ppb α-pinene concentrations (**Figure 4.4A**). Background SOA formation was ruled out as a cause after repeating the same photooxidation experiment without HC injection and observing only negligible amounts of SOA. This effect was also observed by Eddingsaas, N. C. *et al.*

without further rationalization (Eddingsaas, Loza, Yee, Chan, et al., 2012). We originally hypothesized that the $RO_2^{\cdot}$ half-life for 20 ppb is higher leading to enhanced $RO_2^{\cdot}+RO_2^{\cdot}$ reaction or increased SOA via auto-oxidation. However, SAPRC-11 modelling indicates that the $RO_2^{\cdot}$ halflife was shorter in 20 ppb α-pinene compared to 40 ppb α-pinene (see **Figure 4.3**). The higher SOA yields for 20 ppb α-pinene experiments can be rationalized by the higher $HO_2^{\cdot}/RO_2^{\cdot}$ ratio compared to all 40, 80, 100 ppb of α-pinene experiments (**Figure 4.3 A-B)**.

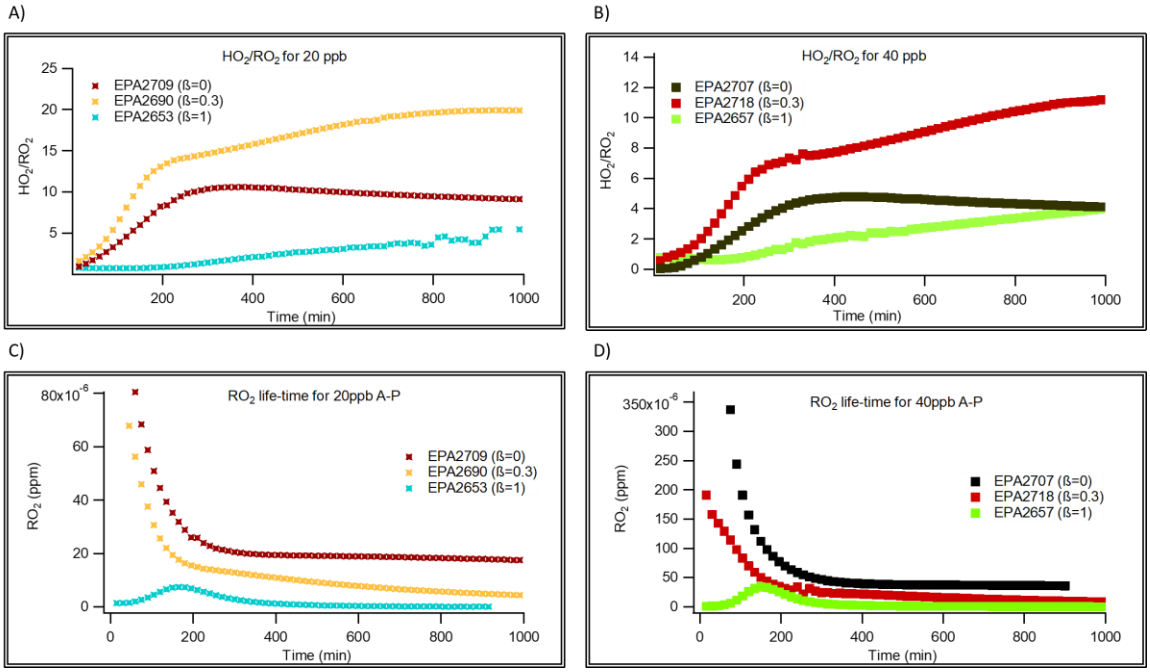

Figure 4.3. $HO_2^{\cdot}/RO_2^{\cdot}$ ratios under β = 0, 0.3, 1 at A) 20ppb; B) 40ppb; $RO_2^{\cdot}$ lifetime simulated under β = 0, 0.3, 1 at C) 20 ppb, D) 40 ppb.

The SOA yields were investigated for different high NO regimes (all β=1) including high NO (minimum sufficient NO to achieve β=1), 1.5X high NO, and 2X high NO conditions. SOA formation at 2X high NO conditions were lower than high NO conditions despite their similar β=1 values **(Figure 4.4 C-D)**. The $RO_2^{\cdot}$ lifetimes were longer under

high NO conditions compared to 2X high NO conditions according to SAPRC-11 simulation (**Figure S 4.4)**. Higher $RO_2^{\cdot}$ lifetimes increase the chance of autooxidation leading to the formations of lower volatility species and therefore higher SOA yields (Afreh, Aumont, Camredon, & Barsanti, 2021; Kurten et al., 2016). Similarly, the NO concentration remained below 10 ppb in the first 600 minutes in the 1X high NO experiments (β=1) for all α-pinene concentrations, allowing formation of next generation oxidized peroxy radicals ($R'O_2^{\cdot}$ and $R"O_2^{\cdot}$) from autoxidation reaction resulting in the higher SOA yield in 1X high NO condition compared to 2X high NO experiments (β=1) where NO exceeded 10 ppb within the first 600 minutes **(Figure S 4.3** NO**)** (Piletic & Kleindienst, 2022). SOA yields were substantially lower for β=1 compared to β=0 or 0.3, consistent with the previous studies on NO effects using biogenic precursors (Eddingsaas, Loza, Yee, Seinfeld, et al., 2012; Ng, Chhabra, et al., 2007; Ng, Kroll, et al., 2007; Wu et al., 2020; Zhao et al., 2018). The lowest SOA yield formed from 80 ppb HC consumption under 2X high NO condition (SOA yield = 0.56%) where the $RO_2^{\cdot}$ lifetime was the shortest among all experiments in this study and the NO level exceeded 10 ppb after only 20 minutes of photooxidation process (**Figure S 4.4**, **Figure S 4.3** NO**)**.

The gas–particle partitioning of an organic species depends on its vapor pressure and the concentration of organic material in the particle phase (Donahue et al., 2006). The volatility basis set (VBS) parameters have been calculated (**Equation 4.3)** for β=0 and 1. The β=0 condition was supplemented with data from Eddingsaas *et al.* for similar experimental conditions to calculate the α_{i,HO_2}. The α_{i,HO_2} were 2.2×10^{-14}, 0.27, 0.00091, 3.9×10^{-5} for C_i^* of 0.1, 1, 10, 100 (ug/m^3), respectively. Moreover, the $\alpha_{i,NO}$ were

calculated using the data acquired for the β = 1 conditions in this study as 1.7 × 10^{-6}, 6.6 × 10^{-7}, 0.087, 0.23 for C_i^* bins of 0.1, 1, 10, 100 (ug/m^3), respectively.

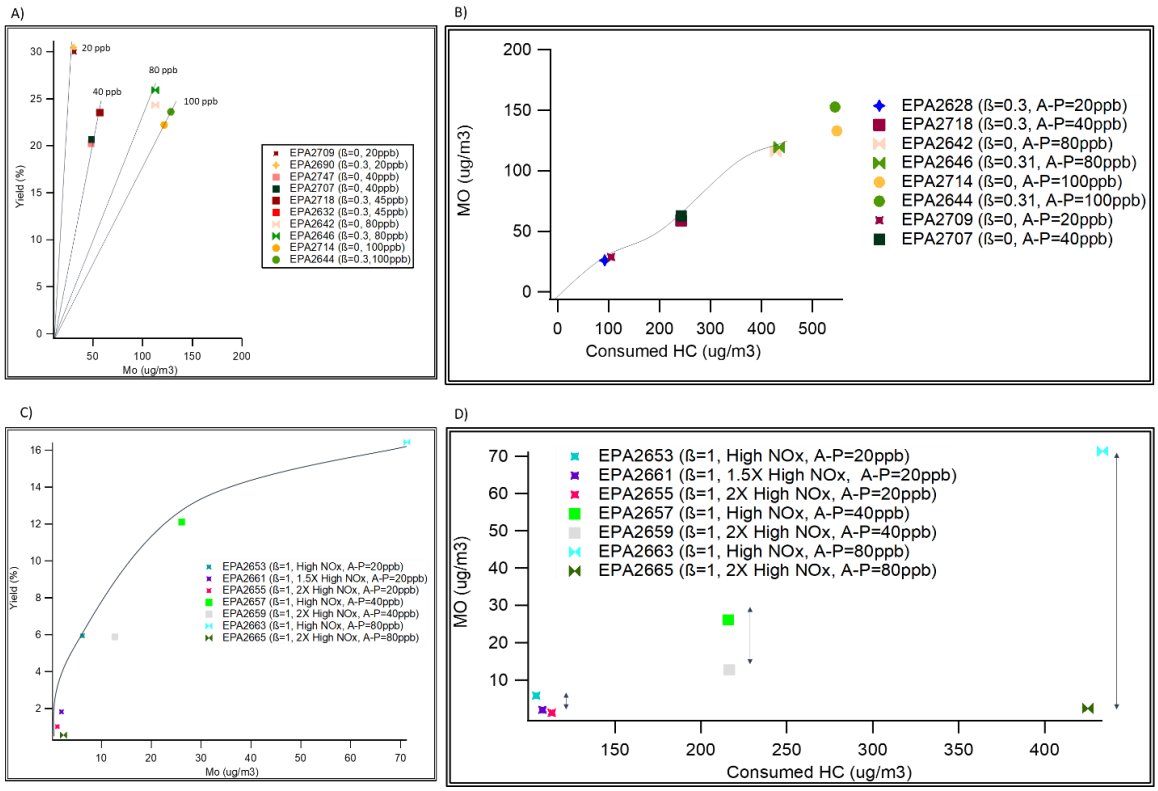

Figure 4.4. A) SOA yield versus SOA mass formed under no and low NO conditions. B) SOA mass formed versus HC consumed (ΔHC) at β=0 and 0.3 conditions. C) SOA yield versus SOA mass formed under high and 2X high NO conditions. D) SOA mass formed versus HC consumed (ΔHC) under high and 2X high NO conditions (β=1).

The elemental composition of SOA formed from α-pinene photooxidation was evaluated using an Aerodyne high-resolution time-of-flight mass spectrometer (HR-ToF-AMS) data. Previous studies have reported O/C between 0.3-0.43 for α-pinene ozonolysis, which correlates with compounds such as pinonic acid, and pinic acid with 3 to 4 oxygens (Chhabra, Flagan, & Seinfeld, 2010; Kim, Liu, Russell, & Paulson, 2014). As shown in **Figure S 4.5**Figure S 4.5. Van Krevelen diagram showing the atomic H:C vs. O:C ratios

SOA formed from α-pinene photooxidation exhibited O/C ranging from 0.40 to 0.65 along with H/C ranging from 1.48 to 1.80. This indicates that the products after more than 20 hours of photooxidation have 4 to 6 oxygens and 14 to 17 hydrogens (based on 10 carbon atoms in each molecule), which is consistent with second and third generation oxidized peroxy radicals (Piletic & Kleindienst, 2022). Therefore, under all b conditions, the oxidation state of SOA products was higher compared to the a-pinene ozonolysis products. Further, little dependence in the degree of oxidation was observed in O/C and H/C of SOA between the b=0 and b=1 experiments. Likewise, the α-pinene + ·OH photooxidation products that reported by Eddingsaas *et al.* exhibited similar O/C ratio ranges: diaterpenylic acids ($C_{10}H_{16}O_6$: O/C=0.6), 2-hydroxyterpenylic acid ($C_8H_{12}O_5$: O/C=0.625), terpenylic acids ($C_8H_{12}O_4$: O/C=0.5) 10-hydroxy pinonic acid ($C_{10}H_{16}O_4$: O/C=0.4), and 10-hydroxy terpenylic acids ($C_8H_{12}O_5$: O/C=0.625) (Eddingsaas, Loza, Yee, Chan, et al., 2012).

Each chamber experiments reported in this work were run for a minimum of 20 hours until both HC was consumed and a plateau in wall-loss corrected particle volume was achieved **(Figure 4.5)**. It was observed that the particle nucleation and aerosol formation rate were faster for β=0.3 compared to β=0 **(Figure 4.5 A)**. At high NO conditions, the nucleation did not occur until nearly ~150-200 min after irradiation and after most of the a-pinene was consumed **(Figure 4.5 B).**

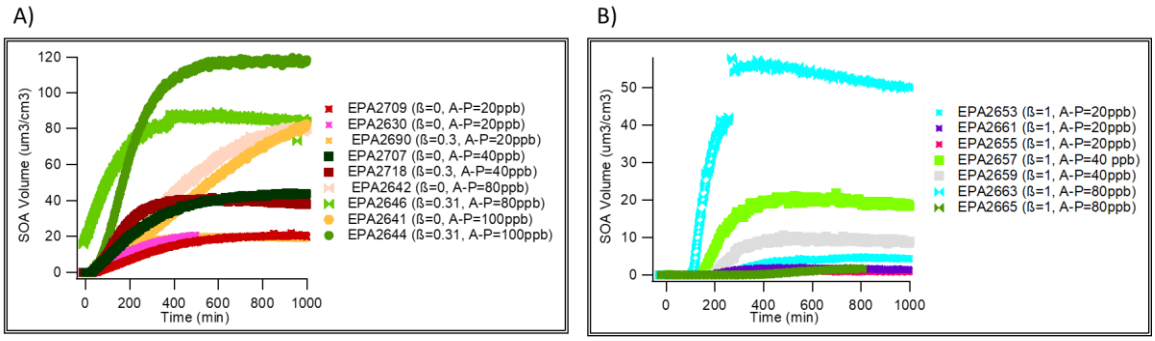

Figure 4.5. Wall-loss corrected volume of the particles formed over the course of experiment for A) low and no-NO conditions, B) at high NO conditions.

Classical experiments with instantaneous NO injection:

An additional classical experiment was performed for each continuous NO injection experiment, where NO was injected once prior to turning the lights on. The amount of NO injection in the classical experiments was calculated based on the total amount of NO injected (ppm/second) in chamber for continuous experiments at the point where $RO_2^{\cdot}$ was consumed, which varied experiment by experiment (from 400 min to 600 min) (**Table 4.1**). Since the β value in classical experiments, changes throughout the experiment, $RO_2^{\cdot}$ species experienced different NO regimes throughput the experiment. **Figure 4.6 A** shows the SOA yields versus SOA mass formed under 20, 40, and 80 ppb initial HC concentrations. SOA yield correlated with SOA mass for lower HC concentrations. Moreover, the SOA formation potentials were suppressed at high NO conditions due to the formation of higher volatile oxidation products. Except for 20 ppb α-pinene experiments, the SOA yields of low-NO experiments were higher than the corresponding no NO experiments, due to lower VOC/NO_x in low-NO 20 ppb α-pinene experiments compared to the corresponding 40 and 80 ppb α-pinene experiments. It was

observed that the NO was relatively high at the beginning of the low-NO classical experiments (initial 26 and 40 ppb NO for 20 and 40 ppb α-pinene, respectively) and dramatically dropped to ~2 ppb 50 minutes after lights on. However, in high-NO classical experiments the NO level decayed slower and was dependent on HC concentration. For example, the 20 ppb α-pinene experiment (Y=1.9%) took 400 minutes for NO to drop from the initial value of 40 ppb to ~10 ppb, while in 40 ppb experiment (Y=15.2%) it took only 100 minutes for the NO level to drop form the initial 63 ppb to ~10 ppb. This led to the SOA yield in the 20 ppb α-pinene experiment to be dramatically lower compared to the 40 α-pinene experiment. **Figure 4.6 B, C** shows the SOA yields from continuous NO injection method versus instantaneous injection method. It was observed that the SOA yield was smaller at low hydrocarbon (HC) concentration (20 ppb: **Figure 4.6 B**) and larger for the higher HC concentrations (40, 80 ppb α-pinene: **Figure 4.6 C**) in classical experiments.

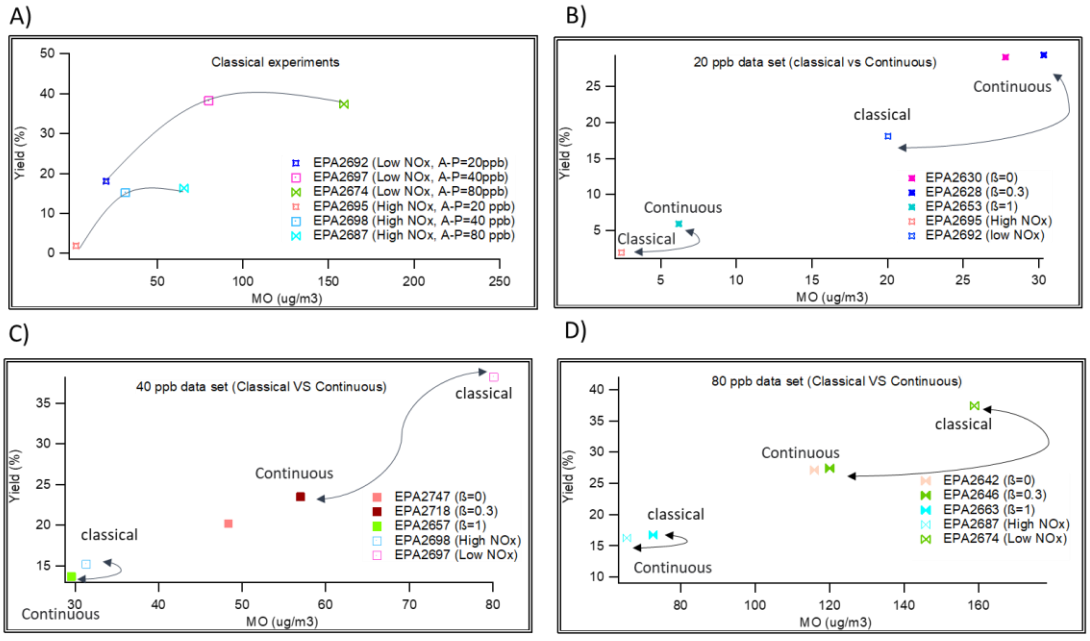

Figure 4.6. SOA yield versus SOA mass formed of continuous NO injections versus instantaneous NO injections.

Global impacts of continuous NO study on terpene SOA yields by Goddard Earth Observing System (GEOS-Chem):

Global branching ratios were also simulated from a global 3-D model of atmospheric chemistry driven by meteorological input from the Goddard Earth Observing System (GEOS-Chem) based on NO and $HO_2^{\cdot}$ concentration using VBS parameters obtained from a-pinene photooxidation under both β=1 (continuous high NO injection) and β=0 (no NO conditions). It was observed that the global impacts of modified terpene SOA yields are shown in **Figure 4.7**, including base terpene SOA concentrations (top), changes in terpene mass concentration using modified yields (middle), and percent difference that these changes represent (bottom). As shown here, increases of up to 1.1 ug m^{-3} are found in areas of high precursor emissions and base terpene SOA formation when using continuous NO injection experimental data under constant β conditions, representing concentration changes of up to 24% in those locations across modeled months. However, in areas characterized by low base terpene SOA formation, small reductions are more common as a result of these modifications. These reductions are relatively large on a percent change basis, but small in terms of total mass concentration. Surface grid cells with less than 1 ug m^{-3} of base terpene SOA show reductions averaging 37% due to mean drops of only 0.001 ug m^{-3}.

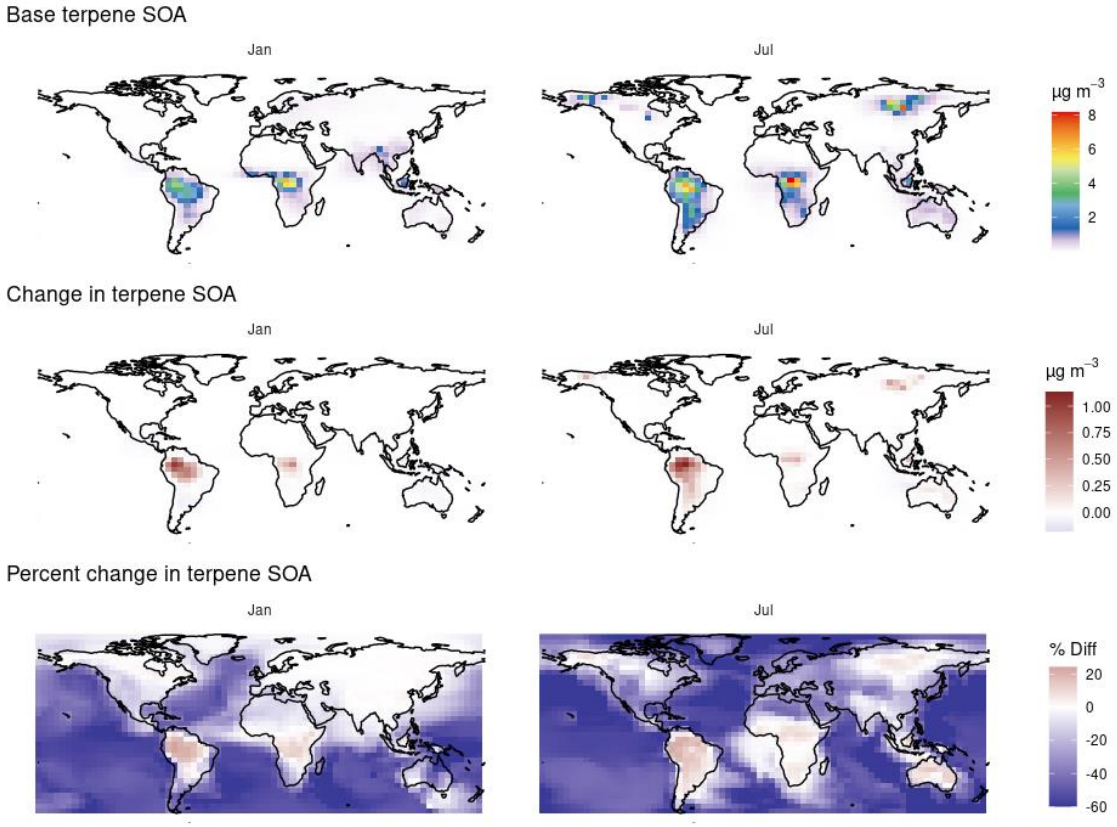

Figure 4.7. Global terpene SOA were simulated from a global 3-D model of atmospheric chemistry driven by meteorological input from the Goddard Earth Observing System (GEOS-Chem) based on NO and HO_2 concentration using VBS parameters obtained from the continuous NO injection chamber results under both β=1 and β=0 conditions. Base terpene SOA concentrations (top), changes in terpene mass concentration using modified yields (middle), and percent difference that these changes represent (bottom) (plot is provided by Dr. William Porter).

Conclusion:

The effect of continuous NO injection on SOA yields from α-pinene photooxidation was evaluated in a new 118 m^3 fixed-volume environmental chamber under fixed branching ratio values (β=0, 0.3, and 1.0) throughout the experiment. The NO injection flow rate for each experiment was calculated via SPRAC-11 simulations to obtain constant β experimental values. The corresponding classical experiments (similar VOC and NO_x (at

$RO_2^{\cdot}$ Depletion)) were then performed to compare the SOA yields and gas-phase chemistry with the NO experiments.

SOA yields for β=0.3 experiments (Y= 21.47%-30.45%) were observed to be roughly similar with SOA yields of β=0 conditions (Y= 20.22%-29.98%). It was observed that the SOA yield was substantially suppressed for β=1 conditions (0.56%-5.75%) where NO level was dramatically high (2X high NO conditions). For experiments that the NO concentration was under 10 ppb (β=0, 0.3), a direct correlation was observed between the SOA yields and both $RO_2^{\cdot}$ life-time (leading to further autooxidation) and $HO_2^{\cdot}/RO_2^{\cdot}$. The simulated $HO_2^{\cdot}/RO_2^{\cdot}$ was higher in β=0.3 experiments (Y= 21.47%-30.45%), while $RO_2^{\cdot}$ lifetime was higher in β=0 conditions (Y= 20.22%-29.98%). Moreover, slightly higher yields at 20 ppb were rationalized by the additional SOA formation for higher $HO_2^{\cdot}/RO_2^{\cdot}$ ratio compared to all 40, 80, 100 ppb of α-pinene experiments.

A high $RO_2^{\cdot}$ life-time increases the extend of autoxidation reaction, which was previously reported to be high for NO concentrations of below 10 ppb (Piletic & Kleindienst, 2022). The NO concentrations in the continuous experiments (b=0, 0.3, 1) did not exceed 10 ppb in the first 600 minutes (when $RO_2^{\cdot}$ have depleted). It is important to note that, in β=0.3 experiments, NO concentrations were low despite the continuous NO injected for the continuous NO injection and the experiments were ~95% converted from NO to NO_2. Moreover, the NO_x data illustrated that NOx consumption was dramatically higher in □=1 conditions compared to □=0.3. The oxidation state of SOA products were evaluated using HR-ToF-AMS and exhibited O/C ranging from 0.40 to 0.65 along with H/C ranging from 1.48 to 1.80. This indicates that the products after more than 20 hours of

photooxidation have 4 to 6 oxygens and 14 to 17 hydrogens (based on 10 carbon atoms in each molecule). Despite large differences in SOA yields, the oxidation state of SOA products in all β experiments were roughly the same.

In classical experiments, since the β value changes throughout the experiment, $RO_2^{\cdot}$ species experienced different NO regimes throughput the experiment. Thus, the SOA production pathways and yields were different from continuous NO injection experiments. The continuous NO injection method (constant β) revealed lower SOA yield than variable β (traditional VOC-NO) experiments at lower initial hydrocarbon (HC) concentration and higher SOA yield at higher HC conditions.

References:

Afreh, I. K., Aumont, B., Camredon, M., & Barsanti, K. C. (2021). Using GECKO-A to derive mechanistic understanding of secondary organic aerosol formation from the ubiquitous but understudied camphene. *Atmospheric Chemistry and Physics, 21*(14), 11467-11487. doi:10.5194/acp-21-11467-2021

Aruffo, E., Wang, J., Ye, J., Ohno, P., Qin, Y., Stewart, M., . . . Martin, S. T. (2022). Partitioning of Organonitrates in the Production of Secondary Organic Aerosols from alpha-Pinene Photo-Oxidation. *Environmental Science & Technology, 56*(9), 5421-5429. doi:10.1021/acs.est.1c08380

Bianchi, F., Kurten, T., Riva, M., Mohr, C., Rissanen, M. P., Roldin, P., . . . Ehn, M. (2019). Highly Oxygenated Organic Molecules (HOM) from Gas-Phase Autoxidation Involving Peroxy Radicals: A Key Contributor to Atmospheric Aerosol. *Chemical Reviews, 119*(6), 3472-3509. doi:10.1021/acs.chemrev.8b00395

Capouet, M., Müller, J. F., Ceulemans, K., Compernolle, S., Vereecken, L., & Peeters, J. (2008). Modeling aerosol formation in alpha-pinene photo-oxidation experiments. *Journal of Geophysical Research, 113*(D2), D02308. doi:10.1029/2007jd008995

Carter, W. P. L., & Heo, G. (2013). Development of revised SAPRC aromatics mechanisms. *Atmospheric Environment, 77*, 404-414. doi:10.1016/j.atmosenv.2013.05.021

Chhabra, P. S., Flagan, R. C., & Seinfeld, J. H. (2010). Elemental analysis of chamber organic aerosol using an aerodyne high-resolution aerosol mass spectrometer. *Atmospheric Chemistry and Physics, 10*(9), 4111-4131. doi:10.5194/acp-10-4111-2010

Chu, B., Hao, J., Takekawa, H., Li, J., Wang, K., & Jiang, J. (2012). The remarkable effect of FeSO4 seed aerosols on secondary organic aerosol formation from photooxidation of α-pinene/NOx and toluene/NOx. *Atmospheric Environment, 55*, 26-34. doi:10.1016/j.atmosenv.2012.03.006

Donahue, N. M., Robinson, A. L., Stanier, C. O., & Pandis, S. N. (2006). Coupled partitioning, dilution, and chemical aging of semivolatile organics. *Environmental Science & Technology, 40*(8), 2635-2643. doi:10.1021/es052297c

Eddingsaas, N. C., Loza, C. L., Yee, L. D., Chan, M., Schilling, K. A., Chhabra, P. S., . . . Wennberg, P. O. (2012). α-pinene photooxidation under controlled chemical conditions – Part 2: SOA yield and composition in low- and high-NOx environments. *Atmospheric Chemistry and Physics, 12*(16), 7413-7427. doi:10.5194/acp-12-7413-2012

Eddingsaas, N. C., Loza, C. L., Yee, L. D., Seinfeld, J. H., & Wennberg, P. O. (2012). α-pinene photooxidation under controlled chemical conditions – Part 1: Gas-phase composition in low- and high-NOx environments. *Atmospheric Chemistry and Physics, 12*(14), 6489-6504. doi:10.5194/acp-12-6489-2012

Farina, S. C., Adams, P. J., & Pandis, S. N. (2010). Modeling global secondary organic aerosol formation and processing with the volatility basis set: Implications for anthropogenic secondary organic aerosol. *Journal of Geophysical Research, 115*(D9). doi:10.1029/2009jd013046

Gill, K. J., & Hites, R. A. (2002). Rate Constants for the Gas-Phase Reactions of the Hydroxyl Radical with Isoprene, α- and β-Pinene, and Limonene as a Function of Temperature. *The Journal of Physical Chemistry A, 106*(11), 2538-2544. doi:10.1021/jp013532q

Guenther, A., Hewitt, C. N., Erickson, D., Fall, R., Geron, C., Graedel, T., . . . Zimmerman, P. (1995). A global model of natural volatile organic compound emissions. *Journal of Geophysical Research, 100*(D5), 8873. doi:10.1029/94jd02950

Jimenez, J. L., Canagaratna, M. R., Donahue, N. M., Prevot, A. S., Zhang, Q., Kroll, J. H., . . . Worsnop, D. R. (2009). Evolution of organic aerosols in the atmosphere. *Science, 326*(5959), 1525-1529. doi:10.1126/science.1180353

Khamaganov, V. G., & Hites, R. A. (2001). Rate Constants for the Gas-Phase Reactions of Ozone with Isoprene, α- and β-Pinene, and Limonene as a Function of Temperature. *The Journal of Physical Chemistry A, 105*(5), 815-822. doi:10.1021/jp002730z

Kim, H., Liu, S., Russell, L. M., & Paulson, S. E. (2014). Dependence of Real Refractive Indices on O:C, H:C and Mass Fragments of Secondary Organic Aerosol Generated from Ozonolysis and Photooxidation of Limonene and α-Pinene. *Aerosol Science and Technology, 48*(5), 498-507. doi:10.1080/02786826.2014.893278

Kurten, T., Tiusanen, K., Roldin, P., Rissanen, M., Luy, J. N., Boy, M., . . . Donahue, N. (2016). alpha-Pinene Autoxidation Products May Not Have Extremely Low Saturation Vapor Pressures Despite High O:C Ratios. *The Journal of Physical Chemistry A, 120*(16), 2569-2582. doi:10.1021/acs.jpca.6b02196

Lee, B. H., Iyer, S., Kurtén, T., Varelas, J. G., Luo, J., Thomson, R. J., & Thornton, J. A. (2023). Ring-opening yields and auto-oxidation rates of the resulting peroxy radicals from OH-oxidation of α-pinene and β-pinene. *Environmental Science: Atmospheres, 3*(2), 399-407. doi:10.1039/d2ea00133k

Li, L., Tang, P., & Cocker, D. R. (2015). Instantaneous nitric oxide effect on secondary organic aerosol formation from m-xylene photooxidation. *Atmospheric Environment, 119*, 144-155. doi:10.1016/j.atmosenv.2015.08.010

Malloy, Q. G. J., Nakao, S., Qi, L., Austin, R., Stothers, C., Hagino, H., & Cocker, D. R. (2009). Real-Time Aerosol Density Determination Utilizing a Modified Scanning Mobility Particle Sizer—Aerosol Particle Mass Analyzer System. *Aerosol Science and Technology, 43*(7), 673-678. doi:10.1080/02786820902832960

Marais, E. A., Jacob, D. J., Jimenez, J. L., Campuzano-Jost, P., Day, D. A., Hu, W., . . . McNeill, V. F. (2016). Aqueous-phase mechanism for secondary organic aerosol formation from isoprene: application to the Southeast United States and co-benefit of SO(2) emission controls. *Atmos Chem Phys, 16*(3), 1603-1618. doi:10.5194/acp-16-1603-2016

Moller, K. H., Otkjaer, R. V., Chen, J., & Kjaergaard, H. G. (2020). Double Bonds Are Key to Fast Unimolecular Reactivity in First-Generation Monoterpene Hydroxy Peroxy Radicals. *The Journal of Physical Chemistry A, 124*(14), 2885-2896. doi:10.1021/acs.jpca.0c01079

Ng, N. L., Chhabra, P. S., Chan, A. W. H., Surratt, J. D., Kroll, J. H., Kwan, A. J., . . . Seinfeld, J. H. (2007). Effect of NOx level on secondary organic aerosol (SOA) formation from the photooxidation of terpenes. *Atmospheric Chemistry and Physics, 7*(19), 5159-5174. doi:DOI 10.5194/acp-7-5159-2007

Ng, N. L., Kroll, J. H., Chan, A. W. H., Chhabra, P. S., Flagan, R. C., & Seinfeld, J. H. (2007). Secondary organic aerosol formation from m-xylene, toluene, and benzene. *Atmospheric Chemistry and Physics, 7*(14), 3909-3922. doi:DOI 10.5194/acp-7-3909-2007

Pai, S. J., Heald, C. L., Pierce, J. R., Farina, S. C., Marais, E. A., Jimenez, J. L., . . . Vu, K. (2020). An evaluation of global organic aerosol schemes using airborne observations. *Atmospheric Chemistry and Physics, 20*(5), 2637-2665. doi:10.5194/acp-20-2637-2020

Piletic, I. R., & Kleindienst, T. E. (2022). Rates and Yields of Unimolecular Reactions Producing Highly Oxidized Peroxy Radicals in the OH-Induced Autoxidation of alpha-Pinene, beta-Pinene, and Limonene. *The Journal of Physical Chemistry A, 126*(1), 88-100. doi:10.1021/acs.jpca.1c07961

Porter, W. C., Jimenez, J. L., & Barsanti, K. C. (2021). Quantifying Atmospheric Parameter Ranges for Ambient Secondary Organic Aerosol Formation. *ACS Earth and Space Chemistry, 5*(9), 2380-2397. doi:10.1021/acsearthspacechem.1c00090

Pye, H. O. T., Chan, A. W. H., Barkley, M. P., & Seinfeld, J. H. (2010). Global modeling of organic aerosol: the importance of reactive nitrogen (NOx and NO3). *Atmospheric Chemistry and Physics, 10*(22), 11261-11276. doi:10.5194/acp-10-11261-2010

Sindelarova, K., Markova, J., Simpson, D., Huszar, P., Karlicky, J., Darras, S., & Granier, C. (2022). High-resolution biogenic global emission inventory for the time period 2000–2019 for air quality modelling. *Earth System Science Data, 14*(1), 251-270. doi:10.5194/essd-14-251-2022

Tanner, D. J., & Eisele, F. L. (1995). Present OH measurement limits and associated uncertainties. *Journal of Geophysical Research, 100*(D2), 2883. doi:10.1029/94jd02609

Wu, K., Yang, X., Chen, D., Gu, S., Lu, Y., Jiang, Q., . . . Lu, S. (2020). Estimation of biogenic VOC emissions and their corresponding impact on ozone and secondary organic aerosol formation in China. *Atmospheric Research, 231*, 104656. doi:10.1016/j.atmosres.2019.104656

Xu, L., Moller, K. H., Crounse, J. D., Otkjaer, R. V., Kjaergaard, H. G., & Wennberg, P. O. (2019). Unimolecular Reactions of Peroxy Radicals Formed in the Oxidation of alpha-Pinene and beta-Pinene by Hydroxyl Radicals. *The Journal of Physical Chemistry A, 123*(8), 1661-1674. doi:10.1021/acs.jpca.8b11726

Zhang, H., Yee, L. D., Lee, B. H., Curtis, M. P., Worton, D. R., Isaacman-VanWertz, G., . . . Goldstein, A. H. (2018). Monoterpenes are the largest source of summertime organic aerosol in the southeastern United States. *Proceedings of the National Academy of Sciences 115*(9), 2038-2043. doi:10.1073/pnas.1717513115

Zhang, S.-H., Shaw, M., Seinfeld, J. H., & Flagan, R. C. (1992). Photochemical aerosol formation from α-pinene- and β-pinene. *Journal of Geophysical Research, 97*(D18), 20717. doi:10.1029/92jd02156

Zhao, D. F., Schmitt, S. H., Wang, M. J., Acir, I. H., Tillmann, R., Tan, Z. F., . . . Mentel, T. F. (2018). Effects of NOx and SO2 on the secondary organic aerosol formation from photooxidation of alpha-pinene and limonene. *Atmospheric Chemistry and Physics, 18*(3), 1611-1628. doi:10.5194/acp-18-1611-2018

Supplementary material of chapter 4

Influence of Continuous NO Injection on SOA Yield from Biogenic Precursors: A Comprehensive Branching Ratio Study

Sahar Ghadimi[1], Huawei Li[1], William Porter[2], David R. Cocker[1]

[1]University of California, Bourns College of Engineering, Center for Environmental Research and Technology (CE-CERT), 1084 Columbia Avenue, Riverside, CA, USA

[2]Department of Chemical and Environmental Engineering, Bourns College of Engineering, University of California, Riverside, CA, USA

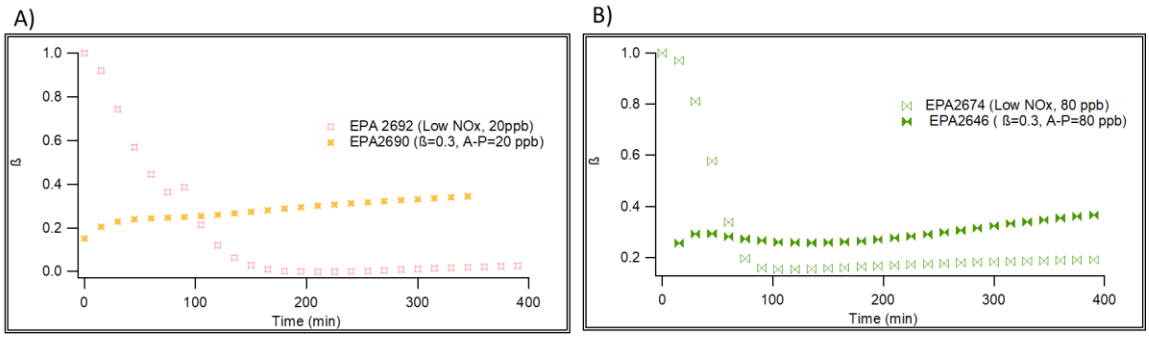

Figure S 4.1. Calculated β ratio using SAPRAC-11: A) The β values of classical experiment vs β=0.3 for 20 ppb. B) The β values of classical experiment vs β=0.3 for 80 ppb.

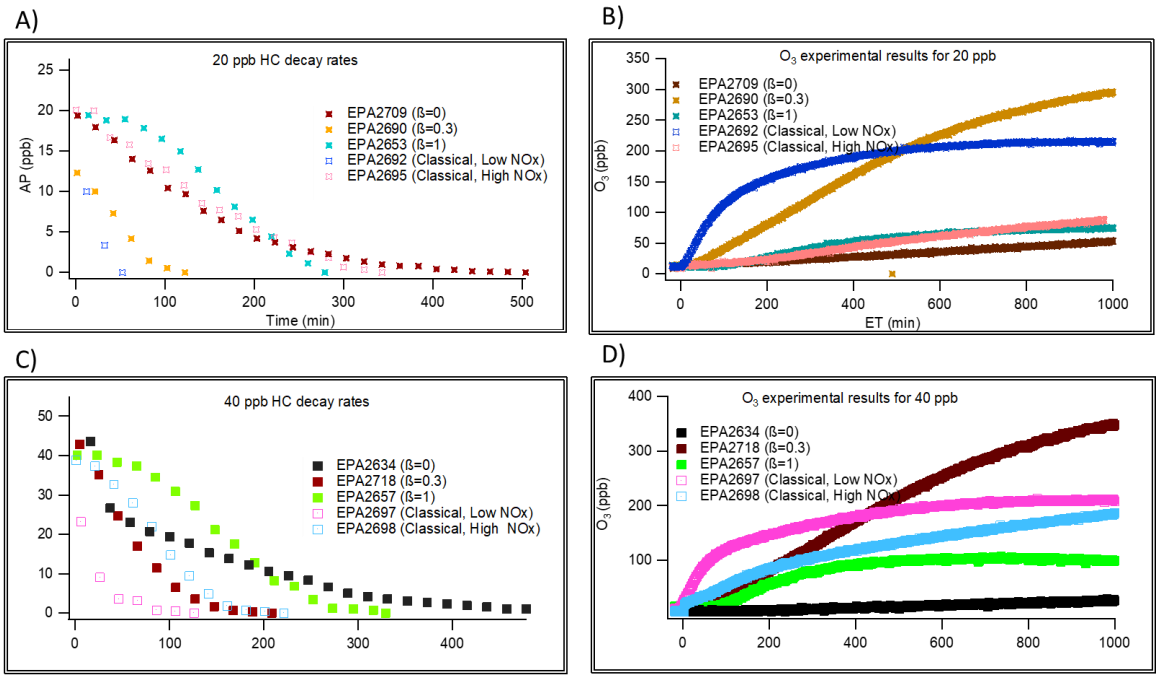

Figure S 4.2. The HC decay rates and O_3 formations inside the chamber at different β values. A) The HC decay rate for 20 ppb of α-pinene experiments. B) the O_3 formations at different β conditions for 20 ppb of α-pinene experiments. C) The HC decay rate for 40 ppb of α-pinene experiments. D) the O_3 formations at different β conditions for 40 ppb of α-pinene experiments.

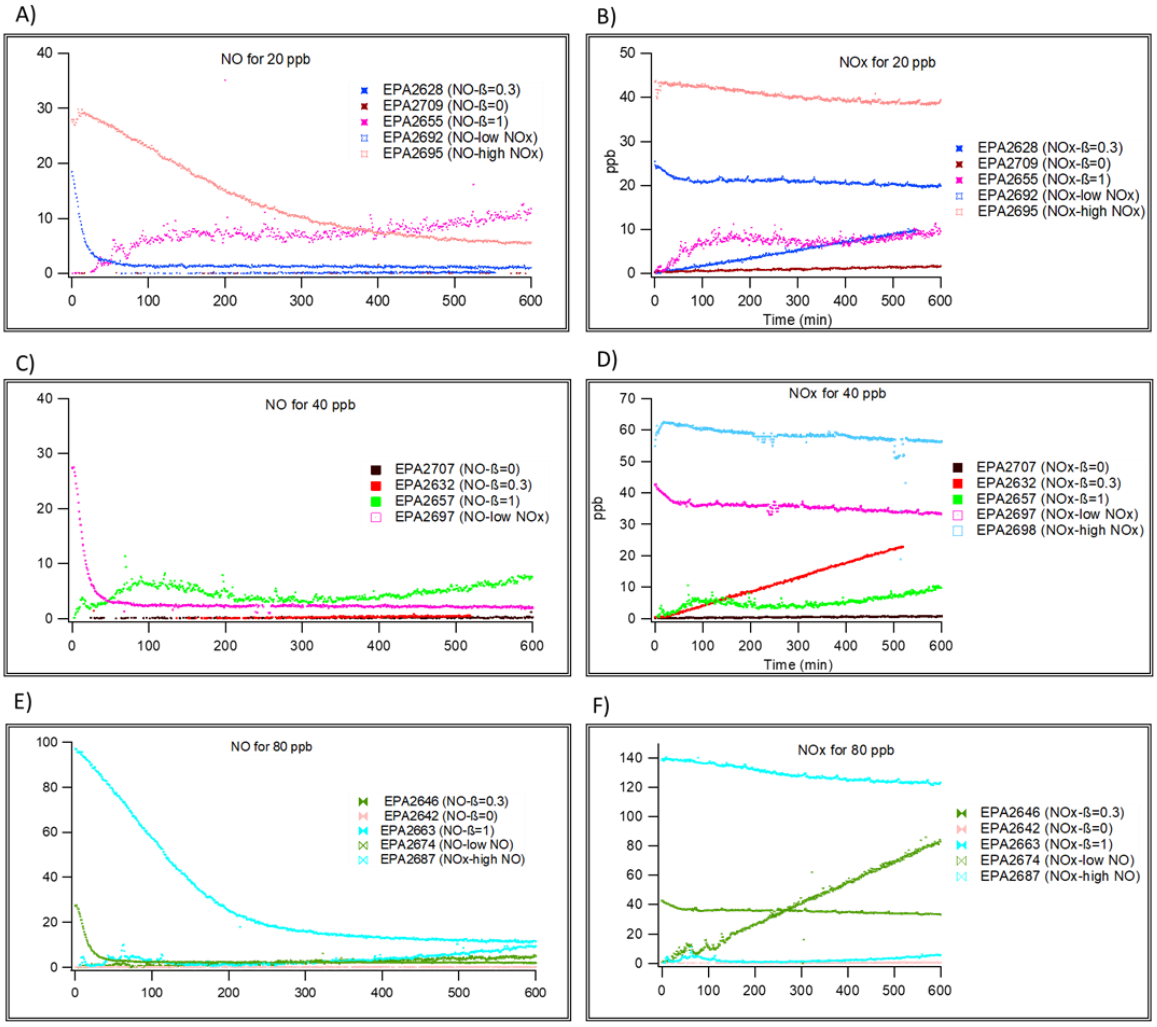

Figure S 4.3. The measured NO and NO_x inside the chamber at different β values, over the course of experiment for 20 ppb, 40 ppb, 80 ppb.

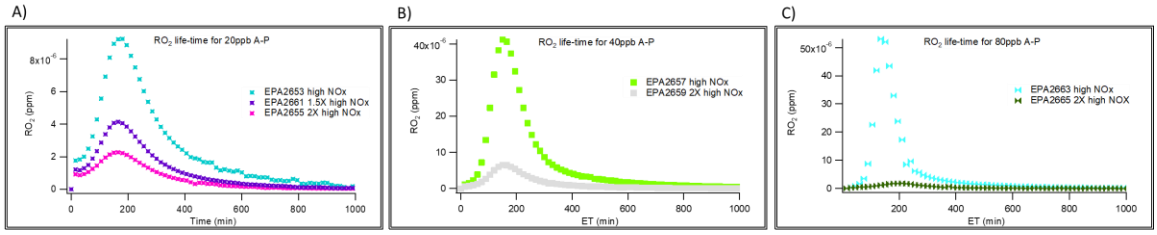

Figure S 4.4. $RO_2^{\cdot}$ lifetime simulated under high and 2X high NO_x conditions at A) 20 ppb, B) 40 ppb, C) 80 ppb.

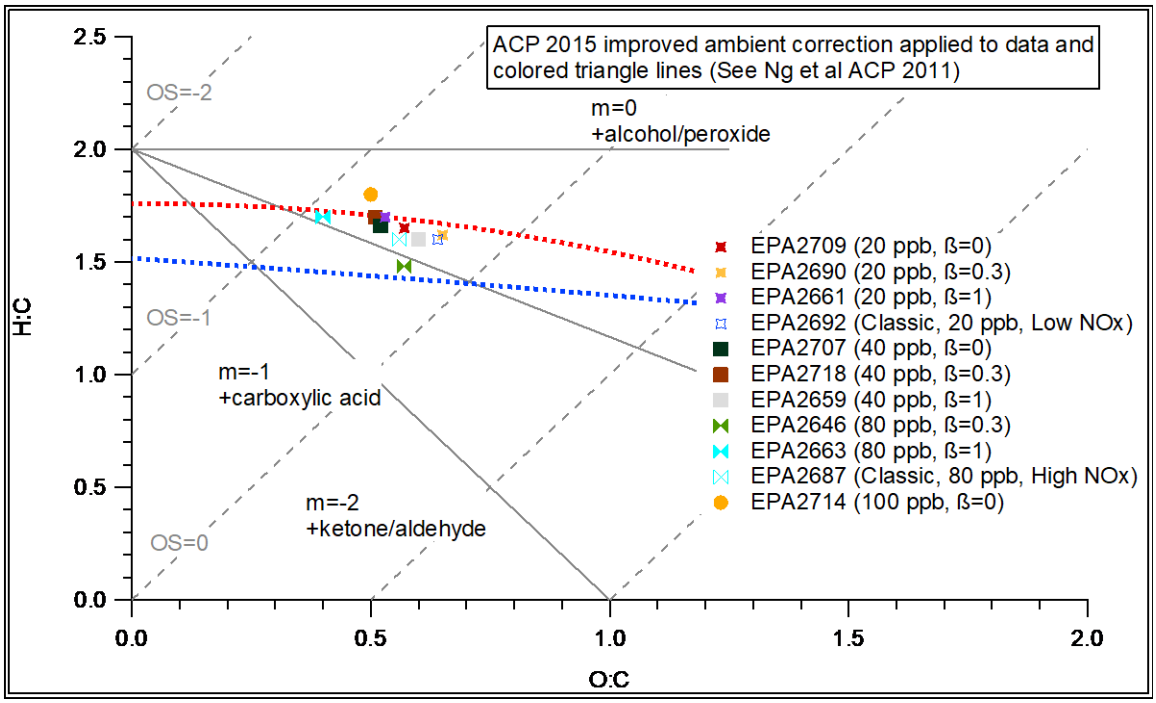

Figure S 4.5. Van Krevelen diagram showing the atomic H:C vs. O:C ratios.

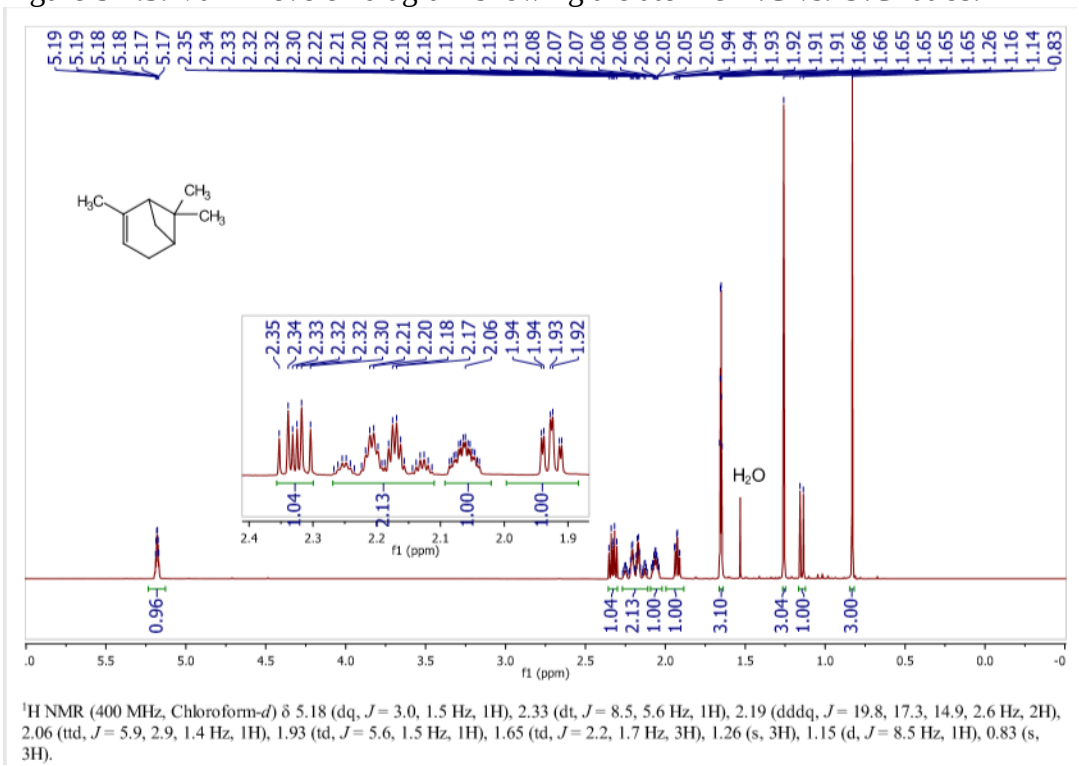

Figure S 4.6. Iinvestigating α-Pinene (<99%) purity by: ^{1}H NMR

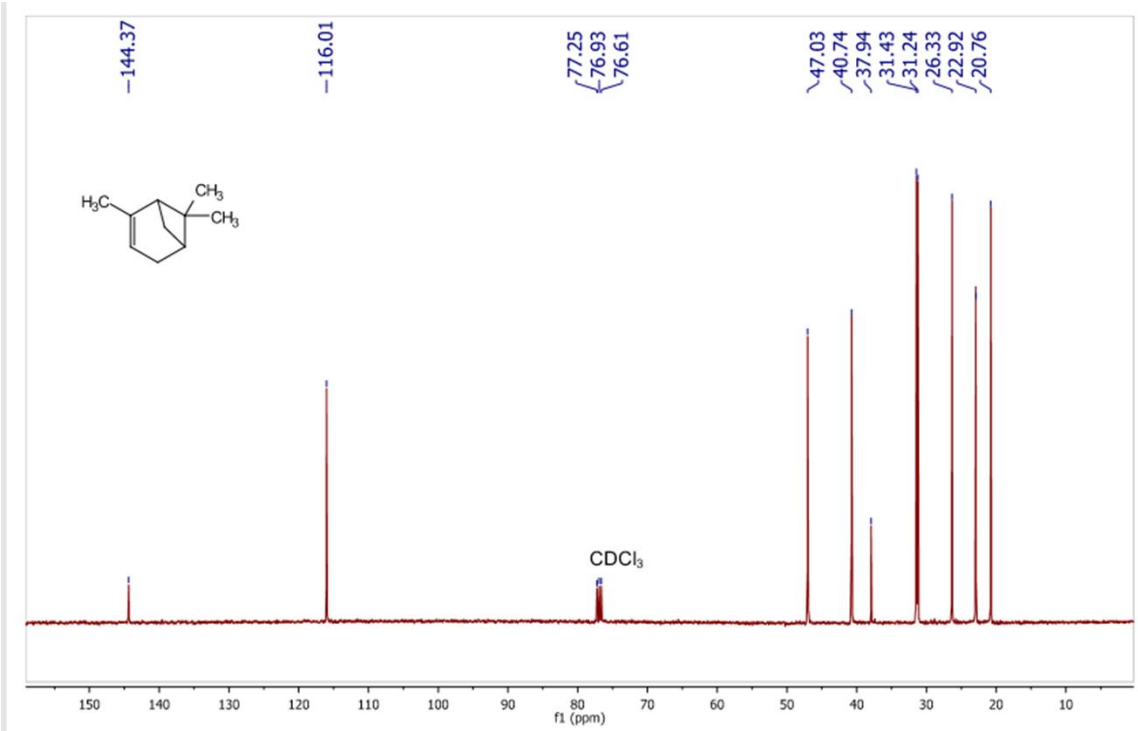

^{13}C NMR (101 MHz, Chloroform-*d*) δ 144.37, 116.01, 47.03, 40.74, 37.94, 31.43, 31.24, 26.33, 22.92, 20.76.

Figure S 4.7. Investigating α-Pinene (<99%) purity by: ^{13}C NMR

Chapter 5 : Conclusion & Recommendations for Future Work

The overall goal of this thesis is to have a better understanding of anthropogenic pollutants in the aspect of primary and secondary emissions from HDVs running under different fuels, aftertreatments, driving cycles, to acquire a comprehensive analysis on the air quality, health impacts, climate change impacts of these different variables. Since recently there has been a lot of passed mandates to move toward electric vehicle adoption in the light-duty sector, thus the major emissions from on-road transportation sector, will be due to heavy-duty vehicles of different vocations. The heavy-duty vehicle electrification is more difficult to achieve on a large scale. Consequently, advancements in engine technology and aftertreatment controls, and the widespread use of low- or zero-carbon fuels will be necessary.

In chapter two, the primary emissions and secondary aerosol production were characterized by two in-use HDDVs operated with typical ULSD and HVO fuels over the UDDS and HHDDT Cruise cycles on a chassis dynamometer. It was observed that the HVO fuels had lower THC, NO_x, and PM emissions compared to ULSD. The primary emissions were mostly comprised of organic mass compared to inorganic mass. After 5 hours of photooxidation the secondary mass significantly exceeded the primary mass for all the experiments. The ULSD fueled DPF/SCR HDDV produced a substantial amount of secondary inorganic material (~20% ammonium and 61% nitrate), whereas the secondary aerosol mass for the DPF/SCR HDDV operated on HVO was almost exclusively comprised of organics (~99%). The no-SCR HDDV (up to 712 mg/mile) secondary aerosol mass was

substantially higher compared to the DPF/SCR HDDV (lower than 12 mg/mile) due to non-functioning DPF, which affected both the primary PM emissions and secondary aerosol formation. Consequently, for reducing both primary and secondary emissions from HDDVs it is critical to have fully functioning DOC/DPF aftertreatment systems. Moreover, The results from this study exhibited that the use of HVO will provide additional benefits on primary emissions and secondary aerosol formation from in-use HDDVs.

Detailed chemical composition was performed using the HR-ToF-AMS for all experiments. The hydrocarbon species (C_xH_y) which were dominant in POA, originated from unburnt fuel. Interestingly, the HVO exhaust emissions organic aerosols contained higher CHO class compounds versus CH class when compared to ULSD under similar conditions, this is due to the higher cetane number of HVO fuel and its better burning properties. It is important to note that in ULSD POA emissions the aromatic species (*m/z* 77, 110, etc.) were higher compared to HVO fuel. The aromatics content in ULSD fuel was 9.9%, whereas in HVO 1.2%. After 5 hours of photochemical oxidation, the *m/z* 44 peak substantially increased, which is evidence of significant oxidation and photochemistry. The $C_4H_9^+$ fragment for the *m/z* 57 peak was used as a tracer to calculate evolution of secondary organic aerosol formation during the photochemical oxidation. The percentage of ΔOA(5h) was calculated using $C_4H_9^+$ as a tracer and showed a range of 71% to 81% after 5 hours of irradiation, emphasizing the importance of diesel exhaust as a source of urban SOA, with size distributions dominated by the accumulation mode.

In chapter three, the primary emissions and secondary aerosol formations from two in-use diesel and 6 natural gas heavy-duty vehicles of different vocations were analyzed.

Tailpipe emissions testing was performed on a chassis dynamometer under different driving cycles. Secondary aerosol was measured after introducing dilute exhaust into a 30 m^3 environmental chamber. Comparing the primary emissions from HDDVs equipped with advanced after treatments (DPF+DOC+SCR) with natural gas vehicles equipped with three-way catalysts (TWCs), both particulate matter (PM) and non-methane organic gas (NMOG) emissions were found to be higher for CNG vehicles. Moreover, the substantial formation of ammonium nitrate in CNG vehicles with TWC was due to ammonia tailpipe emissions. The advanced aftertreatment controls in diesel vehicles resulted in almost negligible secondary organic aerosol (SOA) formation, while the natural gas vehicles led to elevated SOA formation that was likely enhanced by the inherent inorganic seed aerosol and lubricant oil leakage issues. For some natural gas vehicles, the contribution of lubricating oil in primary organic aerosol was dominant (as shown in the mass spectra analysis) leading to enhanced SOA mass.

Our work illustrates that diesel vehicles with well-functioning robust aftertreatment controls will not only provide significant tailpipe emission benefits but will also be an almost negligible source of SOA formation from the transportation sector. This work showed a nonfuel source of SOA formation from some natural gas vehicles (lubricant oil), thus there was not a clear relationship for the natural gas vehicles between engine technology (as indicated by the engine certification for engines certified to 0.2 g/bhp-hr NO_x emissions vs. 0.02 g/bhp-hr ultra-low NO_x emissions). As a result, it is critical to control lubricant oil consumption and new lubricant oil formulations in natural gas engines which will result in lower POA emissions and reduced SOA formation. Applying a

catalyzed gasoline particulate filter in natural gas engines for the reduction of particles related to lubricant oil and SOA precursor emissions is critical. Finally, more efficient control of ammonia emissions (ammonia slip) from SCR-equipped and TWC-equipped vehicles via advanced oxidation catalysts will also result in the reduction of secondary ammonium nitrate aerosol that will in turn lead to lower SOA yields.

This thesis provides valuable data and analysis on the effects of different aftertreatment, and the chemical composition of different fuels. However, the chemical composition of different fuels and the lubricant oil can also be evaluated using a soft ionization technique (CIMS) to have a better understanding of the products that have been formed after 5 hours of photooxidation. Also, it has been observed that ammonium nitrate has a direct correlation with SOA formation potentials, which the data from CIMS can be valuable information regarding the organic versus inorganic particles interactions.

In chapter 4, the effect of continuous NO injection on SOA yields and the fate of RO_2 from α-pinene photooxidation was evaluated in a new 118 m^3 fixed-volume environmental chamber under fixed branching ratio values (β=0, 0.3, and 1.0) throughout the experiment. The corresponding classical experiments (variable β values) were also performed to compare the SOA yields and gas-phase chemistry with continuous NO experiments (fixed β value).

The SOA yields were higher at low NO conditions β=0 (Y= 20.22%-29.98%) and β=0.3 (Y= 21.47%-30.45%) compared to β=1 (0.56%-5.75%) where NO level was dramatically high (2X high NO conditions). It was observed that the yields under β=0.3 experiments were roughly similar with SOA yields of β=0 conditions. A direct

correlation was observed between the SOA yields and both $RO_2^{\cdot}$ life-time (leading to future autooxidation) and $HO_2^{\cdot}/RO_2^{\cdot}$ for both low and no NO conditions (β=0, 0.3). The simulated $HO_2^{\cdot}/RO_2^{\cdot}$ was higher in β=0.3 experiments (Y= 21.47%-30.45%), while $RO_2^{\cdot}$ lifetime was higher in β=0 conditions (Y= 20.22%-29.98%). Moreover, slightly higher yields in 20 ppb were rationalized by higher $HO_2^{\cdot}/RO_2^{\cdot}$ ratio compared to all 40, 80, 100 ppb of α-pinene experiments.

In all the continuous experiments (β=0, 0.3, 1) the NO concentrations did not exceed 10 ppb in the first 600 minutes (when $RO_2^{\cdot}$ have depleted). In β=0.3 experiments the NO concentrations were low throughout the experiment due to the presence of H_2O_2 which converted ~95% of NO to NO_2. However, in all β=1 conditions the NO_2 level was low due to no H_2O_2 injection. Moreover, the NO_x consumption was dramatically higher in β=1 conditions compared to β=0.3.

In classical experiments, since the β value changed throughout the experiment, $RO_2^{\cdot}$ specious experienced different NO regimes in the course of experiment. Thus, the SOA production pathways and yields were different from continuous NO injection experiments. The continuous NO injection method (constant β) revealed lower SOA yield than variable β (traditional VOC-NO) experiments at lower initial hydrocarbon (HC) concentration and higher SOA yield at higher HC conditions.

The surface β were simulated globally using GOES-Chem and was shown that β values were constant ranging from 0.25 to 0.75 around the world. In this work, Global branching ratios were also simulated from a global 3-D model of atmospheric chemistry driven by meteorological input from the Goddard Earth Observing System

(GEOS-Chem) based on NO and $HO_2^{\cdot}$ concentration using VBS parameters obtained from α-pinene photooxidation under both β=1 (continuous high NO injection) and β=0 (no NO conditions). The GOES-Chem results showed that increases of up to 1.1 ug m^{-3} are found in areas of high precursor emissions and base terpene SOA formation when using continuous NO injection experimental data under constant β conditions, representing concentration changes of up to 24% in those locations across modeled months. On the other hand, in regions where there is low base terpene SOA formation, small reductions are more common as a result of these modifications. These reductions are relatively large on a percent change basis, but small in terms of total mass concentration. Surface grid cells with less than 1 ug m^{-3} of base terpene SOA show reductions averaging 37% due to mean drops of only 0.001 ug m^{-3}.

The NO_x impacts on SOA formations from α-pinene was investigated in this thesis using a novel approach of controlling β. The same approach should be applied to other biogenic and aromatic hydrocarbons. For instance, sesquiterpenes have shown to have a different behavior under high and low NO conditions, with increasing the SOA yield as the NO concentration increases. Also, in this study only β=0, 0.3, and 1 was evaluated, implementing other β values in conjunction with CIMS can provide a better picture on the end products that are formed in each path way and a better understanding on autoxidation.